
Controlled Spatial Arrangement
of Gold Nanoparticles
using Focused Laser Beams
and DNA Origami

Jaekwon Do



München 2014

Controlled Spatial Arrangement
of Gold Nanoparticles
using Focused Laser Beams
and DNA Origami

Jaekwon Do

Dissertation

Submitted to the Physics Department
of the Ludwig-Maximilians-Universität München

by

Jaekwon Do

of

Seoul, Republic of Korea

München, March 17th, 2014

First reviewer:

Prof. Dr. Jochen Feldmann

Second reviewer:

Prof. Dr. Tim Liedl

Additional members of oral examination:

Prof. Dr. Ulrich Schollwöck

Prof. Dr. Joachim Rädler

Date of examination :

May 9, 2014

Publications

Hierarchical assembly of metal nanoparticles, quantum dots and organic dyes using DNA origami scaffolds

Robert Schreiber, Jaekwon Do, Eva-Maria Roller, Tao Zhang, Verena J. Schüller, Philipp C. Nickels, Jochen Feldmann, and Tim Liedl

Nature Nanotechnology, 9 (1), 74-78 (2014)

Two-Color Laser Printing of Individual Gold Nanorods

Jaekwon Do, Michael Fedoruk, Frank Jäckel, and Jochen Feldmann

Nano Letters, 13 (9), 4164–4168 (2013)

Photonic-Crystal Nanocavities Containing Plasmonic-Nanoparticles Assembled Using a Laser-Printing Technique

Jaekwon Do, Khalid N. Sediq, Kieran Deasy, David M. Coles, Jessica Rodríguez-Fernández, Jochen Feldmann, and David G. Lidzey

Advanced Optical Materials, 1 (12), 946-951 (2013)

Design and Optical Trapping of a Biocompatible Propeller-like Nanoscale Hybrid

Jaekwon Do, Robert Schreiber, Andrey A. Lutich, Tim Liedl, Jessica Rodríguez-Fernández, and Jochen Feldmann

Nano Letters, 12 (9), 5008-5013 (2012)

Conferences and workshops

Optical two-colour printing of single gold nanorods

The 2013 International Conference on Advances in Nano Research

Seoul, Republic of Korea, 2013

Synthesis and optical trapping of a biocompatible gold nanoparticle/DNA Origami hybrid

SPIE Photonics West

San Francisco, USA, 2013

Synthesis and optical trapping of DNA origami & AuNP hybrid nanoparticle

Workshop from Biophotonics to Optoelectronics

Riezlern, Austria, 2011

Optically driven tunable fluorescence emission intensity on hybrid (organic/inorganic) nanostructure

Seoul Nanohealth 2011 Symposium

Seoul, Republic of Korea, 2011

Table of Contents

Table of Contents.....	vii
Kurzfassung.....	ix
1. Introduction.....	1
2. Fundamentals.....	7
2.1 Optical properties of metal nanoparticles.....	8
2.2 Optical forces on metal nanoparticles in a focused laser beam.....	19
2.3 Laser-induced heating of metal nanoparticles.....	25
2.4 DNA nanotechnology.....	28
3. Characterization, design and modeling of nanostructures.....	39
3.1 Optical property characterization.....	40
3.2 Morphological and surface properties characterization.....	43
3.3 Numerical modeling.....	49
3.4 Tool for designing and preparing of DNA origami structures.....	51
4. Optical printing of single gold nanoparticles with a focused laser beam.....	55
4.1 Two-color laser printing of single gold nanorods with control over their spatial location and angular orientation.....	56
4.1.1 Motivation for a top-down optical printing technique for depositing non-spherical gold nanoparticles.....	56
4.1.2 Longitudinal and transverse plasmon modes of gold nanorods.....	57
4.1.3 Two-color laser printing setup and PEGylation of gold nanorods.....	61
4.1.4 Sequential two-color laser printing process: trapping, aligning and printing.....	65
4.1.5 Effect of relative orientation and laser power of two lasers on angular printing precision of gold nanorods.....	71
4.1.6 Summary.....	77
4.2 Laser printing of spherical gold nanoparticles onto a silicon nitride photonic crystal nanocavity.....	78

4.2.1 Motivation for a top-down laser printing technique for creating a photonic crystal nanocavity containing a gold nanoparticle	78
4.2.2 Optical printing setup and silicon nitride photonic crystal nanocavity	79
4.2.3 Single gold nanoparticle printing onto a silicon nitride photonic crystal nanocavity.....	82
4.2.4 Interaction between surface plasmons and fundamental nanocavity mode in hybrid nanocavity	85
4.2.5 Summary.....	89
5. Hierarchical assembly of planet-satellite type nanostructures by using DNA origami technique	91
5.1 DNA origami technique for spatial arrangement of gold nanoparticles	92
5.2 Design and preparation of planet-satellite type nanostructures	93
5.3 Tuning the morphological properties of planet-satellite type nanostructures .	110
5.4 Planet-satellite type nanostructures for studying fluorescence quenching, light-harvesting antenna, and signal enhancement of circular dichroism.....	116
5.5 Summary	120
6. Deposition of planet-satellite type nanostructures using focused laser beam	123
6.1 Hybrid top-down/bottom-up nanofabrication approach: toward highly complex architecture.....	124
6.2 Plasmonic heating of planet-satellite type nanostructures and their thermal stability	125
6.3 Soft-optical deposition of planet-satellite type nanostructures with focused laser beam	132
6.4 Effect of laser power on the morphology of planet-satellite type nanostructures	138
6.5 Summary	142
7. Conclusion and outlook	145
References.....	149
Acknowledgements.....	164

Kurzfassung

In dieser Dissertation werden drei Methoden beschrieben, um die räumliche Anordnung von plasmonischen Nanopartikeln mit der Hilfe von **stark fokussierten Lasern** und der **DNA Origami** Technik zu kontrollieren. Die Methoden können jeweils den *Top-Down*, den *Bottom-Up* bzw. den Hybridverfahren (*Top-Down/Bottom-Up*) zugeordnet werden.

Im *Top-Down-Verfahren* wurde ein stark fokussierter Laser verwendet, um sphärische und elongierte Goldpartikel auf eine Siliziumnitridmembran sowie auf Glassubstrate aufzubringen. Dazu wurde zunächst ein Laser mit resonanter und ein Laser mit nicht resonanter Wellenlänge benutzt, um Goldpartikel auf ein Glassubstrat zu drucken. Die Effekte verschiedener Kombinationen der relativen Polarisation und Leistung der beiden Laser wurden untersucht, um die Positionierung und Orientierung der gedruckten Goldnanostäbchen zu kontrollieren. Des Weiteren wurde ein monochromatischer Laser dazu genutzt, einzelne Goldnanopartikel exakt an Fehlstellen eines Nanoresonators in einem photonischen Kristall aus Siliziumnitrid aufzubringen. Diese Technik stellt eine deutliche Verbesserung des Herstellungsprozesses hinsichtlich Geschwindigkeit und Einfachheit im Vergleich zu bereits bestehenden Methoden dar. Auch wurden Dämpfung und Verbreiterung der Grundmode des Nanoresonators in dem photonischen Kristall beobachtet und mit Computersimulationen verglichen.

Im *Bottom-Up-Verfahren* wurden Goldnanostrukturen unter Verwendung der DNA Origami Technik zu „Planet-Satellit-Nanostrukturen“ durch Selbstorganisation hergestellt. In diesen Nanostrukturen diente ein „Goldnanopartikel-Planet“ als feste Basis für die weitere Assemblierung der „Goldnanopartikel-Satelliten“ durch vorgefertigte DNA Origami Strukturen definierter Größe und Form. Der schrittweise Aufbau dieser Methode ermöglichte die Kontrolle der Gesamtausdehnung der Struktur, des Abstandes zwischen den einzelnen Bauelementen und der Anzahl der „Planet“-gebundenen „Satelliten“. Ferner stellten diese Strukturen ein ideales Modell dar, um durch die Verwendung verschiedener Elemente wie metallische Nanopartikel, Quantenpunkte und fluoreszierende Farbstoffe Untersuchungen über die abstandsabhängige Fluoreszenzlöschung von Goldnanopartikel-gebundenen Farbstoffmolekülen, die Energiegewinnung mit Antennen und die zirkulardichroische Signalverstärkung durchzuführen.

Im Hybridverfahren (*Top-Down/Bottom-Up*) wurden einzelne „Planet-Satellit-Nanostrukturen“ mit einer optischen Pinzette an gewünschte Positionen eines Glassubstrates aufgebracht. Um die Eignung dieser Technik anhand eines einfachen Modells zu testen, wurden Planet-Satellit-artige Nanostrukturen hergestellt, die jeweils aus einem „Goldnanopartikel-Planet“ und plättchen-förmigen „DNA Origami Satelliten“ bestanden. Diese Strukturen wurden optisch mit einer nicht resonanten Laserfalle auf ein Substrat

aufgebracht, ohne jedoch die DNA Origami Strukturen, die den plasmonisch erhitzten Nanopartikel umgaben, zu denaturieren. Der Bereich der Laserleistung, der zu keiner Zerstörung der DNA Strukturen führte, wurde durch eine Versuchsreihe, bei der Strukturen mit verschiedenen Leistungen aufgebracht wurden, ermittelt. Innerhalb diese Bereichs ist es möglich Planet-Sattelit-artige Nanostrukturen optisch auf einem Substrat anzuordnen, während die komplexe Morphologie erhalten bleibt.

1. Introduction

Ever since the American physicist Richard Feynman inspired the importance of the *physical dimension* in his famous lecture "There's Plenty of Room at the Bottom" in 1959, size engineering of matter has become an important issue in science [1]. Among many, noble metals dragged tremendous attention due to their unique optical properties when their physical size enters the nanometer scale. Recent advances in colloidal chemistry enabled preparing such *metal nanoparticles* with tunable size and shape [2,3]. Their mono-dispersed size can be precisely tuned in a range between a few and few hundreds of nanometers. Shape control is not limited to the spherical morphology, but also to anisotropic shapes, such as rods, wires, plates, tetrapods, cubes and cages [4-10]. Due to their unique electrical properties, the so called *localized surface plasmons* [11], metal nanoparticles are widely used in different applications. Large effective cross-sections makes metal nanoparticles be considered as efficient absorbers in organic solar cells [12], or bright scattering markers for single molecule tracking [13]. Highly sensitive plasmonic resonance frequency of the metal nanoparticles to the surrounding environment allows the detection of small localized dielectric property changes, such as the binding of molecules and particle aggregation [14,15]. Feeble fluorescence and Raman signal from chemical substances can be amplified by enhanced electric field in the vicinity of metal nanoparticles and thus enables the detection of substances down to the single-molecule level [16-19]. Versatile surface functionality and plasmonic heating of metal nanoparticles makes it possible to use them as ideal materials for medical and pharmaceutical therapies [20-22].

For the realization of photonic devices and sensors to fully utilize such optical properties of metal nanoparticles, the precise nanoscopic spatial arrangement of metal nanoparticles on a solid support is important. Several nanofabrication methods were suggested for the spatial arrangement control, which can be categorized as ‘*top-down*’ and ‘*bottom-up*’ approaches [23-25]. In the *top-down* approach, the spatial

arrangement control of nanostructures are realized by either cutting and shaping bulk materials into nano-scale structures, or positioning and orientating individual nanostructures directly on a solid support. Various methods are being used in the *top-down* approach, however electron beam-, scanning probe- and photo- lithography techniques are the most commonly used [26-29]. Although these techniques yield metal nanostructures with precise shape and well-defined location over macroscopic length scales, they often have low-throughput and require expensive facilities. Also, the resulting nanostructures usually have poor surface roughness and crystallinity. Alternatively, in the *bottom-up* approach, colloidal metal nanoparticles are self-organized into two- or three- dimensional metal nanostructures driven by various physical and chemical forces between them [30-34]. Colloid chemistry allows preparing single-crystalline metal nanoparticles with various shapes and tailored surface functionality. Due to their monodispersity in size and shape, the resulting self-organized nanostructures form highly ordered arrays of metal nanoparticles with well-defined inter-particle distances and orientation. However, the nature of the self-assembly approach makes the precise location and orientation control difficult when it comes down to single particle manipulation. Despite of these limitations, the bottom-up approach is also widely used as a nanofabrication method owing to its high throughput and cost-effectiveness compared to the *top-down* approaches.

Recently, a **tightly focused laser beam** was used to deposit metal nanoparticles on a glass substrate as an alternative *top-down* nanofabrication method [35,36]. The technique used the strong scattering force resulting from the interaction between a resonant single wavelength laser and the surface plasmon of metal nanoparticles, to accelerate individual colloidal metal nanoparticles along the laser propagation direction. This all-optical printing allowed the metal nanoparticle to be deposited at a desired location on a glass substrate with a printing accuracy of few tens of nanometers. In contrast to the other methods in top-down approach, this technique allows creating metal nanostructures on a glass substrate in a relatively faster and easier without involving any post chemical processing.

On the other hand, the **DNA origami technique** has been suggested as one of the *bottom-up* approaches to build complex shaped nano-sized objects which cannot be realized by conventional nanofabrication methods [37]. A 7-kilobase long single-stranded ‘scaffold’ DNA was folded into pre-programmed two dimensional nano-objects by help of multiple short DNA staples. Upon thermal annealing process, each DNA staple is hybridized with scaffold DNA and forms approximately 6 nm sized single module which serves as a building-block to construct the final DNA origami structure with a dimension of 100 nm. Moreover, complex patterns, such as words and images were spatially addressed on the DNA origami objects by employing DNA dumbbell hairpins.

In this thesis, the nanoscopic control of the spatial arrangement of metal nanoparticles on substrates was carried out by employing the two previously-mentioned nanofabrication techniques: **tightly focused laser beam** and **DNA origami technique**. Three different approaches are investigated by adapting the techniques either individually or combined, categorizing them as *top-down*, *bottom-up* and *hybrid top-down/bottom-up*.

The fundamentals of metal nanoparticles and DNA nanotechnology are explained in Chapter 2. The resulting phenomenon of light-metal interaction, such as surface plasmon, optical forces, and optical heating in metal nanoparticles are introduced in the first three sub-chapters. In the last sub-chapter, fundamentals of DNA and its use in structural DNA nanotechnology are introduced followed by a description of the state-of-the-art DNA origami technique.

In Chapter 3, spectroscopic and microscopic techniques commonly used for the characterization and preparation of nano-scale objects are explained. Computational analyses, finite-element, and finite-differential time-domain methods, are also briefly introduced. In the last part, design and purification tools for the preparation of DNA origami structures are explained.

In the first part of Chapter 4, a *top-down* two-color laser printing technique is used to control the spatial location and angular orientation of optically printed gold nanorods. To find an optimum laser wavelength in this technique, the interplay between two plasmon modes of gold nanorods and the laser wavelength of two independent lasers is studied. Finally, the effect of the relative alignment and power of two lasers on the angular printing precision are experimentally investigated.

In the second part of Chapter 4, a tightly focused single wavelength laser beam is used to optically print individual gold nanoparticles onto the defect of a two dimensional silicon nitride photonic crystal nanocavity. The optimization of the sample and the printing setup, as well as the resulting printing precision is discussed. The interaction between the fundamental nanocavity mode and the plasmon mode of the gold nanoparticle in this hybrid structure is studied by using finite-differential time-domain modeling.

In Chapter 5, metal nanoparticles are arranged to form a planet-satellite like nanostructure based on the *bottom-up* DNA origami technique. First, a detailed preparation of each component and their assembly into the planet-satellite type nanostructures are thoroughly explained. Also, the possibilities of morphological tuning of hierarchically assembled nanostructures, such as composition, inter-particle distance and stoichiometry between planet and satellite metal nanoparticles are investigated. By employing different types of materials, such as metal nanoparticles, quantum dots, and fluorescent dyes, hetero-nanostructures are prepared. Their use in fundamental studies on distance-dependent fluorescence quenching of dyes/gold, light harvesting in antenna structure, and signal enhancement of circular dichroism are also discussed.

In Chapter 6, planet-satellite type nanostructures are all-optically deposited on a substrate by using optical tweezers. This ‘soft-optical deposition’ technique is a hybrid nanofabrication method that results from the combination of both the *bottom-up* DNA origami technique and the *top-down* optical tweezers technique. Assembled complex shaped planet-satellite type nanostructures are individually trapped by using

an off-resonant wavelength laser and further deposited onto an oppositely charged substrate without denaturing the DNA origami structures surrounding the plasmonically heated gold nanoparticles. The applicable trapping laser power range is experimentally determined by performing such a soft-optical deposition technique in different laser powers.

2. Fundamentals

In this chapter the fundamental background of metal nanoparticles and DNA nanotechnology are introduced. In the first part, the basic theoretical description of the interaction between metal nanoparticles and electromagnetic wave is explained. The resulting unique optical property of metal nanoparticles, the so called localized surface plasmon resonance, is described by using dielectric function. Also, the optical forces exerting on the metal nanoparticles exposed to focused laser beam are explained. Thermalization of metal nanoparticles resulting from the non-radiative decay of localized surface plasmon resonance is described. In the last part, the basics of deoxyribonucleic acid (DNA) are explained followed by introducing the structural DNA nanotechnology.

2.1 Optical properties of metal nanoparticles

One of the first known usages of colloidal gold dates back to the 4th-century in the Roman glass cage cup, Lycurgus cup[38]. This archeologically valuable cup shows dichroic optical properties which depends on the illumination direction due to the presence of small amount of gold nanoparticles with sizes are below 100 nm [39]. However, the use of colloidal gold in various applications in history, such as glass coloring [40], medicine [41] were based on empirical trials without fully understanding of its chemical and optical properties.

The first pure colloidal gold was prepared by British chemist Michael Faraday in 1850s by reducing gold chloride with phosphorus [42]. In contrast to the golden shiny appearance of bulk gold, nanometer-sized colloidal gold nanoparticles show different optical properties as a highly scattering reddish solution. Much research has gone into understanding and improving on the chemistry of colloidal gold [43,44], and the first exact theoretical description of the absorption and scattering properties of gold nanoparticles was suggested by Gustav Mie in 1908 [45].

Dielectric response of matter to light

When light interacts with matter, the inherent properties of the matter play a big role. Depending on the properties, some matter is highly responsive and the absorption, reflection, refraction, and scattering of the light results. Other matter, however, transmits light without interactions. Among light-responsive matter, metals have received great attention due to their opaque and shiny appearance [46]. Along with their unique optical properties, great electrical and thermal conductivities make metals highly important materials for mankind.

The unique optical and physical properties of metals originate from electrons that loosely bound to the nuclei, the so called *quasi-free electrons* [47]. One of the

straightforward ways to describe optical and electrical properties of metals is their dielectric response ϵ_r . Dielectric response, in definition, is a material property denotes how strongly the matter can be affected by an external electric field. To describe dielectric response of metals to the stimulating electric field, the macroscopic polarization \mathbf{P} need to be considered first. In macroscopic point of view, the universal polarization of matter can be expressed as $\mathbf{P} = -Nex$, where e is unit charge, N is density of charge, and x is charge displacement. N and e are material parameters which are only dependent on their chemical composition (i.e. $N_{\text{Au}} = 4.9 \times 10^{28} \text{ m}^{-3}$ and $e = 1.602 \times 10^{-19} \text{ C}$). However, the charge displacement of electrons x is highly dependent on the frequency and amplitude of the external electric field. To link the external electric field and the dielectric response, it is necessary to adopt an equation which describes the relationship between the dielectric response and the universal polarizability.

The macroscopic Maxwell's equations established by the Scottish physicist in 1860s provides the relationship between external electromagnetic field and the resulting induced electromagnetic field. [48]. In the following Maxwell's equations (2.1 – 2.4) describe the evolution of the resulting electric and magnetic field with charge density ρ and current density \mathbf{J} :

$$\nabla \cdot \mathbf{D} = \rho, \quad (2.1)$$

$$\nabla \cdot \mathbf{B} = 0, \quad (2.2)$$

$$\nabla \times \mathbf{E} = -\frac{\partial \mathbf{B}}{\partial t}, \quad (2.3)$$

$$\nabla \times \mathbf{H} = \frac{\partial \mathbf{D}}{\partial t} + \mathbf{J}, \quad (2.4)$$

where \mathbf{D} is dielectric displacement, \mathbf{E} is electric field, \mathbf{B} is magnetic flux density, and \mathbf{H} is magnetic field. With Maxwell equations, the external electromagnetic field (\mathbf{E} and \mathbf{B}) can be correlated with two new fields (\mathbf{D} and \mathbf{H}). By employing two macroscopic material parameters ϵ_0 and μ_0 , and two vector fields: magnetization \mathbf{M}

and polarizability \mathbf{P} , the average macroscopic interaction between the external and induced fields can be described by the following equations (2.5) and (2.6):

$$\mathbf{D} = \varepsilon_0 \mathbf{E} + \mathbf{P} = \varepsilon_0 \varepsilon_r \mathbf{E} \quad (2.5)$$

$$\mathbf{H} = \mu_0^{-1} \mathbf{B} - \mathbf{M} = \mu_0^{-1} \mu_r^{-1} \mathbf{B} \quad (2.6)$$

where ε_0 is the vacuum permittivity and μ_0 is the vacuum permeability with their values of 8.854×10^{-12} F/m, and 1.257×10^{-6} H/m, respectively. ε_0 and μ_0 can be a scalar or a tensor depending on the materials isotropicity.

The last expressions in the above equations are valid if the media is linear, isotropic and nonmagnetic. This constitutive realtions further provide the relationship between macroscopic polarization and external electric field with dielectric response as one of its variable:

$$\mathbf{P} = -Nex = \varepsilon_0 (\varepsilon_r - 1) \mathbf{E}. \quad (2.7)$$

Thus, the dielectric response ε_r of matter is:

$$\varepsilon_r = 1 - \frac{Nex}{\varepsilon_0 \mathbf{E}}. \quad (2.8)$$

As mentioned earlier, the charge displacement of electrons is strongly related to the oscillating external field. Therefore, more detailed description of the dielectric response of matter to the light is possible by employing the Drude-Sommerfeld model. The model provides a basic theoretical description of the motions of electrons, the so called *free electron gas* [49-51]. In this theory, the collisions between electrons and the fixed ion cores are only taken into account. Therefore further realistic interactions, such as electron-electron collision and attractive electron-ion core interaction are neglected. This assumption allows the calculation of the overall behavior of the electrons simply by multiplying the single electron behavior by the electron density of the system. The free electron motion $\mathbf{x}(t)$ in matter subjected to an oscillating

external electric field is described by equation (2.9), where m_e is electron mass and external field $\mathbf{E}_0 e^{-i\omega t}$ with its frequency (ω) and amplitude (\mathbf{E}_0).

$$m_e \frac{\partial^2 \mathbf{x}}{\partial t^2} + m_e \Gamma \frac{\partial \mathbf{x}}{\partial t} = -e \mathbf{E}(t) = -e \mathbf{E}_0 e^{-i\omega t} \quad (2.9)$$

Under an external electric field, accelerated electrons can travel for a certain amount of time without collisions, the so called mean free time τ_e . The damping constant Γ is defined as the reciprocal of mean free time. Typically, the damping constant of metal is a few tens of THz at ambient temperature [52,53]. The solution of the above equation contains the complex amplitude of motion \mathbf{x}_0 and the phase shift between the driven electron oscillations and the external oscillating electric field, as shown in equation (2.10).

$$\mathbf{x}(t) = \mathbf{x}_0 e^{-i\omega t} = \frac{e}{m_e(\omega^2 + i\Gamma\omega)} \mathbf{E}_0 e^{-i\omega t} \quad (2.10)$$

The obtained electron charge displacement can be inserted into equation (2.8). The dielectric response of matter to the external electric field can then be described as a function of the electric field frequency.

$$\epsilon_r(\omega) = 1 - \frac{Ne^2}{\epsilon_0 m_e (\omega^2 + i\Gamma\omega)} = 1 - \frac{\omega_p^2}{\omega^2 + i\Gamma\omega} \quad (2.11)$$

In the simplified form, the plasma frequency of the free electron gas $\omega_p^2 = Ne^2/\epsilon_0 m_e$ is used [54]. Plasma frequency is a material property which gives further insight on the light-matter interaction. Depending on the frequency of the illuminating light to the matter, the sign of real part of dielectric function can change. With frequencies higher than the plasma frequency, the real part of dielectric constant is positive but becomes negative at lower frequencies. At higher frequencies, the collective motion of electrons cannot follow the rapid oscillation of the electric field, therefore light passes through matter without interaction. However, below the plasma frequency, the electric field is sufficiently slow to interact with electrons and results in the reflection or absorption of light by the matter. As an example, radio signal travels either long

distance or short distance depending on its frequency. Low frequency 'amplitude modulation' (AM) signal travels longer distance due to their high reflectance at the outermost layer of earth's atmosphere which consists of ionized matter. On the other hand, high frequency 'frequency modulation' (FM) signal is not reflected, but rather transmitted through the outermost layer and thus could travel in short distance.

To extend the derived dielectric response to the noble metals (includes gold, silver and copper), the background permittivity ϵ_b needs to be implemented into equation (2.11). The extended dielectric response equation (2.12) takes into account the polarization effect of the d -band electrons, which are close to the Fermi surface, by employing the background permittivity ϵ_b [54]. Moreover, to access more realistic information of the electron motion, the electron mass can be substituted by the effective mass m^* in the plasma frequency term.

$$\epsilon_{Drude}(\omega) = \epsilon_b - \frac{\omega_p^2}{\omega^2 + i\Gamma\omega} \quad (2.12)$$

The validity of the above equation in metals can be verified by comparing it with the measured dielectric functions from the work of Johnson and Christy in 1972 [55]. In their study, the dielectric function of gold and silver are measured under ultrahigh vacuum conditions.

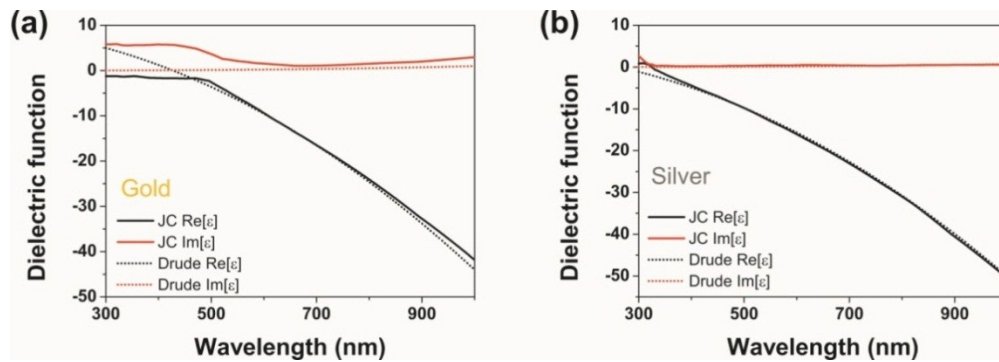


Figure 2.1 Plot of calculated and measured dielectric function of (a) gold and (b) silver based on the Drude-sommerfeld model and the experimental data from Johnson and Christy. $\epsilon_b=9.84$ (gold), $\epsilon_b=3.7$ (silver), $\omega_p=1.38 \times 10^4$ THZ, $\tau=2.9 \times 10^{-14}$ s (gold) and $\tau=4.0 \times 10^{-14}$ s (silver).

In figure 2.1 measured (Johnson and Christy) and calculated (Drude model) real and imaginary parts of the dielectric constants are compared for both gold and silver. The modeled real part of the dielectric constant of both gold and silver fairly agree in the visible wavelength. However, particularly in the case of gold, the modeled imaginary part of the dielectric constant fails over the visible wavelength. This failure, in turn, tells that there is a non-negligible effect from the interband transition of electrons between the lower lying d-band and sp-band of gold [56]. Therefore, in the calculation of optical properties of noble metal structure, either the theoretical or experimental value is used depending on the region of validity.

Localized surface plasmon resonance of metal nanoparticles

Up to now, we have discussed the dielectric response of matter upon an external oscillating electromagnetic wave. However, in the case of metals, when the physical size of metals becomes smaller than the wavelength of the incident light, the dielectric response is different than its bulk form. When metal nanoparticles are illuminated with light, the spatial phase of the induced electron oscillation becomes nearly uniform over the particle due to the negligible external field intensity difference over its volume [57]. Moreover, the induced electron oscillation is spatially confined by the physical size of metal nanoparticles by the restoring force from the electron-ion interaction. The consequence of the size confinement of the collective electron oscillation (plasmon) in sub-wavelength sized metals is called the *localized surface plasmon resonance*, as shown in figure 2.2.

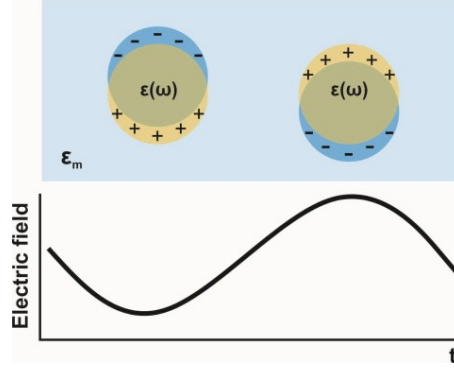


Figure 2.2 Localized surface plasmon resonance in spherical gold nanoparticles exposed to the external electromagnetic wave. Dielectric function of gold nanoparticles is $\epsilon(\omega)$, and ϵ_m is dielectric constant of medium.

To describe the localized surface plasmon resonance of metal nanoparticles, we assume that there is a single spatial phase of electrons that appears in sub-wavelength sized spherical metal nanoparticles under an external electromagnetic field. This assumption, the so called the *quasi-static approximation* [58], allows us to determine the polarizability α which is a very useful physical property of metal nanoparticles for describing their localized surface plasmon resonance. To this end, the dipole moment \mathbf{p} is defined in equation (2.13) with polarizability as one of variables.

$$\mathbf{p} = \epsilon_0 \epsilon_m \alpha \mathbf{E}_0 \quad (2.13)$$

In this equation, the dipole moment is closely correlated with the magnitude of the external electric field \mathbf{E}_0 , where ϵ_0 and ϵ_m are the dielectric constants of vacuum and the surrounding medium, respectively. We assume a spherical metal nanoparticle with a radius of a surrounded by a non-magnetic and isotropic medium. Using spherical coordinates with radius r and angle θ , the electric potential inside and outside the sphere can be written as equation (2.14) and (2.15), respectively, by using two boundary conditions at $r = a$ and $r = \infty$ [54]:

$$\Phi_{\text{in}} = -\frac{3\epsilon_m}{\epsilon + 2\epsilon_m} \mathbf{E}_0 r \cos \theta \quad (2.14)$$

and

$$\Phi_{\text{out}} = -\mathbf{E}_0 r \cos \theta + \frac{\varepsilon - \varepsilon_m}{\varepsilon + 2\varepsilon_m} \mathbf{E}_0 a^3 \frac{\cos \theta}{r^2}. \quad (2.15)$$

The equation of electric potential outside the sphere contains not only the applied field in its first term but also the induced dipole moment in its second term. By employing the general dipole potential expression in equation (2.16), the induced dipole moment at the center of the metal sphere can be described as equation (2.17):

$$\Phi_{\text{Dipole}}(r) = \frac{\mathbf{p} \cdot \mathbf{r}}{4\pi\varepsilon_0\varepsilon_m r^3} = \frac{\mathbf{p}r \cos \theta}{4\pi\varepsilon_0\varepsilon_m r^3} = \frac{\varepsilon - \varepsilon_m}{\varepsilon + 2\varepsilon_m} \mathbf{E}_0 a^3 \frac{\cos \theta}{r^2} \quad (2.16)$$

and

$$\mathbf{p} = 4\pi\varepsilon_0\varepsilon_m a^3 \frac{\varepsilon - \varepsilon_m}{\varepsilon + 2\varepsilon_m} \mathbf{E}_0. \quad (2.17)$$

By inserting derived induced dipole moment into equation (2.13), the polarizability of a spherical metal nanoparticle surrounded by a medium can be described as equation (2.18) with the physical volume of the metal sphere and the dielectric functions of both the metal and medium as its variables. This expression of polarizability is called Clausius-Mossotti equation.

$$\alpha = 4\pi a^3 \frac{\varepsilon - \varepsilon_m}{\varepsilon + 2\varepsilon_m} \quad (2.18)$$

This equation tells us that the polarizability of a metal sphere can be highly dependent on the wavelength of light which, in turn, can vary the dielectric constant of the metal significantly. In figure 2.3 the real and imaginary parts of the polarizability of 20 nm gold and silver nanoparticles in water are plotted as a function of wavelength. In this plot, the dielectric functions of gold and silver are taken from the Johnson and Christy experiments. It can be clearly seen that the response of gold and silver are

highly different depending on the wavelength: silver responds actively to the light with shorter wavelength while gold responds to the longer wavelength light.

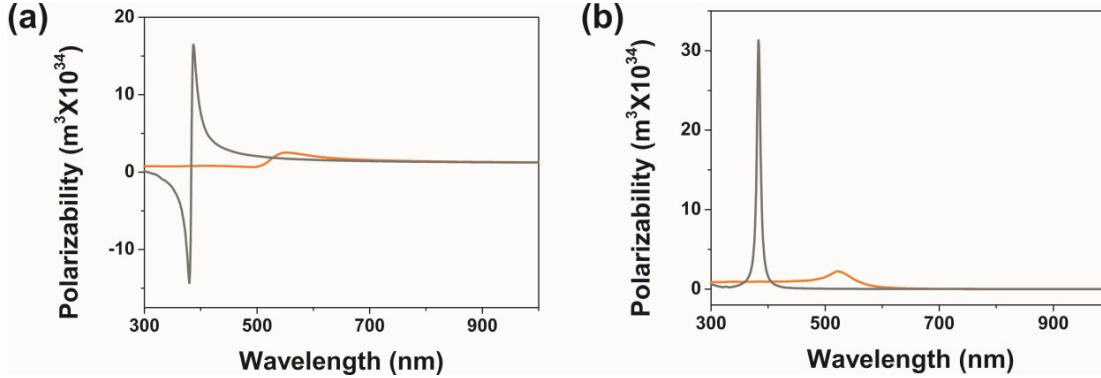


Figure 2.3 Plot of (a) real and (b) imaginary polarizability of 20 nm gold (colored yellow) and silver (colored grey) nanoparticles.

However, with Clausius-Mossotti equation, the physical size of metals influences only the amplitude of polarizability, not their response with respect to the wavelength of the light. Consequently, the effective cross-sections of metal nanoparticle (which are closely related to polarizability) do not reflect the size effect of metal nanoparticles if the polarizability is calculated from Clausius-Mossotti equation. In figure 2.4, the normalized calculated (Clausius-Mossotti equation) and measured extinction cross-sections of 20 and 80 nm gold nanoparticles are plotted. The cross-sections of metal nanoparticles are conveniently derived from equation (2.19) and (2.20) [54,57].

$$\sigma_{\text{ext}} = k\text{Im}[\alpha] \quad (2.19)$$

$$\sigma_{\text{sca}} = \frac{k^4}{6\pi} |\alpha|^2 \quad (2.20)$$

In the measured extinction cross-section, the peaks shift to longer wavelengths with the size of metal nanoparticles. However, in the calculated one, the peak maxima are independent of the size of the metal nanoparticles.

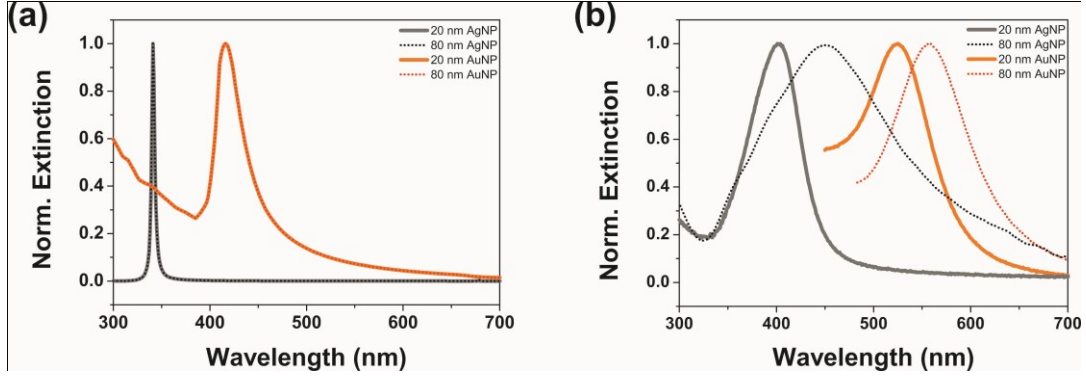


Figure 2.4. (a) Calculated (Clausius-Mossotti equation) and (b) measured extinction cross-section of differently sized gold (colored orange) and silver (colored grey) nanoparticles.

To overcome this limitation, it is necessary to consider not only the dipole (in the case of quasi-static approximation) but also higher order multipoles. This consideration was suggested by Gustav Mie in 1908 [45]. In his theory, the contribution of the multipole is no longer negligible when the size of the sphere becomes bigger than $\lambda/10$, where λ is the wavelength of incident light. Taking into account multipoles, the scattering and extinction cross-sections of metal spheres can be described with equations (2.21) and (2.22) by using boundary conditions at the interface of the sphere and the surrounding medium, where the radius of metal sphere is a .

$$\sigma_{\text{ext}} = \frac{2\pi}{|k|^2} \sum_{n=1}^{\infty} (2n+1) \text{Re}(|a_n|^2 + |b_n|^2) \quad (2.21)$$

and

$$\sigma_{\text{sca}} = \frac{2\pi}{|k|^2} \sum_{n=1}^{\infty} (2n+1)(|a_n|^2 + |b_n|^2) \quad (2.22)$$

In above equation, k is the wave number of incident light, and the scattering coefficients a_n and b_n are defined in the equations (2.23) and (2.24) below:

$$a_n = \frac{m\psi_n(mx)\psi_n'(x) - \psi_n(x)\psi_n'(mx)}{m\psi_n(mx)\xi_n'(x) - \xi_n(x)\psi_n'(mx)} \quad (2.23)$$

and

$$b_n = \frac{\psi_n(mx)\psi_n'(x) - m\psi_n(x)\psi_n'(mx)}{\psi_n(mx)\xi_n'(x) - m\xi_n(x)\psi_n'(mx)} \quad (2.24)$$

where m is the relative refractive index ($m = n/n_m$), and x is the size parameter of the sphere $x = 2\pi a/\lambda$ and ψ_n and ξ_n are the Riccati-Bessel functions. Since the scattering coefficient equation takes into account the size parameter of sphere, the resulting cross-section values from Mie theory shows size dependency, as plotted in figure 2.5. It is clearly seen that the peak maxima of the extinction and scattering cross-sections shift to the longer wavelength with the size of gold nanoparticles. Also, the magnitude of the cross-sections are increased with respect of the nanoparticle size.

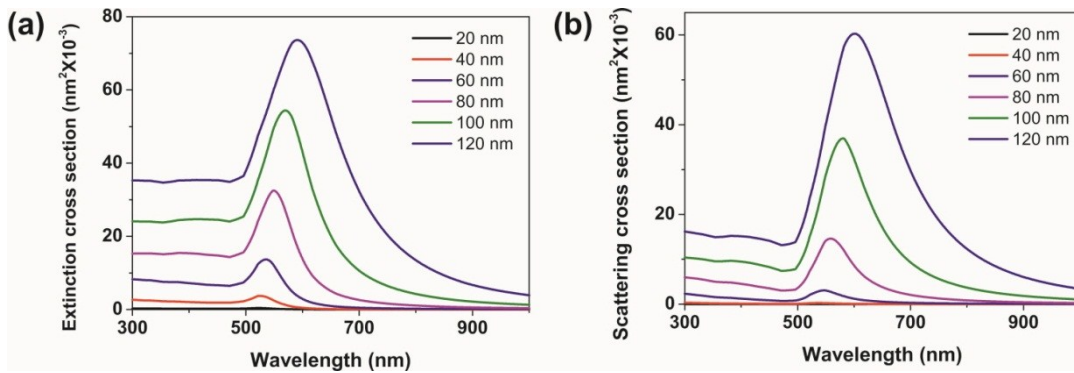


Figure 2.5 Calculated (Mie theory) extinction and scattering cross-sections of differently sized gold nanoparticle in water.

Although Mie theory provides exact effective cross-sections of the metal nanoparticles with size larger than $\lambda/10$, it does not deliver polarizability value. The polarizability of metal nanoparticles are essential values for optical forces calculation, which will be done in the next section. Moreover, as mentioned earlier, the calculated polarizability from the Clausius-Mossotti equation cannot assess retardation effects [59,60], which is strongly governed by the size of metal nanoparticles. To estimate

the polarizability of metal nanoparticles with arbitrary size, equation (2.18) is extended into equation (2.25) [61].

$$\alpha = a^3 \frac{1 - \frac{1}{10}(\varepsilon + \varepsilon_m)x^2 + O(x^4)}{\left(\frac{1}{3} + \frac{\varepsilon_m}{\varepsilon - \varepsilon_m}\right) - \frac{1}{30}(\varepsilon + 10\varepsilon_m)x^2 - i \frac{2}{9} \varepsilon_m^{3/2}x^3 + O(x^4)} \quad (2.25)$$

This extended quasi static approximation equation includes the size parameter $x = 2\pi a/\lambda$ and higher orders of size parameter $O(x^4)$, where a and λ are the radius of metal nanoparticle and the wavelength, respectively. The calculated polarizability obtained from equation 2.25 can provide nearly identical effective cross-sections compared to the one from Mie theory in terms of the peak maxima and the magnitude. All the force calculation in this thesis are performed by using polarizabilities which are obtained from this extended quasi-static approximation.

2.2 Optical forces on metal nanoparticles in a focused laser beam

Size regimes in optical forces

When microscopic objects are illuminated by a tightly focused light, they can be either trapped or repelled depending on the material parameters and the wavelength of light [62,63]. One of the material parameters which influences this the most is physical size r . Generally, their interaction can be categorized into two regimes depending on the relative difference between the wavelength λ and the physical size of object r . In these two regimes, the origin of the optical forces are different as illustrated in figure 2.6.

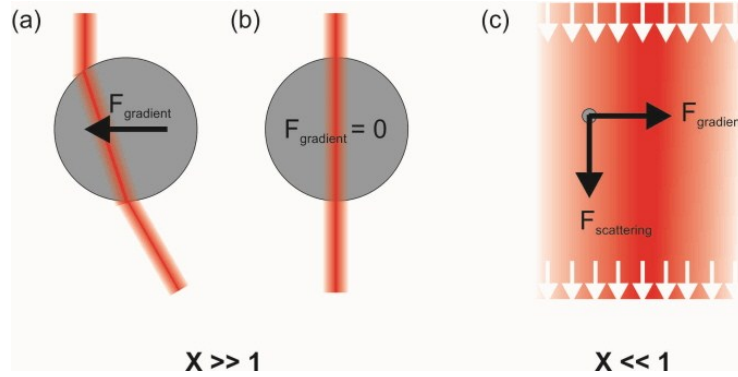


Figure 2.6 Optical forces exerting on the object with the size included in (a, b) Ray optics regime or (c) Rayleigh scattering regimes.

In the first regime where the particle size is much bigger than the wavelength of the beam ($\lambda \gg r$), particle behavior can be explained by momentum changes [64]. When individual rays of light hit the particle, they are refracted and exit the particle in different directions from their incident direction due to the refractive index mismatch between the particle and medium. As shown in figure 2.6a, the exiting light brings a momentum change which has equal magnitude but acts in the opposite direction. Therefore, if a particle center is away from the region where the intensity is highest, the exerting optical force brings it back to the initial position (figure 2.6b). In the case of a tightly focused light, the particle will reside at the focus where net momentum change become zero, hence enabling objects to be trapped solely with light.

If the size of the object is much smaller than the beam size ($\lambda \ll r$), the most distinct interaction is the scattering of light from the object [65], which is proportional to the particle size (r^6) and the illuminated laser wavelength ($1/\lambda^4$). The blue sky and orange sunsets are the consequence of light scattering by small molecules in the atmosphere in this regime. The oscillating electric field of light acting on small objects makes it oscillate resonantly to the light frequency, which results in the radiation of electromagnetic waves with a certain frequency. Since the object in this regime can be assumed to be point charge, the force acting on this object follows the Lorentz force [66] which describes the force exerting on a charged particle moves in an electromagnetic field.

The two regimes described above are named Ray optics and Rayleigh scattering region, respectively. There is also an intermediate regime, the so called Mie regime, where particle size is close to the wavelength of light. Most of the samples used in this thesis can be included in the Mie regime since their physical size is close to the wavelength of the manipulation lasers. However, to describe the force in this region the interaction should first be approximated as either Ray optics or Rayleigh scattering for the convenience.

Optical forces acting on gold nanoparticles

To assess the optical force acting on gold nanoparticles, we consider them as point dipoles, such as in the case of the Rayleigh scattering regime. In this assumption, when a charged particle q moves in an electromagnetic field with a speed of v , the Lorentz force acting on the particle can be described :

$$\mathbf{F}_{\text{Lorentz}} = q(\mathbf{E}(\mathbf{r}, t) + \mathbf{v}(\mathbf{r}, t) \times \mathbf{H}(\mathbf{r}, t)), \quad (2.26)$$

where, \mathbf{E} and \mathbf{H} are the electric and magnetic field, respectively. Taking into account Maxwell's equations, vector equality and the dipole approximation ($\mathbf{p} = \varepsilon_0 \varepsilon_m \alpha \mathbf{E}$), the total force \mathbf{F} can be written as:

$$\mathbf{F}_{\text{total}} = \varepsilon_0 \varepsilon_m \alpha \left[\sum_j E_j \nabla E_j + \mu \frac{\partial(\mathbf{E} \times \mathbf{H})}{\partial t} \right]. \quad (2.27)$$

The averaged total force over the optical period $T = 2\pi/\omega$ with complex polarizability can be written as:

$$\langle \mathbf{F}_{\text{total}} \rangle = \frac{1}{4} \varepsilon_0 \varepsilon_m \alpha' \nabla(\mathbf{E}^* \cdot \mathbf{E}) + \frac{1}{2} \varepsilon_0 \varepsilon_m \alpha'' \text{Im} \left(\sum_j E_j^* \nabla E_j \right). \quad (2.28)$$

First and second terms in the above equation denote two different components of the total force, so called gradient force and scattering force, respectively. Gradient force acts along the intensity gradient of the light and its magnitude is proportional to the real part of the complex polarizability. On the other hand, scattering force acts along the poynting vector of the electromagnetic field of the light, thus it follows the laser propagation direction. The magnitude of the scattering force is proportional to the imaginary part of the complex polarizability. Since the two forces can act in different directions, small changes in the magnitude of the individual forces significantly affect the magnitude and direction of the total force. Especially when a tightly focused laser illuminates the particles, this effect becomes tremendous due to the rapid intensity changes near the laser focus. The behavior of particles at the laser focus can be divided into two different regimes, *optical trapping* and *optical printing*. In the optical trapping regime, the gradient force becomes dominant in terms of magnitude of the forces. To achieve such a condition, the magnitude of the scattering force should be minimized while maximizing the gradient force. In order to tune the magnitude of the two forces, it is necessary to consider the complex polarizability of gold nanoparticles as a function of wavelength. Figure 2.7 shows the real and imaginary parts of the polarizability of 80 nm gold nanoparticles in water. With a laser wavelength above 700 nm, the real part of the polarizability becomes larger than the imaginary part. Therefore, at such wavelengths, an 80 nm gold nanoparticle can be optically trapped at the laser focus where the laser intensity is highest.

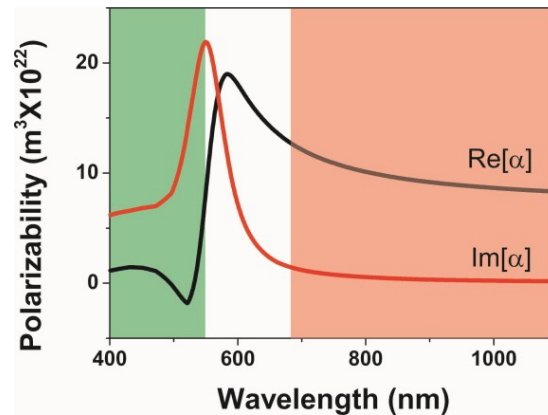


Figure 2.7 Complex polarizability of 80 nm gold nanoparticles. Optical printing and optical trapping regimes are colored green and red, respectively.

However, when the laser wavelength is below 600 nm, where the magnitudes of the real and the imaginary polarizabilities are reversed, an 80 nm gold nanoparticle will be propelled from the laser focus. In this optical printing regime, the scattering force becomes bigger than the gradient force. Therefore, an 80 nm gold nanoparticle will be pushed along the laser propagation direction. This propulsion of gold nanoparticles can be enhanced even more when the real part of the polarizability is negative. Light in this wavelength range not only pushes a gold nanoparticle by the strong scattering force but also repels it from the laser focus with an oppositely acting gradient force.

Optical forces in tightly focused laser beam

To assess the magnitude and direction of the forces acting on the gold nanoparticles inside a tightly focused laser beam, the exerting electric field is first considered as a Gaussian distribution of the laser (TEM₀₀ mode). The spatial distribution of the electric field is approximated below in equation (2.29) with z and r , which are the distances from the laser focus along the beam axis and image plane, respectively [67].

$$E(r) = E_0 \sqrt{\frac{2}{\pi}} \frac{w_0}{w(z)} \exp\left(-\frac{r^2}{w^2(z)}\right) \exp\left(i \frac{k_m r^2}{2R(z)}\right) \exp(ik_m z + i\eta(z)) \quad (2.29)$$

In the above equation, $k_m = 2\pi/\lambda$ is the angular wavenumber of the focused laser and $w(z)$, $\eta(z)$, and $R(z)$ are defined in following individual equations (2.30 – 2.32).

$$w^2(z) = w_0^2 \left\{ 1 + \left(\frac{z}{z_0}\right)^2 \right\} \quad (2.30)$$

$$\eta(z) = \tan^{-1} \left(\frac{z}{z_0}\right) \quad (2.31)$$

$$R(z) = z \left\{ 1 + \left(\frac{z}{z_0}\right)^2 \right\} \quad (2.32)$$

The beam radius at the focal point and the length at which the beam's cross-sectional area becomes doubled are defined as $w_0 = \lambda/\pi(NA)$ and $z_0 = \pi w_0^2/\lambda$, respectively. By inserting the electric field distribution equation (2.29) into equation (2.28), the Lorenz force exerted on the gold nanoparticle can be obtained. Figure 2.8 compares the magnitude and direction of the calculated total force exerting on a 80 nm gold nanoparticle near the laser focus upon illumination of different laser wavelength. As the direction of the total force depicting, the total force acts along the laser propagation direction when a resonant wavelength laser (532 nm) is illuminated on a gold nanoparticle. However, with an off-resonant wavelength laser (1064 nm), the total force directed toward the laser focus where the highest laser intensity is present.

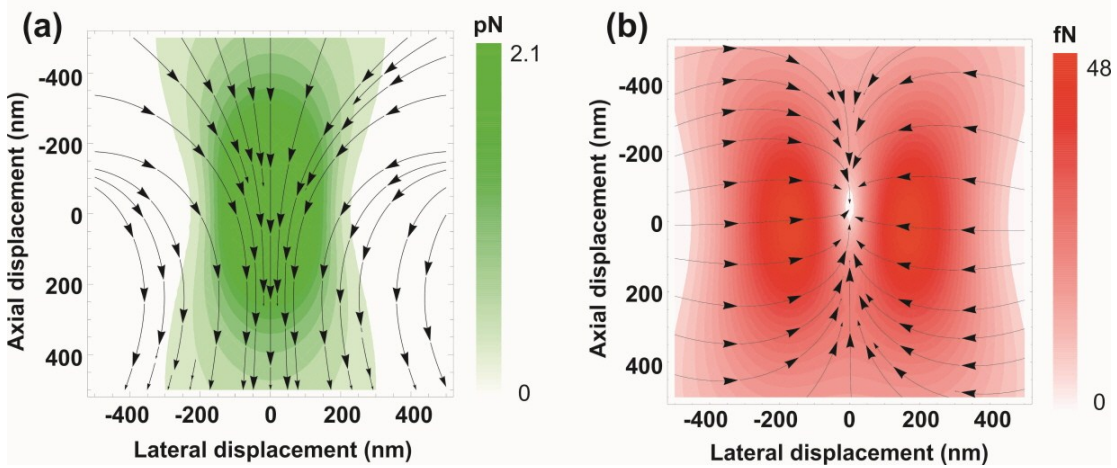


Figure 2.8 Total force map of 80 nm gold nanoparticle upon illumination of resonant and off-resonant laser at the wavelength of (a) 532 and (b) 1064 nm, respectively. The laser power is 1mW and focused with 1.0 NA objective. Laser beam propagates from top to bottom.

As can be seen in the force maps, the direction and magnitude of the force are different at each point in lateral and axial coordinates. Thus further decomposition of both forces into separate lateral r and axial z components is necessary in order to understand interplay of induced particle motion under laser illumination [67]. Firstly lateral and axial components of gradient force can be divided and written as in equations (2.33) and (2.34).

$$F_{\text{grad,axial}}(r, z) = -\frac{\varepsilon_0}{\pi} \alpha' |E_0|^2 z \frac{w_0^4}{z_0^2} \left(\frac{1}{w^4(z)} - \frac{2r^2}{w^6(z)} \right) \exp\left(-\frac{2r^2}{w^2(z)}\right) \quad (2.33)$$

$$F_{\text{grad,lateral}}(r, z) = -\frac{2\varepsilon_0}{\pi} \alpha' |E_0|^2 r \frac{w_0^2}{w^4(z)} \exp\left(-\frac{2r^2}{w^2(z)}\right) \quad (2.34)$$

In the same manner, lateral and axial component of the scattering force are described in equations (2.35) and (2.36).

$$F_{\text{scat,axial}}(r, z) = \frac{\varepsilon_0}{\pi} \alpha'' |E_0|^2 \frac{w_0^2}{w^2(z)} \left\{ k_m \left(1 - \frac{r^2(z^2 - z_0^2)}{2(z^2 + z_0^2)^2} \right) - \frac{w_0^2}{z_0 w^2(z)} \right\} \exp\left(-\frac{2r^2}{w^2(z)}\right) \quad (2.35)$$

$$F_{\text{scat,lateral}}(r, z) = \frac{\varepsilon_0}{\pi} \alpha'' |E_0|^2 \frac{w_0^2}{w^2(z)} \frac{k_m r}{R(z)} \exp\left(-\frac{2r^2}{w^2(z)}\right) \quad (2.36)$$

Force calculations in this thesis were performed by using the commercial mathematical computing program Mathematica (Wolfram research).

2.3 Laser-induced heating of metal nanoparticles

Depending on the number of gold atoms in a gold nanostructure, the relaxation process of photo-excited gold behaves differently. When subnanometer gold clusters consisting of few to few tens gold atoms are excited, relaxation occurs mainly through a radiative mechanism (photoluminescence) due to their molecular like properties [68]. On the other hand, gold nanoparticles with a size of few to few tens of nanometers, consisting of millions of gold atoms, relax via both radiative and non-radiative channels in the form of a photon and heat, respectively [69]. However, resulting light from the radiative process of gold nanoparticle relaxation is a consequence of scattering, while the photoluminescence of the gold nanoclusters is

caused by electronic transition. All gold nanoparticles which are studied in this thesis belong to the second size regime. Therefore, it is necessary to understand the two decay channels in gold nanoparticles as sketched in figure 2.9.

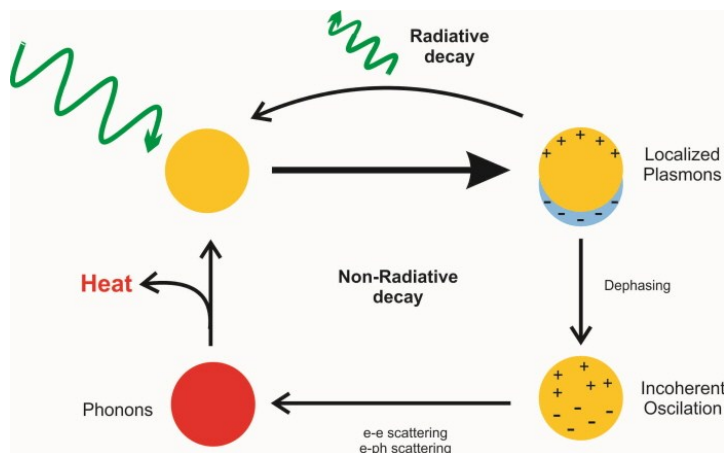


Figure 2.9 Radiative and non-radiative decays of localized surface plasmon resonance in gold nanoparticles.

When an electromagnetic wave is absorbed by the gold nanoparticle, it induces a localized surface plasmon resonance in the nanoparticle. Induced coherent oscillation of electrons in the gold nanoparticle results in elastic scattering of the incident light. Therefore the energy of the photon is preserved while its propagation direction is changed. However, the plasmon modes in gold nanoparticles can also decay via a non-radiative channel. In this case, incoherent oscillation of electrons plays a role and results in the elevated temperature of the gold nanoparticles [70]. After partial dissipation of the initial energy into photons via a radiative channel, the incoherent oscillation of electrons are scattered among them or with phonon. These electron-electron and electron-phonon collisions transform their kinetic energy into thermal energy in gold nanoparticles. This process happens within a few picoseconds [71,72], thus heat transfer from gold nanoparticles to the surrounding medium on this time scale can be negligible. Once a gold nanoparticle is heated homogeneously over its entire structure, it begins transferring its thermal energy to the surrounding medium. The transferred thermal energy increases the temperature and forms a thermal

gradient in the medium around the gold nanoparticle. This process takes place on the nanosecond time scale. After releasing the absorbed energy via scattering and thermalization, the gold nanoparticle is brought back to its initial state. However, when the excitation is continuous, there will be a thermal equilibrium state where the generated and dissipated thermal energy are balanced. Therefore the surface temperature of the gold nanoparticle will be constant in the thermal equilibrium state.

To assess the steady state surface temperature of a gold nanoparticle under continuous excitation (i.e. cw laser), the diffusion of heat from an optically heated gold nanoparticle is described by using the heat transfer equation (2.37) [73]:

$$\rho(\mathbf{r})c(\mathbf{r})\frac{\partial T(\mathbf{r}, t)}{\partial t} = \nabla k(\mathbf{r})\nabla T(\mathbf{r}, t) + Q(\mathbf{r}, t), \quad (2.37)$$

where \mathbf{r} is coordinate, t is time, T is local temperature, ρ is material density, c is specific heat, k is thermal conductivity of the surrounding and, Q is the heat source of the system. The temperature distribution in the system at the steady state within the physical volume (V), for nanoparticles surrounded by a medium with thermal conductivity k_m can be described by the equation:

$$\Delta T(\mathbf{r}) = \frac{QV}{4\pi k_m \mathbf{r}}. \quad (2.38)$$

This steady state temperature distribution is only valid when \mathbf{r} is bigger than radius of the nanoparticles. Q is calculated with known values of the absorption cross section (σ_{abs}), power density (I), and volume of nanoparticles as shown in equation (2.39).

$$Q = \frac{\sigma_{abs}I}{V} \quad (2.39)$$

Figure 2.10 shows the calculated temperature distribution around a spherical gold nanoparticle in water. In this work, effective absorption cross-sections of spherical and non-spherical nanoparticles are calculated by MQMie [74] and finite-difference time-domain modeling (Lumerical), respectively. Power density is calculated based

on measured Gaussian profiles and the power of the laser at the focal plane. The modeling of heat distribution around gold nanoparticles in the medium is performed with the commercial program COMSOL multiphysics 4.0 (FemLab). Detail principles of the finite-element method will be discussed in next chapter.

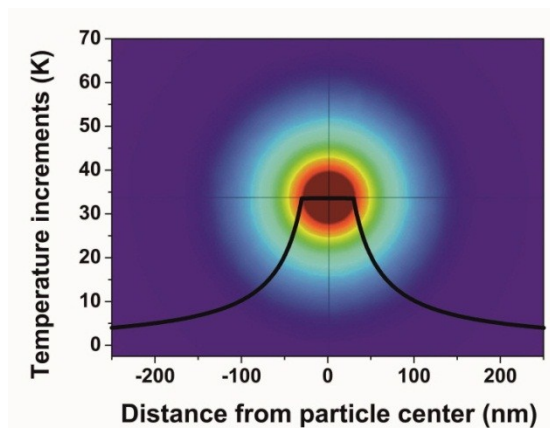


Figure 2.10 Calculated temperature distribution around 60 nm gold nanoparticles illuminated with 1064 nm laser and its power density is 229 kW/cm². The calculated absorption cross section at 1064 nm is $4.10 \times 10^{-5} \mu\text{m}^2$.

2.4 DNA nanotechnology

To function as living organisms, there are three essential macromolecules that are required; nucleic acids, proteins and carbohydrates. Among them, nucleic acids are polymeric macromolecules which transmit genetic information of living organisms to the next generation. Nucleic acids can be classified as either deoxyribonucleic acid (DNA) or ribonucleic acid (RNA) depending on their chemical structure and functions. DNA plays a main role for the long-term storage of the genetic information, whereas RNA transfers genetic code for manufacturing proteins.

First discovery of DNA goes back to the 19th century when Johann Friedrich Miescher made observations of a microscopic substance in the pus [75]. In following decades, DNA has been isolated from non-protein substances in the cell and its chemical composition has been revealed [76]. However, in those early studies, the function of DNA molecules and their exact chemical conformation were still unknown. The role of DNA in heredity was first confirmed by Hershey-Chase's experiments in 1952 [77], and its double helix structure was revealed by James Watson and Francis Crick from X-ray diffraction patterns of DNA in 1953 [78]. To commend their discovery of the DNA structure, James Watson and Francis Crick received the Nobel Prize in physiology or medicine in 1962. Following this pioneer work, extensive research has been conducted on DNA to gain a deeper understanding of their structure and functions in biological systems. Based on those fundamental studies, DNA was first considered as a structural building material beyond its original role in heredity by American scientist Nadrian Seeman in the 1990s [79].

Basics of DNA

A single DNA polymer chain consists of a series of unit molecules, or so called nucleotides [80-82]. Individual nucleotides are chemically connected via phosphodiester bonds and form long linear biopolymer chains as shown in figure 2.11. A single nucleotide is composed of a phosphate backbone, base and deoxyribose sugar [83]. The chemical structure of deoxyribose and phosphate in every nucleotide is identical but base can vary according to the type of aromatic moiety and the number of hydrogen bonding site: adenine (A), cytosine (C), guanine (G), or thymine (T) [84]. This diversity of bases and their uncountable combination of sequences in DNA polymer chains allows encoding of a large quantity of genetic information in a living organism.

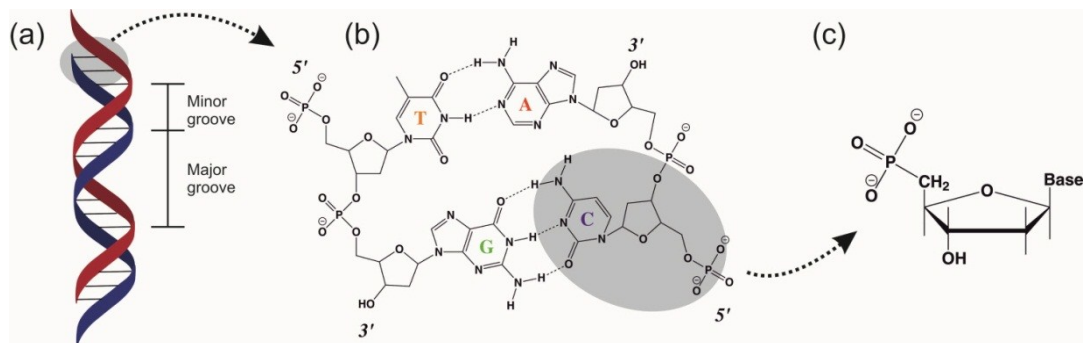


Figure 2.11 (a) The major and minor grooves in DNA double helix structure. (b) Chemical composition of four different types of nucleotide, and hydrogen bonding between complementary base pairs. (c) Three dimensional chemical structure of single nucleotide.

Typically, in nature, DNA exists in a double helix form in the nucleus [85]. Each single-stranded DNA contains millions of nucleotides, and it can be hybridized to a counterpart DNA strand having complementary sequences via hydrogen bonding. When DNA molecules form a double helix structure, they are aligned in an anti-parallel configuration, where one strand is oriented 3' to 5' while the other is oriented 5' to 3' along the first one as shown in figure 2.9b. Here the 3' end and the 5' end represent the 3'-hydroxyl group and the 5'-phosphate, respectively. In the double helix form, hydrogen bonding sites of all bases are facing to the central helix axis, whereas same charged backbones are far apart. Hence, hydrophobic aromatic moieties are clustered in the interior of the double helix while hydrophilic ionic backbones are exposed to the surrounding water molecules. This amphiphilicity makes DNA double helix stable in aqueous condition.

Due to internal polarity within a single base and their structural conformation within a strand, two base pairs are preferentially allowed, being adenine-thymine (A-T) and cytosine-guanine (C-G) pairs. Therefore adenine, which has two hydrogen bonding sites, is unlikely to be paired with guanine or cytosine, where three hydrogen bonding sites are present. Also, the number of hydrogen bonds in the base pairs also causes a small difference in bonding energy between the two different base pairs. Since cytosine and guanine are paired via three hydrogen bonds, this binding has a higher bonding energy than an adenine-thymine pair [86]. Double-stranded DNA with a high

content of cytosine-guanine pairs should have higher molecular stability. In a typical DNA double helix, alternating major and minor grooves are found. A major groove has a length of 22 nm and a minor groove a length of 12 nm. This is due to the two possible glycosidic bond angles between the base and the deoxyribose sugar of 240 degrees and 120 degrees for major and minor grooves, respectively [87]. The most common form of a DNA double helix in nature is the B-DNA form. Other forms (A-DNA and Z-DNA) also exist depending on the conditions, such as hydration level, DNA sequences, chemical modification etc [83,88]. The B-form of the DNA double helix has right handed spiral with inter-nucleotide distance of 0.34 nm and a helical pitch of 10.5 nucleotides [78].

Stability of DNA double helix

In the absence of highly alkaline histones or cations in the medium, double-stranded DNA becomes unstable due to the electrostatic repulsion between two charged backbones in the complementary DNA strands. Typically, DNA strands have a negatively charged phosphodiester bond in their polymer backbone due to its nearly zero pKa value at pH 7 [85]. Thus, the attractive hydrogen bonding which is primary force for the DNA stabilization can be disturbed by the electrostatic repulsion force, resulting in denaturing of double-stranded DNA into two single-stranded DNA. However, by having cations in the vicinity of the DNA polymer backbone, negative charges in the backbone can be electrostatically neutralized by positively charged cations, which leads to stable hybridization of the two same charged polymers even though they are close together.

The stability of a double stranded DNA is not only governed by hydrogen bonding between base pairs but is also attributed to *base stacking* between neighboring bases [89]. Between two adjacent bases, partial overlapping of the delocalized pi-electrons holds the structure more rigid. Moreover, the instantaneous dipole of each base

induces dipole-dipole interaction (so called London force) which also provides additional stability to the DNA double helix form as shown in figure 2.12.

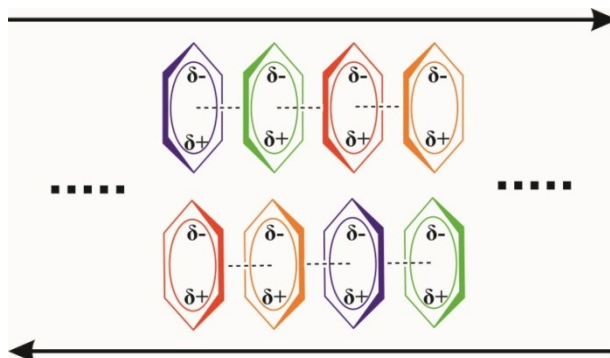


Figure 2.12 Base stacking and instantaneous dipole-dipole interaction in DNA double helix.

The thermal stability of double-stranded DNA is important since they are hybridized via hydrogen bonding and π - π stacking, which are relatively weaker than other chemical bonding, such as covalent and ionic bonding. Therefore, DNA can often be denatured at a temperature well below its chemical decomposition temperature. One of the parameters indicating the thermal stability of DNA is its melting temperature T_m . The melting temperature of double-stranded DNA is defined as the temperature where half of the bases remain paired while the others are denatured. Melting temperature can be experimentally measured by observing the magnitude of the absorption peak at 260 nm. At this wavelength, the aromatic moiety in the base absorbs light strongly, however the absorption intensity is different depending on the base pairing. In comparison to non-paired bases, bases paired via hydrogen bonding or base stacking decrease the magnitude of absorption intensity by a factor of 1.6. This magnitude changes allow us to measure the melting temperature of DNA, where rapid temperature changes are observed. Alternatively, the melting temperature of DNA can be predicted with the following equation (2.40),

$$T_m = \frac{\Delta H^\circ \cdot 1000}{\Delta S^\circ + R \cdot \ln\left(\frac{C_T}{4}\right)} - 273.15 \quad (2.40)$$

where ΔH° (kcal/mol), ΔS° (cal/mol·K), and C_T (M) and R (cal/mol·K) are change in enthalpy, change in entropy, total molar strand concentration and gas constant, respectively. The enthalpy and entropy values can be obtained from nearest-neighbor model [90].

Synthetic DNA

Naturally occurring DNA synthesis in living organism is done by several proteins, in a process called DNA replication. Here, double-stranded DNA unwinds into two individual single-stranded DNA molecules and each serves as a template for further production of replica DNA with complementary sequences. However, synthesis of DNA with special sequences and their replication can also be done in the lab using the polymerase chain reaction (PCR) technique. The programmability of DNA sequences in the lab enables DNA to be used in structural DNA nanotechnology which will be discussed in the following section. By PCR, single-stranded DNA with defined sequences can be obtained. However the number of nucleotides in single DNA chain is rather limited due to a rapidly increasing error rate when the length exceeds 60 nucleotides. Technically, manufacturing DNA longer than 60 nucleotides is possible but this requires more delicate purification steps which leads to a higher manufacturing cost.

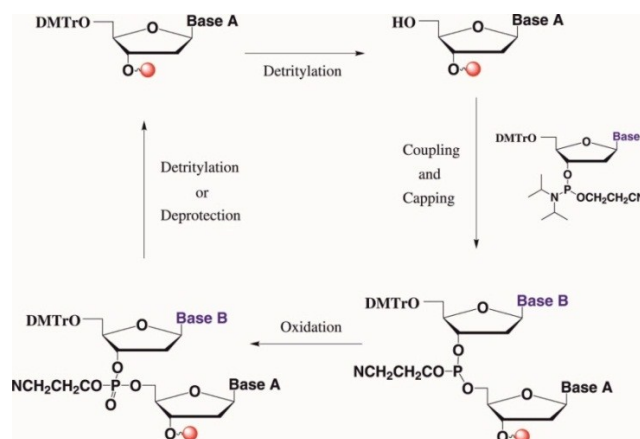


Figure 2.13 Chemical synthesis of synthetic DNA-oligonucleotides.

Synthesizing DNA oligos in the lab involves several steps, as described in figure 2.13 [91]. In the first step, the 4,4'-dimethoxytrityl (DMTr) group is removed in the presence of acid in an inert solvent such as dichloromethane or toluene. After detritylation, a 5'-terminal hydroxyl group is formed and used for a further coupling reaction. An excess amount of phosphoramidite is added into the detritylated oligonucleotide precursor, thereby two nucleotides are coupled via a phosphite triester linkage. The hydroxyl group in the unreacted precursor is capped in the presence of acetic anhydride and N-methylimidazole to avoid deletion mutation of DNA oligos. Once coupling is done, unstable tricoordinated phosphite triester is oxidized with iodine in the presence of water and weak base to generate a stable form of tetracoordinated phosphite triester. The above process is repeated for each nucleotide to produce DNA oligos with the desired length and base sequence. In the last step, the cyanoethyl group is deprotected to form a final phosphodiester linker between nucleotides, resulting in lab synthesized DNA oligos.

DNA as a building materials in structural nanotechnology

In nature, special functionality of macromolecules often arises from their structure. Protein and DNA are biological materials that have been extensively investigated in order to understand their functions in relation to their alternating structures [92,93]. Among them, the structural DNA nanotechnology is based solely on DNA hybridization. Each DNA strand is considered as a single building block and is connected to other building blocks via Watson-Crick base pairing to form a nano-sized object made only of DNA. Other advantages of DNA, such as biocompatibility, the stiffness of double strands, the versatility of chemical modification and well developed preparation methods make it an ideal material for structural nanotechnology.

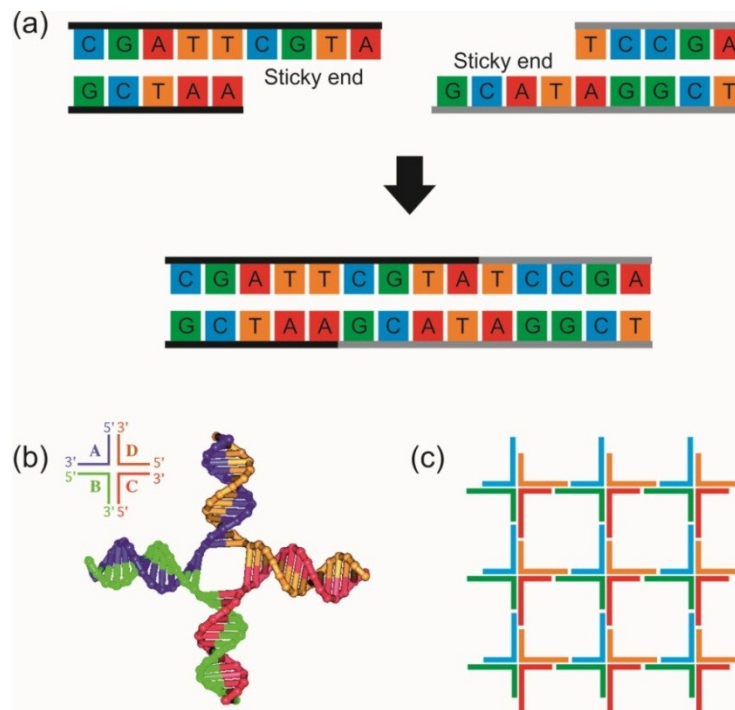


Figure 2.14 (a) One dimensional sticky-end mediated binding of two DNA double helices. (b) Molecular geometry of a Holliday junction and its schematic representation in the inset image. (c) A schematic sketch of two dimensional DNA tiles made of four-arm branched immobile Holliday junctions. ((b) adapted from [94]).

The simplest approach to connect each DNA building block together to form the desired structure is to use a ‘*sticky-end*’ on each DNA double helix building block [95]. Figure 2.14a shows a schematic sketch of the hybridization of two DNA double helices via sticky-end hybridization. At the sticky-end, a few unpaired bases are extend from the end of the DNA double helix. If the sequence of one sticky-end is complementary to that of a counterpart DNA double helix, the two sticky-ends will be hybridized through base pairing. As a consequence, two DNA double helices are linked together and form a longer DNA double helix. Moreover, when each DNA double helix contains a sticky end at both extremities could potentially be formed a continuous one dimensional DNA double helix structure consisting only of DNA.

This sticky end scheme is not limited to one-dimension but can also be extended to higher dimensions by adapting the DNA Holliday junction. The Holliday junction is

found in the intermediate steps of the genetic recombination of DNA [96,97]. Here, two pairs of homologous sequences of double-stranded DNAs form a four-arm branched junction. Due to the symmetry of base sequences, the Holliday junction can be moved within the four-arm branched junction. However, the mobility of a Holliday junction can be limited by using four independent sequences of single-stranded DNA, where each can be partially paired with two others as shown in figure 2.14b. By employing four sticky ends in a four-armed branched immobile Holliday junction, a highly ordered two-dimensional crystal structure can be formed as illustrated in figure 2.14c [98,99].

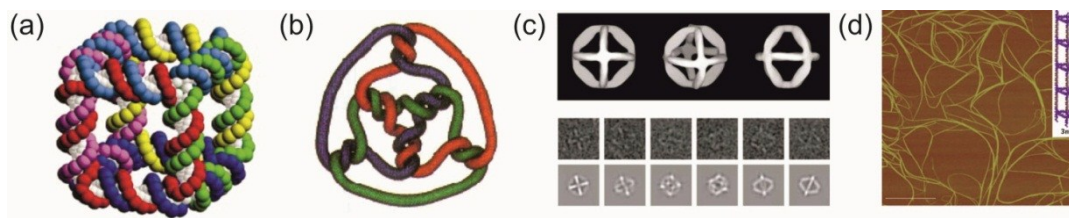


Figure 2.15 Three-dimensional DNA structure (a) DNA cube, (b) truncated octahedron, (c) octahedron made of 1.7-kilobase single-stranded DNA, and (d) DNA nanotube. (Adapted from [79,100-102])

A three dimensional DNA structure can also be realized by cross-connecting multiple single-stranded DNA in the appropriate positions to obtain a three dimensional shape. In a first man-made DNA cube, six single-stranded DNA molecules are used and each are hybridized to other four neighboring ones, thereby consisting edges of cube as shown in figure 2.15a [79,103]. Three dimensional structures of different shapes have been reported using the same strategy [101,104]. Additionally, 1.7-kilobase single-stranded DNA has been prepared based on PCR technique and further folded into an octahedron structure [102]. Three dimensional DNA structures could also be connected continuously to form structures of macroscopic length [100].

DNA origami

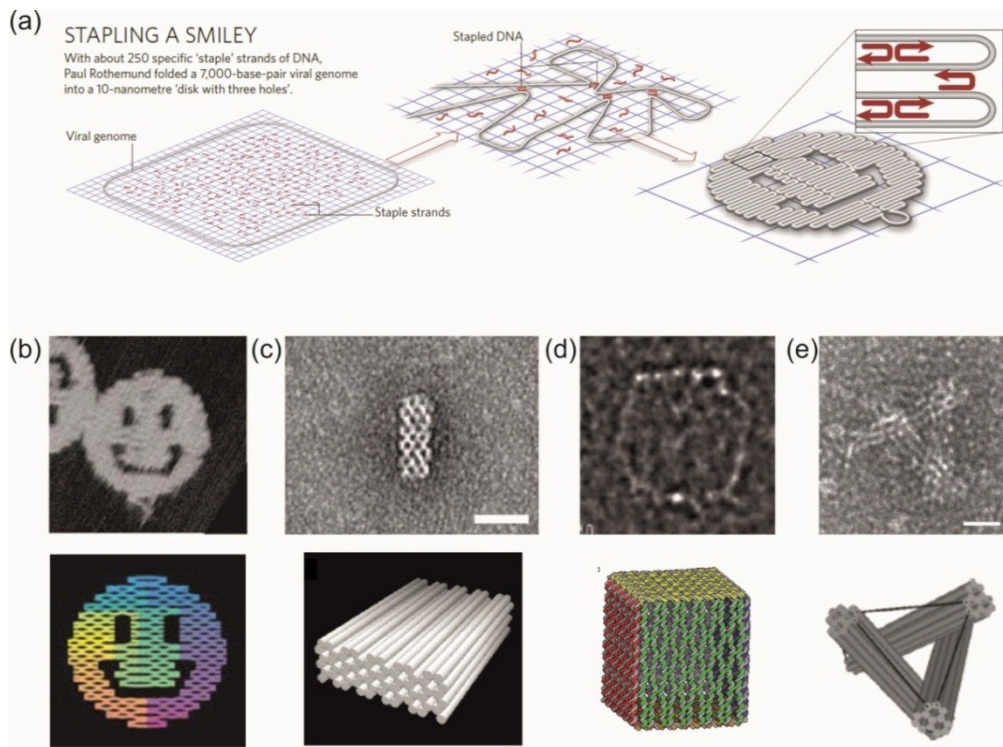


Figure 2.16 (a) Schematic illustration of the folding of the DNA origami structures. Various two or three dimensional DNA origami nanostructures: (b) smiley, (c) DNA helix-bundles, (d) DNA box and (e) tensegrity structure. (Adapted from [37,105-108])

15 years after Nadrian Seeman developed the first three dimensional DNA object by combining 6 single-stranded DNAs into a cube shaped nano-object, Paul Rothemunds suggested the ‘*DNA origami technique*,’ which makes it possible to create arbitrarily shaped DNA nanostructures more conveniently than previously suggested techniques [37]. As its name suggests, in DNA origami nanotechnology several kilobase long single-stranded DNA is folded into the pre-designed structure with the help of multiple short DNA staples as shown in figure 2.16a [108]. The versatile shape control of this method can provide nearly 100 nm sized nano-objects with spatial resolution of about 6 nm, which is the distance covered by one turn of a DNA double helix. In the very first paper by Rothemunds, he already demonstrates creation of

various two dimensional DNA origami structures, such as smileys, triangles and rectangular shapes with nearly 90 % yield from a one-pot self-assembly reaction. This revolutionary work inspired other works in structural DNA nanotechnology, and in 2009, the DNA origami technique expanded into the three-dimensional DNA origami objects. 3D hollow boxes [105], DNA helix-bundles [106], tensegrity structures [107] and recently high curvature three dimensional structures [109] have also been realized as shown in figure 2.16. These 3 dimensional DNA structures are also extended to create highly ordered crystalline structures by adopting sticky-ends in their structure [110,111]. The detailed design and preparation methods for DNA origami structures will be thoroughly discussed in following chapters.

3. Characterization, design and modeling of nanostructures

The following chapter describes principle of various methods for characterizing, designing, and modeling the properties of the nanostructures. Optical properties of nanostructures, such as Rayleigh scattering, extinction and photoluminescence are characterized by dark field microscopy, UV-Vis spectroscopy and photoluminescence spectroscopy, respectively. Also, their detailed morphology and hydrodynamic size, as well as surface charge, are determined by electron microscopies and dynamic light scattering. Computational modelings are used to calculate the effective cross-sections and the steady-state surface temperature of the metal nanoparticles. Additionally, the techniques used for designing and purifying the DNA origami nanostructures are introduced.

3.1 Optical property characterization

Dark field microscopy

Dark field microscopy (DFM) is a powerful imaging technique due to the fact that it has an exceptionally dark background and is applicable in various medium, such as air, water, oil, etc. The principle of typical dark field microscope and the resulting Rayleigh scattering image are shown in figure 3.1.

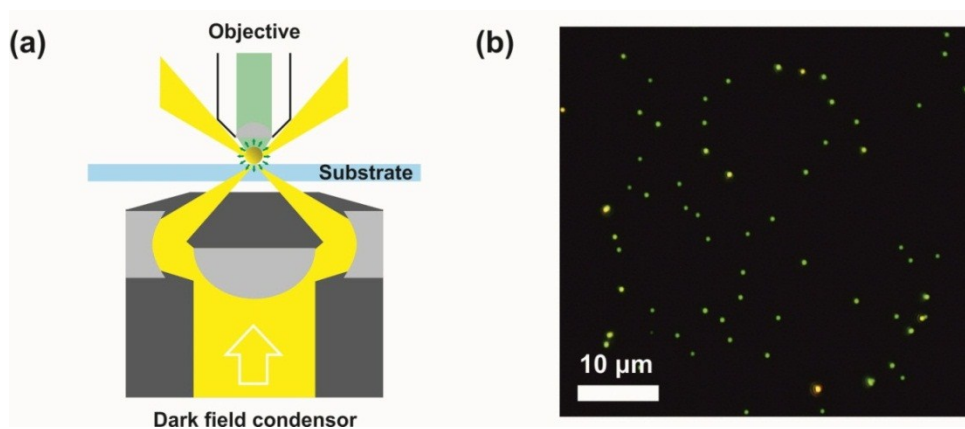


Figure 3.1 (a) Schematic illustration of conventional dark field configuration and (b) high contrast Rayleigh scattering image of 60 nm gold nanoparticles by using dark field microscope. Green and orange dots presents scattering from single nanoparticles and aggregations, respectively.

The main characteristic feature of DFM, which makes it different from conventional bright field microscopy, is the illumination pathway. Bright field microscopes use direct back illumination on the sample. Therefore, the color and contrast of images are mainly governed by absorption and transmission of the samples. However, in dark field microscopy, the light illuminating the sample is tightly focused by using a dark field condenser. When the numerical aperture (NA) of the condenser is higher than the NA of the microscope objective, only light scattered from the sample can enter the objective owing to its scattered omnidirectionality while non-scattering light is blocked. Since a dark field microscope collects scattering light selectively, it became a useful tool not only for imaging but also for characterizing scattering properties of

samples. Dark field microscopy often requires a strong illumination source due to the low intensity of the scattering light compared to bright field microscopy. Nevertheless, it is a powerful microscopic technique in the field of biology and metal nanoparticle research [59,112] where samples can be better imaged with DFM than bright field microscope. In this work, DFM is used for observing the behavior of metal nanoparticle and their scattering properties. Depending on the experimental purpose, DFM setup is modified by introducing lasers, stages, charge coupled device (CCD), and spectrometers. Details of setup modification will be discussed in each chapter accordingly. Also, ultra-clean substrates are used in DFM measurements. Since any size of chemical residue can potentially scatter the light, glass substrates are cleaned through several cleaning steps prior to use. Typically, 0.17 mm thick glass substrates (24×24 mm) are sonicated in isopropanol, acetone, 1% Hellmanex® and Millipore water sequentially for 15 min in each steps. Cleaned glass substrates are dried with nitrogen gun and kept in Silicon wafer containers to minimize further contamination.

Photoluminescence spectroscopy

Photoluminescence spectroscopy is a light-based technique that enables the luminescence of photo-excited samples to be investigated. A typical photoluminescence spectrometer consists of a excitation light source, monochromators, and a photomultiplier, as shown in figure 3.2a. Various types of lamps can be used as light sources, though, xenon lamps are widely used due to their broad wavelength range (UV-VIS) and strong illumination intensity despite their relatively low efficiency in terms of output power per input power. Once strongly illuminated broadband white light is diffracted with monochromator, only a narrow band of wavelengths is selected to illuminate the sample. When a particular transition energy level is matched with the excitation energy lever, the sample which was initially in ground state is excited with this excitation wavelength. The excited sample relaxes to the ground state by emitting stored energy in the form of a photon with a

certain energy. Part of the emission is collected via the monochromator and transferred to the photomultiplier. The signal is amplified and transformed to an electric signal. A controller reads the signal and shows there spectral data on the screen.

In this work, we use a Fluorolog®-3 Model FL3-22 (Horiba Jobin Yvon GmbH) equipped with dual-grating monochromator in both excitation and emission light paths. A 450 W xenon lamp is used for illumination, and the resulting fluorescence emission is amplified with a R928PMT photomultiplier. The setup is used to investigate distance-dependent fluorescence quenching of the organic dyes by gold nanoparticles in Chapter 5.

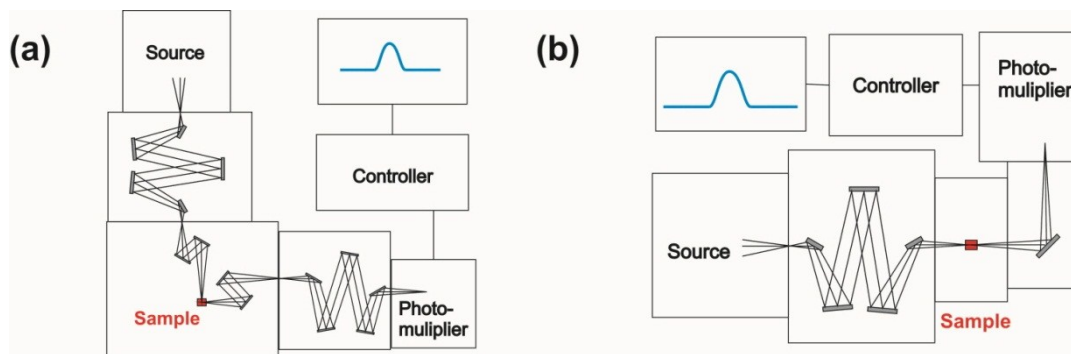


Figure 3.2 Illustration of the principle of (a) photoluminescence and (b) UV-VIS-NIR spectrometers.

UV-VIS-NIR spectroscopy

Chemical substances have their own characteristic absorption and scattering features when they interact with light. UV-VIS-NIR spectrometry is a technique providing unique extinction properties of samples with respect to the wavelength of light. A schematic sketch of an absorption spectrometer is shown in figure 3.2b. Typically, several light sources are combined and cover a wide wavelength range from UV to NIR to excite samples in solution or on a substrate. Depending on the chemical

composition and physical dimension of the sample, photons with certain energy are either absorbed or scattered by the sample. Only non-interacting photons transmitted through the sample are collected with the photomultiplier and then amplified. The detected amount of photons is plotted as a function of wavelength by the controller. The transmittance T of a sample can be converted to absorbance A by using the Beer-Lambert law [113]:

$$A = -\log T = \epsilon lc \quad (3.1)$$

where ϵ is the molar absorption coefficient ($\text{cm}^{-1}\text{M}^{-1}$) of the chemical species, l is the path length (cm) of the light passing through sample, and c is the concentration (M) of sample. However, with highly scattering samples such as metal nanoparticles, the measured absorbance is not only the consequence of absorption from the sample but also the scattering of the particles. In this case, the term ‘extinction’ is used instead of absorption.

In this study, the extinction of various metal particles functionalized with different chemicals are measured with a Cary 5000 (Varian Inc). Depending on the sample amount, different volume cuvettes are used.

3.2 Morphological and surface properties characterization

Field emission scanning electron microscopy

In micro- and nano-science, conventional optical microscopy cannot provide detailed morphological information of the objects because the physical size of samples is smaller than the diffraction limit of light used ($0.61 \times \lambda/\text{NA}$). In order to overcome this limit, electrons are used instead of photons since the wavelength of electrons is well below the one of visible light. The wavelength of electron is defined in equation (3.2),

which is the extended form of the *de Broglie relation* by taking into account relativistic effect [114]:

$$\lambda = \frac{h}{\sqrt{2m_0eU}} \frac{1}{\sqrt{1 + eU/2m_0c^2}}, \quad (3.2)$$

where h is Planck constant, m_0 is electron mass, c is speed of light, e is electron charge, and U is the electric potential, respectively. Therefore the wavelength of an electron becomes several tens of picometers with the applied electric potential used this work (around 2 kV). The diffraction limit for this wavelength is sufficiently small enough to observe the morphology of nano-size objects. A typical scanning electron microscope (SEM) consists of an electron gun, electron lens, scan coil, stigmator, and detectors. In early SEMs, the electron gun was made of tungsten or lanthanum hexaboride (LaB_6), and it liberated electrons by heating the filament to high temperatures. Therefore, the minimum threshold of their acceleration voltage was high enough to decompose organic compounds (mainly consist of H, N, O, C) while scanning. Advanced field emission scanning electron microscopy (FE-SEM) uses a cold field emission electron gun, allowing low acceleration voltages below 0.5 kV. Although lower acceleration voltage reduces the resolution of the final image, it enables imaging nano-scale organic compounds without deforming their morphology.

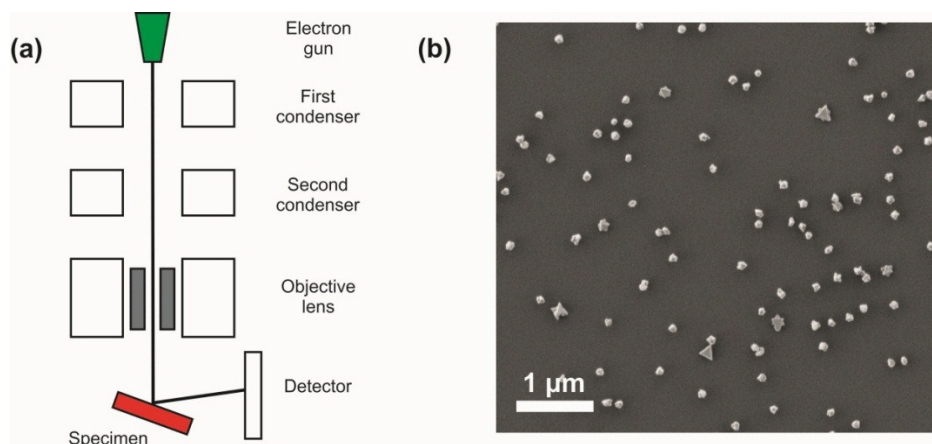


Figure 3.3 (a) Illustration of the principle of SEM and (b) resulting image of various shaped gold nanoparticles on a glass substrate.

The principle of scanning electron microscopy (SEM) is described in figure 3.3a. The principle of an SEM is similar to an optical microscope except it uses electrons instead of photons. When electrons are liberated by a field emission source, they are accelerated in a high electrical field gradient. Accelerated electrons are focused on the sample by electro-magnetic lenses and aperture. Depending on the detector in use, not only topography but also elemental composition difference within the sample can be imaged by detecting either primary or secondary scattered electrons. Sample preparation for SEM measurements can differ depending on the material properties of both the substrate and the nanostructures on it. Typically, samples are prepared on ultra clean and flat surfaces, so nanostructures can be clearly identified. If non-conducting glass substrates are used, additional conducting layers are required on the top surface to avoid accumulation of the electron charge. In this work, most of the nanostructures were deposited on either glass substrate or silicon wafers. If necessary, a thin conducting layer (~3 nm) of gold-palladium is deposited on the samples with a Leica EM SCD005 sputtering machine. All scanning electron microscope images of the various size nanostructure (few tens to several hundred nanometers) are imaged by a Zeiss FE-SEM Ultra series 55 with a secondary electron detector. Nanostructures containing organic compounds are stained by uranyl acetate prior to SEM measurement to obtain sufficiently high contrast images.

Transmission electron microscopy

Along with SEM, transmission electron microscopy (TEM) is often used to gain additional insight into the morphology of nano-scopic objects. Various imaging modes in TEM allow us to investigate not only the morphology of objects but also their chemical composition and crystallinity. All images of nanostructures in this work were taken in the typical bright/dark field image mode which shows the contrast of the sample based on its absorbance (JEM-1011, JEOL GmbH). In contrast to SEM, the specimen is placed before the objective lens which is made of electromagnetic coils along the electron beam path as shown in figure 3.4. Therefore, the primary

electrons interact first with sample and focused by the objective lens onto an imaging device. As a consequence, the TEM image of the nanostructures can be monitored in real time, whereas SEM image require a certain amount of time for scanning. However, The TEM technique is limited by its narrow choices of substrates that can be used. Typically, a fixed-sized, thin-carbon-layer-coated metal grid is used as specimen support, whereas SEM technique allows using various sizes and types of substrates.

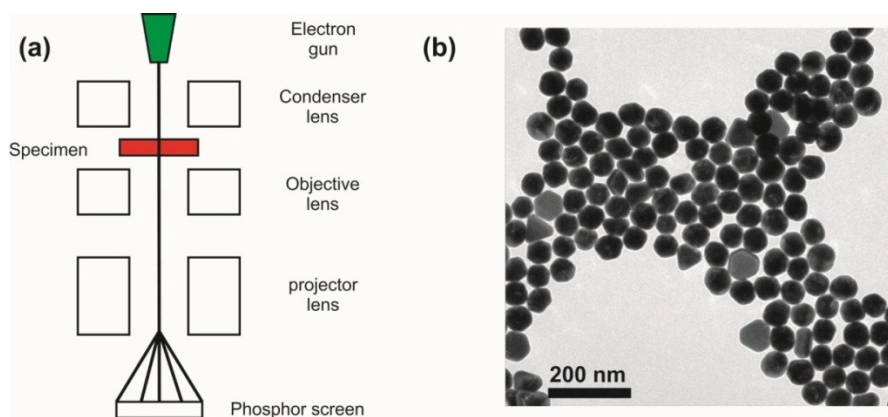


Figure 3.4 (a) Illustration of the principle of TEM and (b) resulting image of 60 nm gold nanoparticles.

Samples are prepared differently depending on the chemical composition of the materials used. As mentioned in the SEM technique, organic compounds need to be stained for better contrast. Thus, negatively-stained organic compounds can be distinguished even next to gold nanoparticles of high contrast. Formvar-carbon-coated copper grids (Science Services, FCF300-Cu) are used to prepare the sample. The following summarizes how DNA origami structures are prepared on a TEM grid as an example. First, native TEM grids were plasma cleaned under argon purge to clean and negatively charge the grid. To attach negatively charged DNA origami structures on the grids, a small drop of a 1 M magnesium chloride solution is applied to the grid, letting the magnesium chloride to go over negatively charged surface. Excess magnesium chloride solution is removed from the grid with filter paper and dried in air. Once dried, a drop of the solution with DNA origami structures is applied.

Before the droplet is completely dry, the remaining solution is removed with filter paper to avoid drying induced aggregation. A 1% uranyl acetate solution was applied for a few seconds to stain the DNA origami structure on the TEM grid. Remained staining solution is removed with filter paper and dried in air for 1 hour.

Dynamic light scattering

Dynamic light scattering (DLS) is a technique which measures the dispersity, hydrodynamic size and zeta potential of colloids. DLS is not limited to particles in colloidal solution; polymers and biological samples such as proteins and micelles can also be measured. In this work, DLS was used to measure the averaged hydrodynamic size and zeta potential of metal nanoparticles with various surface molecules such as citrate, DNA oligos, and DNA origami structures.

The principle of the DLS technique is based on the Stokes-Einstein equation which relates the diffusion of particles and their sizes in solution. When a laser hits particles in colloid, light scatters in all direction. A detector placed at a certain angle (90 degrees or close to 180 degrees) collects this scattered light pattern at time t . After time interval Δt , DLS measures the scattered light pattern again. Typically, DLS measures the scattering light pattern up to 1 to 10s milliseconds with time intervals of nanoseconds to microseconds. During each time interval, particles move from one position to the next position, thus the phase of scattered light is changed in accordance with their translational distance along the illumination direction. This changing phase interferes with other scattered light and this generates either a constructive or destructive light pattern on detector. Scattering light patterns at different times are plotted as autocorrelation curves and the decay rate (I) of this curve is calculated. Decay rate are highly dependent on particle size which are directly related to their Brownian motion in solution. Bigger size particles diffuse slower than smaller particles, therefore decay rates of bigger particles are smaller. Obtained decay rate is related to the diffusion coefficient (D) through equation (3.3) and (3.4) below, where $q = 4\pi n_0 \sin(\theta/2)/\lambda$, n_0 is refractive index of the sample and θ is the angle between the sample and the detector and λ is the laser wavelength.

From the calculated diffusion coefficient, the radius (r) of the sphere can be obtained through Stokes-Einstein equation [115,116], where T is the absolute temperature, k_B is Boltzmann's constant, and η is viscosity, respectively.

$$\Gamma = q^2 D \quad (3.3)$$

and,

$$D = \frac{k_B T}{6\pi\eta r} \quad (3.4)$$

DLS technique allows not only the hydrodynamic size to be measured but also the surface charge of colloidal nanoparticles. The zeta potential technique is a value used to determine the stability of particles in suspension. Zeta potential z can be calculated using the measured electrophoretic mobility U_E and the given dielectric constant ϵ , viscosity η , and Henry's function $f(ka)$, as shown in equation (3.5).

$$U_E = \frac{2\epsilon z f(ka)}{3\eta} \quad (3.5)$$

Electrophoretic mobility of particles can be measured with a special kit equipped with electrodes on each ends. When a potential is applied on each ends, particles attracted toward one of the electrodes have opposite charge. To measure the electrophoretic mobility, a laser is illuminated on the sample and the scattering signal is collected with detector placed 17 degrees away from the laser beam path. The scattered light intensity fluctuates with certain frequency depending on the particle velocity, and thus the electrophoretic mobility can be measured. In this thesis, hydrodynamic size and zeta potential are measured with Zetasizer Nano ZS (Malvern) equipped with He-Ne 633 nm laser.

3.3 Numerical modeling

Finite-element method

The finite element method is a numerical technique for finding approximate solutions to boundary value problems for differential equations [117]. This method uses boundary conditions to find stable solution, where the rate of change of the function becomes zero through the variational method. Thus all mathematically described small sub-domains can be connected through finite-element method, resulting in a complex equation describing a large domain. In this work, we use the heat transfer module of COMSOL Multiphysics 4.0 (FemLab) to numerically calculate the steady state heat distribution around a gold nanoparticle upon irradiation with cw laser. A constant temperature (293 K) at the surface of medium sphere is set as boundary condition which surrounds gold nanoparticle. With a sufficiently large medium sphere, the heat transfer equation can be written,

$$Q = \rho C_p \frac{\partial T}{\partial t} - \nabla k \nabla T_E \quad (3.6)$$

where ρ is the mass density, C_p is the heat capacity, and k is the thermal conductivity of the material. Laser power density per unit volume $Q = C_{\text{abs}} P V^{-1}$ (Wm^{-3}) can be calculated from the laser power density P (Wm^{-2}) and the particle volume V (m^{-3}). The material parameters of water and gold are taken from the materials library provided in the software: $\rho_{\text{water}} = 1000 \text{ kg m}^{-3}$, $C_{p,\text{water}} = 4187 \text{ J kg}^{-1} \text{ K}^{-1}$, $k_{\text{water}} = 0.54 \text{ W m}^{-1} \text{ K}^{-1}$, $\rho_{\text{gold}} = 19300 \text{ kg m}^{-3}$, $C_{p,\text{gold}} = 1290 \text{ J kg}^{-1} \text{ K}^{-1}$, $k_{\text{gold}} = 318 \text{ W m}^{-1} \text{ K}^{-1}$.

Finite-difference time-domain method

Finite-difference time-domain (FDTD) method is a numerical analysis technique used for modeling computational electrodynamics. It solves the time-dependent partial

differential form of Maxwell's equation by using finite differential approximations in discretized space. The electric field vector and magnetic field are solved alternatively at tiny time scale in each discretized space. The calculation is repeated until the system either reaches steady state or a transition state. FDTD is a powerful tool especially in the field of light-matter interaction due to its unlimiting choice of any arbitrary shape objects. To obtain accurate results, discretized space, the so called domain, has to be set small. A Yee lattice [118] is a commonly used domain for many FDTD software where the electric and magnetic vectors are placed in a rectangular unit cell, as described in figure 3.5b. The matter which interacts with the light is defined with material parameters, such as with permittivity, permeability, and conductivity values. The source, typically an electromagnetic wave, can be also set by tuning the wavelength, polarization, etc. In this work, the numerical computation package FDTD (Lumerical) was used to calculate scattering, absorption, and extinction cross-sections of gold nanoparticles with various shapes. In different structures, the optimum mesh sizes are chosen based on a convergence test. The dielectric function of gold is taken from Johnson and Christy, and the refractive index of surrounding water is set to 1.33. The geometry of gold nanorods are constructed by adding a hemisphere at bothends of a gold pillar.

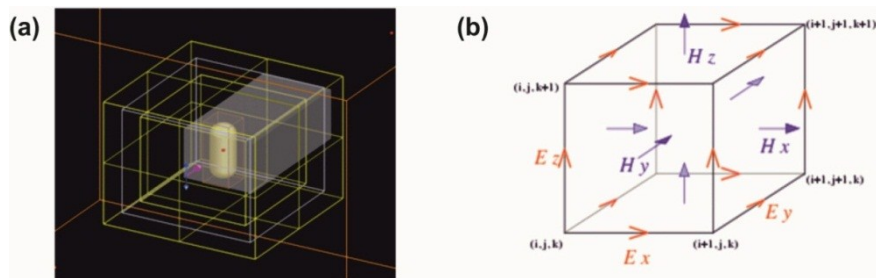


Figure 3.5 (a) Graphical interface of the FDTD modeling of gold nanorods and (b) electric and magnetic vector components in the Yee lattice.

3.4 Tool for designing and preparing of DNA origami structures

caDNAno

To design a DNA origami structure, the open source architecture program caDNAno was used. CADnano was initially developed at William Shih's laboratory under the MIT license [119]. It is specifically optimized for designing DNA origami structures where long, single-stranded scaffold DNA is folded into numbers of DNA double helix bundles, which are inter-connected together by help of short DNA staples.

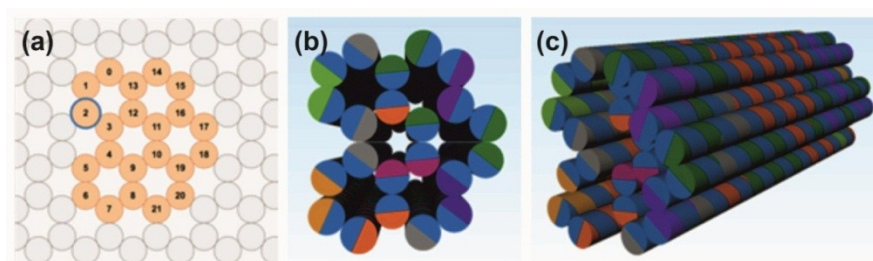


Figure 3.6 Designed DNA helix-bundles structure by caDNAno program. (a) Honeycomb alignment of DNA helix-bundles and its (b) front (d) front-side view from 3D rendered DNA origami structure. Scaffold DNA colored with blue and DNA staples are colored with other colors.

As a first step of DNA origami design, imaginary DNA helices are stacked to form square or honeycomb lattice in a 2D graphical interface based on the front (cross-section) picture of the desired structure, as shown in figure 3.6a. The diameter of each DNA helix has approximately 2-3 nm [120], thus overall diameter of DNA helix-bundles can be predicted. Once helices are arranged, the number of bases in each helices are assigned in order to obtain the desired length of the final structure. The length of each DNA helix is defined as $l = N_{bp} \times 0.34$ nm, where N_{bp} is the number of base pairs in a DNA helix. In figure 3.6b and c, the perspective view of resulting protruding DNA helix-bundles is shown. At this point, it is necessary to consider the dimensional limitation of the structure given by total number of bases in single

scaffold DNA. The total number of bases in the designed structure must not exceed the number of bases in the scaffold DNA which will be used in actual folding. On the predefined helix arrangements and lengths, multiple DNA staples are automatically added followed by choosing the type of scaffold DNA. Each DNA staple has specific base sequences assigned to be the complementary sequence to the specific part of scaffold DNA. The DNA staples hybridized with scaffold DNA and form multiple antiparallel cross-overs which results in inter-connection of all helices into a desired DNA helix-bundles structures consisting only of DNA. It is noteworthy that the number of bases in single staple DNA is kept below 60 due to the manufacturing cost. Also, staple DNA shorter than 16 bases are not recommended owing to low binding energy. The internal distortional stress of DNA origami can be occurred, which originates from the fractional number of bases per one helix turn (10.5 bases per 1 turn). To avoid undesired winding of DNA origami structure, one in every 32 bases in the scaffold is left un-bind (no complementary base assigned). The three dimensional visualization of designed DNA origami structures can be realized by implementing the caDNAno program into the 3D rendering program Maya (Autodesk) as a plug-in.

Gel electrophoresis

Gel electrophoresis is a sorting technique to separate molecules of similar charge and size. This technique is frequently used in biological research, especially to separate specific lengths and sizes of DNA, RNA and proteins. Typical gel electrophoresis consist of a container, electrodes, gel matrix and an electric potential applier, as described in figure 3.7a. The container is equipped with two linear long electrodes in each end, and the electrolyte solution is filled in between the two electrodes. The gel matrix is prepared in a separate container by mixing agarose and the electrolyte solution in a proper ratio. Depending on the agarose contents in the electrolyte solution, the matrix pore size can be tuned. The pockets with proper sized and depth are introduced into the gel matrix for the further addition of the mixture of the

material that needs separated. Once the gel matrix is prepared, it is placed into the electrolyte solution in container so that the electrolyte travel through the gel matrix. Usually the DNA ladder is also loaded into one of the pockets thus providing molecular weight information of the bands which appear during the gel electrophoresis. By applying the potential, negatively charged macromolecules will immigrate toward the cathode and the positively charged ones to the anode, as shown in figure 3.7b. Highly charged macromolecules migrate faster to the oppositely charged electrode than the less charged ones with same molecular weight. Furthermore, smaller ones travel easier through the gel matrix pores than bigger ones, and thus they migrate faster. Once similar size and charged molecules immigrate and appear as clear bands on the gel matrix, these bands are cut based on the molecular weight indicated by DNA ladders. The cut band is meshed and filtered to extract the macromolecules from the gel matrix. In this work, DNA origami of several mega Dalton molecular weight is separated from excess staple DNA or unbounded small gold nanoparticles by using gel electrophoresis.

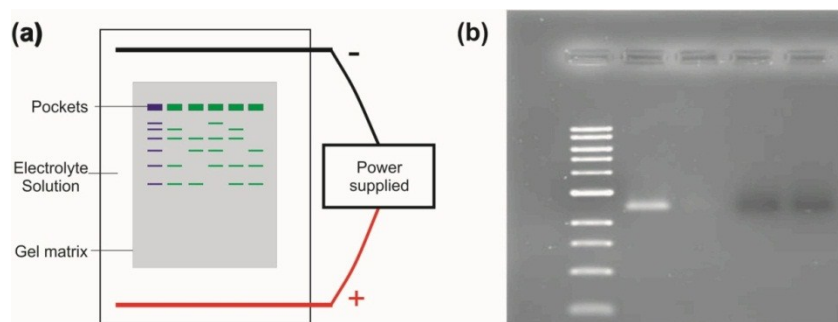


Figure 3.7. Schematic illustration of (a) gel electrophoresis and (b) fluorescence image of ethidium bromide stained gel matrix illuminated with UV lamp.

4. Optical printing of single gold nanoparticles with a focused laser beam

In this chapter an all-optical *top-down* lithography method are realized by using a tightly focused laser beam for printing single gold nanoparticle on a substrate. In the first part of this chapter, we introduce and demonstrate a ‘two-color laser printing’ technique for optically printing individual gold nanorods with control over their location and angular orientation on a substrate. The effect of laser power and relative laser polarization alignment of two lasers on angular printing precision will be discussed. In the second part of this chapter, we demonstrate optical printing of spherical gold nanoparticles onto silicon nitride (Si_xN_y) photonic crystal nanocavities. The interaction between the fundamental mode of the Si_xN_y nanocavity and the plasmon mode of the gold nanoparticles in this assembled structure will be discussed.

4.1 Two-color laser printing of single gold nanorods with control over their spatial location and angular orientation

4.1.1 Motivation for a top-down optical printing technique for depositing non-spherical gold nanoparticles

Recent advances in colloidal chemistry allow for preparation of mono-dispersed gold nanoparticles of various size, shape, and composition [121,122]. Among them, shape control enables precise tuning of the optical and electronic properties of gold nanoparticles [123,124]. Their anisotropic properties are extensively studied, especially in elongated shape [125], multiple branched [126] and star shaped [127] structures as illustrated in figure 4.1a.

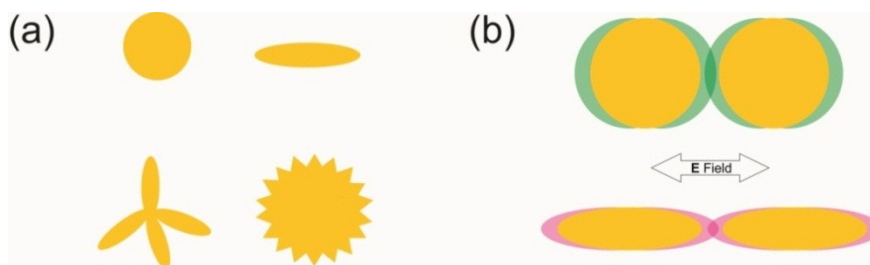


Figure 4.1 (a) Differently shaped gold nanoparticles. Gold nanosphere, -rods, -tetrapod, and -stars. (b) Localized surface plasmons (colored green and red) and electric field enhancement of closely located spherical and elongated gold nanoparticles. The arrow represents polarization direction of the external electric field.

Due to the high curvature of the tips in such structures, there is a stronger local electric field compared to the spherical structure [128]. Moreover, this local electric field can be further enhanced by placing two particles close to each other in a tip-to-tip manner as shown in figure 4.1b. An enhanced electric field which is confined between two particles allows sensing of a substance down to the single molecular

level from its' fluorescence or Raman signal [129]. However, arranging gold nanoparticles in such a configuration still remains a challenge. Electron beam lithography is generally used to create sophisticated nanostructures but the manufacturing process is relatively slow and requires expensive facilities [130]. As a contribution to this issue, in this work, an all-optical *top-down* lithography technique is used to print gold nanorods by employing two independent laser wavelength lasers. This technique, the so called *two-color laser printing*, allows printing individual gold nanorods at desired locations on a substrate with control over angular orientation.

4.1.2 Longitudinal and transverse plasmon modes of gold nanorods

Plasmonic properties of gold nanorods

As one of the approaches in *top-down* nanofabrication methods, a tightly focused cw laser has been used to print single metal nanoparticles onto a substrate [35]. In this pioneer work, a laser wavelength resonant to the plasmon mode of spherical gold nanoparticle was used to optically push an 80 nm spherical gold nanoparticle toward the surface. The maximized scattering force exerted on the spherical gold nanoparticles was enough to overcome the electrostatic repulsion between the same charged spherical gold nanoparticle and the polyelectrolyte covered substrate. Consequently, single spherical gold nanoparticles were deposited at desired locations of the surface. Optical printing of smaller spherical silver nanoparticles ($d=40$ nm) has also been achieved by different group using the same principle [36]. However, to apply this technique to anisotropic structures such as gold nanorods, their unique plasmonic properties have to be considered first.

Size (nm) (short × long)	Aspect ratio (long/short)	Transverse plasmon mode (nm)	Longitudinal plasmon mode (nm)
40 × 97	2.4	525	670
41 × 114	2.8	520	724
50 × 199	4.0	527	800
36 × 162	4.5	506	850

Table 4.1. Particle dimension, aspect ratio and peak maxima (in water) of differently sized CTAB-capped gold nanorods.

In contrast to spherical gold nanoparticles, anisotropic gold nanorods show two distinct plasmonic peaks originating from their two major collective electron oscillation modes along the long and short axis of the particle, respectively. The transverse mode (oscillation along the short axis) appears at higher energy whereas the longitudinal mode (oscillation along the long axis) appears at lower energy. Among them, the longitudinal mode is highly depend on the aspect ratio of the nanorods which is defined as a/b , where a and b are the length of long and short axes of the nanorod, respectively. In table 4.1 the particle size, aspect ratio, and plasmon resonance peak position of four differently sized CTAB-capped gold nanorods are summarized. A clear dependency of the plasmon resonance peak position on the aspect ratio can be observed: the larger the aspect ratio, the more the longitudinal plasmonic peak is shifted to longer wavelengths. This dependency in elongated nanoparticles is well described by Gans theory [131]. In this theory, absorption and scattering cross-sections of an ellipsoid are dependent on the geometrical depolarization factor L_i , where i is one of three major axes of the ellipsoid which is used as an approximation for the rods shape. The depolarization factor and the complex polarizability along the axis i can be expressed using the following equation (4.1) and (4.2), respectively:

$$L_a = \frac{abc}{2} \int_0^\infty \frac{dq}{(a^2 + q)f(q)} \quad (4.1)$$

and

$$\alpha_i = 4\pi abc \frac{\varepsilon - \varepsilon_m}{3\varepsilon_m + 3L_i(\varepsilon - \varepsilon_m)} \quad (4.2)$$

where a , b , and c are half the length of the ellipsoid along the three major axes, and $f(q) = \{(q + a^2)(q + b^2)(q + c^2)\}^{1/2}$. As a consequence of this physical geometry dependency on complex polarizability, gold nanorods interact differently with external light of different polarization.

As discussed in Chapter 2, gold nanoparticles can be optically manipulated by focused lasers depending on whether the laser wavelength is resonant with the plasmon resonance wavelength of the gold nanoparticle or not. Optical trapping is possible if the laser wavelength is far away from the plasmon resonance wavelength (i.e. off-resonant case) by maximizing the gradient force while the scattering force is minimized. On the other hand, the gold nanoparticle is repelled from the laser focus when the laser wavelength is close to the plasmon resonance wavelength of the gold nanoparticle (i.e. resonant case). Therefore, by tuning the wavelength of the laser, the behavior of gold nanoparticles at the laser focus can be controlled. This tuning is rather simple in case of a spherical gold nanoparticle since it has only one plasmon mode. However, in the case of gold nanorods, control of exerting forces is a more complex problem due to the two plasmon modes as discussed above. Thus, the spatial orientation of gold nanorods in a laser focus must always to be taken into account since the dipolar external field will interact differently with polarizabilities in each major axis of gold nanorods. On the other hand, the dual polarizability of gold nanorods provides a higher degree of freedom in the optical manipulation of gold nanorods, such as rotational motion [132], which cannot be realized with symmetrically shaped nanoparticles.

Two independent laser wavelengths

In order to fully utilize the anisotropic properties of gold nanorods, we use two different wavelength lasers for optical trapping, aligning, and ultimately printing the

gold nanorods. Theoretically, gold nanorods can be optically printed with a single wavelength laser when its wavelength is resonant with the plasmon mode of the gold nanorods. However, since the single beam printing process is extremely fast and involves plasmonic heating of the particles, it leads to poor precision in angular orientation and inaccurate printing position [133]. To overcome this problem, we introduce optical trapping as one of the sequential steps of the printing process. The additional optical trapping step provides a defined spatial location of the gold nanorods at the laser focus and thus printing accuracy can be improved. Moreover, the particles will also be aligned along their preferential orientation. The details of angular orientation of gold nanorods in the optical trap will be discussed thoroughly below.

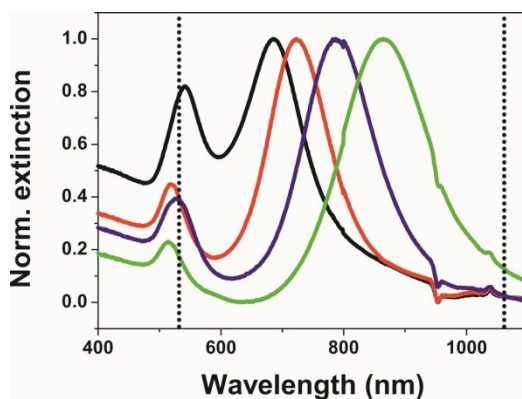


Figure 4.2 Measured extinction spectra of differently sized CTAB stabilized gold nanorods in water. 532 and 1064 nm wavelength are marked with dotted lines. 40×97, 41×114, 50×199, and 36×162 nm gold nanorods are plotted with black, red, blue, and green solid lines, respectively.

To choose appropriate wavelengths for the two lasers, we need to consider the plasmon resonance peak positions of different aspect ratio gold nanorods as shown in figure 4.2. To optically trap those nanorods, the trapping laser wavelength has to be chosen to not overlap with any of their plasmon modes. Therefore we chose a 1064 nm laser which has almost negligible overlap with both the transverse and longitudinal plasmon modes of all gold nanorods except those with the largest aspect ratio. For optical printing, the manipulation laser wavelength needs to overlap with at least one of the plasmon modes; either the longitudinal or transverse. To choose one

universal wavelength which allows printing of all gold nanorods regardless of their aspect ratios, it is necessary to consider the sensitivity of the plasmonic peaks to the aspect ratio. It can be clearly seen in table 4.1 and figure 4.2 that the longitudinal mode shifts dramatically (180 nm) with changing aspect ratio of the gold nanorods while only a small shift (21 nm) is observed for the transverse mode. Therefore, a 532 nm laser wavelength which overlaps with the transverse mode of all gold nanorods is chosen for laser printing in this study.

4.1.3 Two-color laser printing setup and PEGylation of gold nanorods

Two-color laser printing setup

To realize individual gold nanorod printing with control over angular orientation and location, we modified a conventional DFM setup. In figure 4.3. the two-color laser printing setup is sketched.

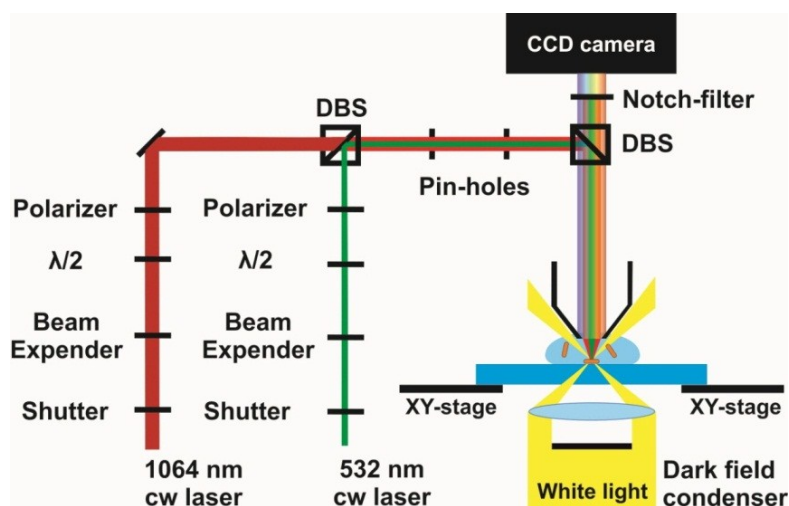


Figure 4.3. Schematic illustration of the two-color laser printing setup. 532 nm printing laser (colored green) and 1064 nm trapping laser (colored red) are implemented into a dark field microscope setup. (Adapted from [134])

Two lasers of different wavelength are coupled into the conventional dark field microscope with dichroic mirrors, which reflect 532 nm but transmit 1064 nm light. The laser beam is aligned through two pin holes and finally focused to a spot on the sample via the microscope objective. Each laser beam is controlled via a mechanical shutter, a beam expander, the $\lambda/2$ plate and a linear polarizer. The electrically controllable mechanical shutters are placed in front of each laser beam out-port to switch them on and off independently. The diameters of the laser beams are expanded to fill the back aperture of the objective. $\lambda/2$ plate and linear polarizer are used to change and refine the polarization of the laser beam. During experiments, the scattering signal of the samples is collected through the same objective and guided to either the ocular lens or CCD camera in real time. To use two different wavelengths in the visible and near-infrared regions with minimized chromatic aberration, we use a W Plan-Apochromat 63 \times water dipping objective with high numerical aperture (NA = 1.0). A dual line notch filter (532/1064) is placed before the ocular lens and CCD camera to avoid direct illumination of the eyes or the CCD. Glass substrates are fixed on a nano-precision x-y stage and thus can be moved arbitrary distances controlled by the computer program.

PEGylation on gold nanorods

To perform two-color laser printing technique with the above described setup, we functionalized CTAB-gold nanorods (Nanopartz) with thiol-terminated poly ethylene glycol (thiol-PEG). In the early work of laser printing of single gold nanoparticles by Urban et al [35], the same charge of both gold nanoparticles and the surface was used to avoid non-specific binding between them. Positively charged hexadecyl-trimethyl-ammonium bromide (CTAB) bilayers and Polydiallyldimethylammonium chloride (PDDA) are used to provide positive charges on spherical gold nanoparticles and glass substrates, respectively. However, to keep CTAB functionalized gold nanoparticles stable in colloidal solution, the concentration of CTAB has to be kept near the critical micelle concentration of CTAB (0.9 mM). At room temperature, and

at the critical micelle concentration, CTAB forms small micelles or crystals in solution, which can potentially disturb optical trapping. Thus, it often requires an extra heating chamber (~ 30 °C) to avoid crystallization [135]. Citrates are also used as an alternative stabilizer instead of CTAB [136]. Owing to their negative charge, the use of PDDA on the substrate surface can be avoided. However, in contrast to spherical gold nanoparticles, gold nanorods cannot be stabilized with small stabilizing molecules such as citrate due to their relatively small steric effect compared to the large attraction force among gold nanorods [137].

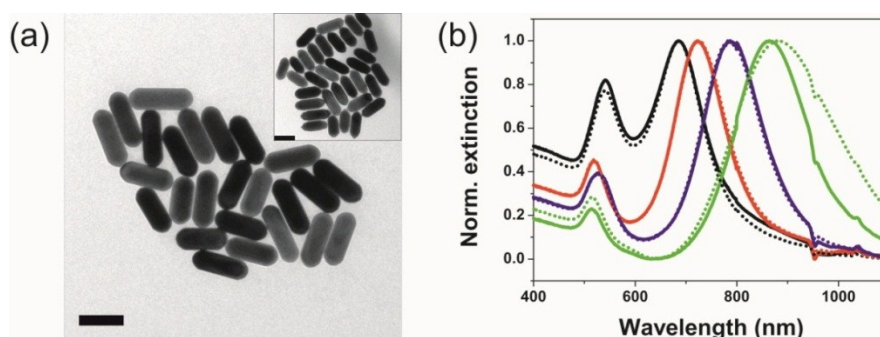


Figure 4.4 (a) TEM images and (b) extinction spectrum of differently sized gold nanorods before and after (inset) PEGylation. 40×97, 41×114, 50×199, and 36×162 nm gold nanorods are plotted with black, red, blue, and green solid lines, respectively. Scale bar is 100 nm.

To overcome this drawback, PEG was used in this work to substitute the role of CTAB as a stabilizer. By adding water soluble thiol-PEG into CTAB stabilized gold nanorod colloid solution, CTAB was efficiently replaced, with the thiol-PEG and chemically grafted onto the gold nanorods surface via covalent thiol bonding. PEGylated gold nanorods have several advantages. First, they are stable in aqueous solution without additives, while CTAB and citrate require a certain concentration of the stabilizer in solution for colloidal stability. Second, an additional chemical treatment of the substrate is not necessary. Since PEG has neutral charge, non-specific binding between PEGylated gold nanorods and the non-functionalized substrate can be avoided. Preparation of PEGylated gold nanorods is summarized as follows; 50 μ L of PEG solution (10 mM, Mw= 5,000 Da) are added to 500 μ L of CTAB capped gold nanorod solution (33 pM, < 10 mM CTAB). The mixture is

incubated at room temperature overnight. Ligand exchanged gold nanorods are centrifuged at 1200 rpm for 15 min. The supernatant containing excess PEG and CTAB is removed with a pipette and the remaining gold nanorod pellet is redispersed in Mili-Q water. This process is repeated three times.

In figure 4.4 SEM images and extinction spectra of different sized gold nanorods from before and after ligand exchange are shown. No distinct peak shift or broadening is observed in most samples. Only the 36/162 aspect ratio gold nanorods show an 20 nm red shift of their longitudinal peak and also significant broadening of the plasmonic band. This indicates that gold nanorods partially aggregate during the ligand exchange. In nano-sized colloids, it is generally accepted that gold nanorods with larger aspect ratios tend to aggregate more easily than smaller ones due to the larger area of flat surface on their sides.



Figure 4.5 Dark field microscope image of optically printed gold nanorods (41×114 nm) with two-color laser printing setup.

Figure 4.5 shows a scattering image of three 10×10 square patterns each consisting of optically printed gold nanorods (41×114 nm) on a non-functionalized surface by using two-color laser printing technique. Individual PEGylated gold nanorods can be clearly identified as orange scattering dots. It is noteworthy that no single gold nanorods which attached non-specifically onto the surface of the glass substrate can be found, while optically printed particles are firmly fixed in the desired locations over a large area. This indicates that PEGylation provides good colloidal stability for the gold nanorods and thus they stay stable in pure aqueous media, while non-specific binding between gold nanorods and substrate can also be avoided.

4.1.4 Sequential two-color laser printing process: trapping, aligning and printing

Three-step two-color laser printing process

In figure 4.6 the three-step laser printing process assisted by two different color lasers is shown as a schematic illustration. To summarize the three steps, in the first step, a randomly diffusing gold nanorod in solution is optically trapped at the focus of the off-resonant trapping laser slightly above surface. Second, the trapped gold nanorod aligns along the polarization direction of the trapping laser in the optical trap. Finally, the trapped and aligned gold nanorod is printed onto the surface by addition of the printing laser, for which the polarization is perpendicularly aligned to that of the trapping laser.



Figure 4.6 Schematic illustration of three-step two-color laser printing of single gold nanorod. Trapping: freely diffusing gold nanorod is optically trapped into the trapping laser focus. Aligning: trapped gold nanorod is aligned along polarization of the trapping laser. Printing: gold nanorod is optically printed by addition of printing laser. (Adapted from [134])

When the 1064 nm trapping laser is focused onto the substrate at a defined location, a freely diffusing gold nanorod near this laser focus will be pulled due to the attractive gradient force. The optically trapped rod is then guided to the spot where the laser intensity is highest. Strictly speaking, the actual particle position in the optical trap is not exactly at the center of the laser focus but rather downwards along the laser propagation direction due to the presence of a non-negligible scattering force acting on the gold nanoparticle. Therefore, a gold nanorod optically trapped above a surface

is rather gently pushed down toward the surface but not deposited on the surface due to the PEG polymer cushion around it (steric effect).

In the optical trap, elongated gold nanorods are aligned *orthogonal* to the laser beam propagation direction, and *parallel* to the laser polarization direction. The orthogonal alignment of metal nanorods in the optical trap with respect to the laser propagation axis has been reported previously [132,138]. If the size (length of longest axis) of the trapped nanorod is bigger than the laser beam waist, it aligns along the laser beam propagation axis. In contrast to bigger particles, particles smaller than the beam waist will align perpendicular to the laser beam propagation direction [139]. All gold nanorods used in this work are smaller (< 200 nm) than the beam waist of the trapping laser which has a FWHM of ~ 1 μm . Thus, gold nanorods are aligned orthogonally to the laser propagation direction in the optical trap.

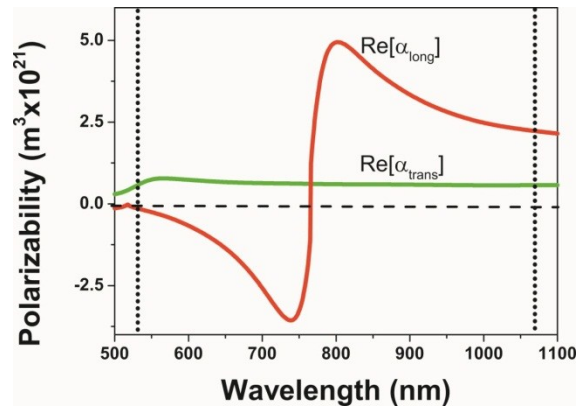


Figure 4.7 Calculated real part of the polarizability of 41×114nm gold nanorods at the longitudinal and transversal mode respectively. 532 and 1064 nm wavelength are marked with dotted lines.

The parallel alignment of gold nanorods with respect to the laser polarization direction can be explained by comparing the potential energy with respect to different axes of the gold nanorod under an external electric field. The potential energy at a specific axis is $U = -\langle P \cdot E \rangle = -1/2 \sum \text{Re}(\alpha_i) E^2$, where i indicates the long or short axis of the gold nanorod, $\text{Re}(\alpha_i)$ is the real part of the polarizability of the gold nanorod along the i axis and E is the incident electric field. In figure 4.7, the real part of the polarizability of the gold nanorods along both the long and short axes are

plotted. At the trapping laser wavelength of 1064 nm, the real part of the polarizability of the longer axis is bigger than that of the short axis. Consequently, to minimize the potential energy, gold nanorods preferentially align along the polarization direction of the laser with respect to its long axis. In such alignment, the alignment stiffness factor is described by $\text{Re}(\alpha_{\parallel})/\text{Re}(\alpha_{\perp})$, where $\text{Re}(\alpha_{\parallel})$ and $\text{Re}(\alpha_{\perp})$ are the polarizabilities of the axes of the gold nanorod which are parallel or perpendicular to the polarization direction of the laser, respectively. Therefore, when the gold nanorods are optically trapped with off-resonant laser, nanorods with higher aspect ratio have higher alignment stiffness than smaller aspect ratio particles, which results in more precise angular orientation in the optical trap.

In the final step of the two-color printing process, optically trapped and aligned gold nanorods are exposed to a resonant 532 nm printing laser. At this point, it is necessary to consider the two possible alignments between the transverse plasmon mode of the gold nanorods and the polarization direction of the printing laser. It can be clearly seen in figure 4.7 that at 532 nm the magnitude of the real part of the polarizability of the long and short axes is reversed compared to at 1064 nm. If the polarization of the printing laser is aligned along the long axis of the gold nanorod, the alignment stiffness factor $\text{Re}(\alpha_{\parallel})/\text{Re}(\alpha_{\perp})$ will be below 1. This indicates that parallel alignment of the printing laser polarization with respect to the long axis is energetically unfavorable. To be energetically favorable, the printing laser polarization needs to be turned 90 degrees and be parallel to the short axis of the gold nanorod. In this alignment, the stiffness factor will be bigger than 1 which indicates an energetically favorable orientation of the gold nanorod with respect to the polarization of the printing laser.

Two-color laser printing of individual gold nanorods

To achieve the best angular alignment of gold nanorod by two lasers in the optical trap, the polarizations of the trapping and printing lasers should align parallel and

perpendicular to the long axis of gold nanorod, respectively, as discussed above. In this alignment, the trapping laser is almost perfectly resonant with the transverse plasmon mode and thus the magnitude of the scattering force induced by the printing laser will be maximized. When the overall scattering force overcomes the overall gradient force from both lasers, the particle will be repelled from the laser focus and be printed onto surface via strong van der Waals interaction between the gold nanorod and the glass substrate. In figure 4.8 the amplitude and direction of the forces exerted on a gold nanorod near the laser focus by trapping, printing, and the combination of both lasers are plotted, where trapping and printing powers are 33 and 4.2 mW, respectively. It can be clearly seen that when the force contribution of the printing laser (2 pN) is bigger than the one of the trapping laser (1.7 pN), the overall force distribution will look similar to the distribution of the force induced by the printing laser. It is noteworthy that the printing laser not only provides additional scattering force on the gold nanorods but also increases the surface temperature. As a consequence of optical heating, the PEG layer around the gold nanorods is thermally collapsed and thus nanorods may fix onto the substrate strongly. The details about temperature increases upon printing laser irradiation will be discussed in the later part of this chapter.

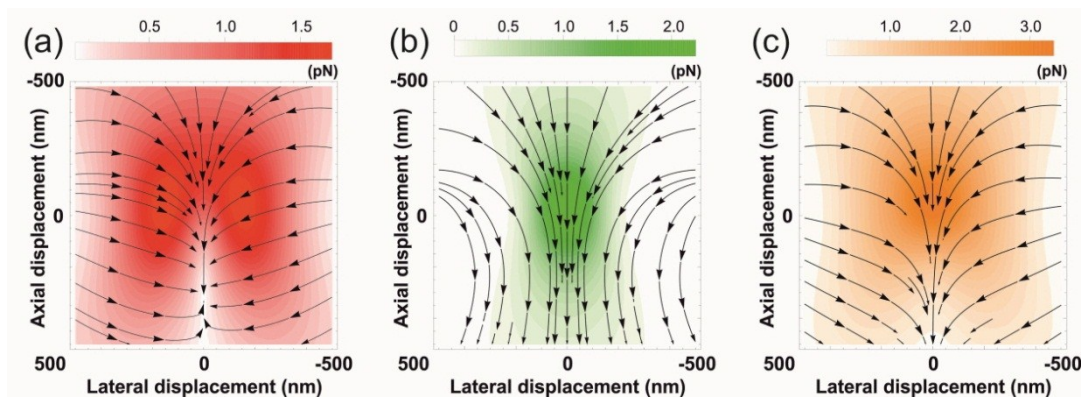


Figure 4.8 Amplitude (colored) and direction (arrow) of calculated optical forces exerting on 41×114nm gold nanorods under the (a) trapping, (b) printing, and (c) two-color lasers, respectively. Trapping and printing laser powers are 33 and 4.2 mW, respectively. Light propagates from top to bottom of the force map. (Adapted from [134])

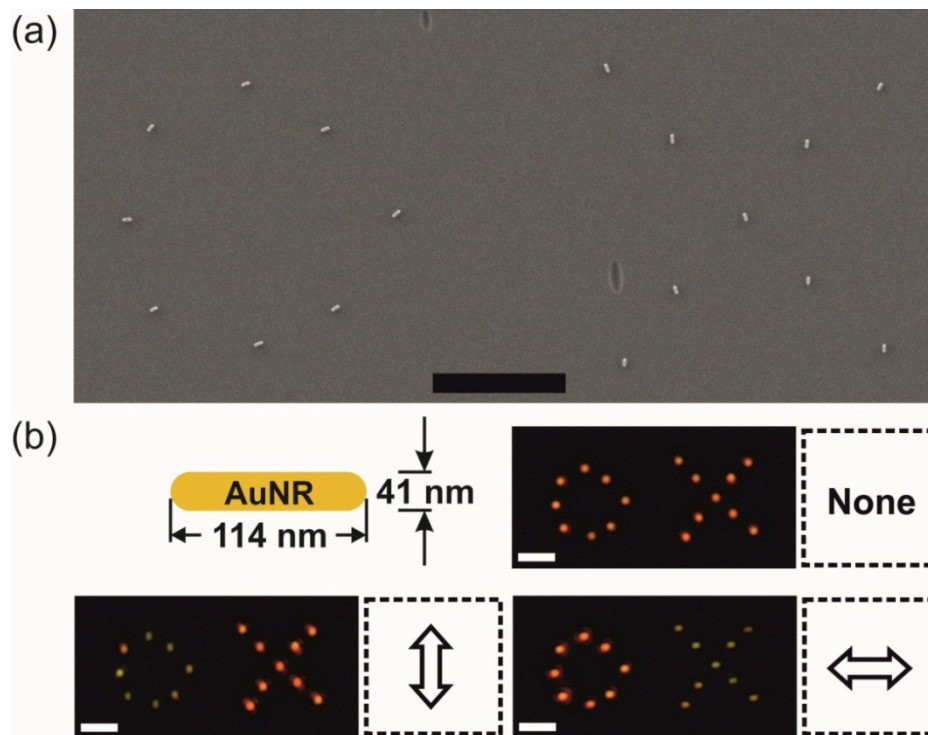


Figure 4.9 (a) SEM image of O and X patterns created by two-color laser printing. (b) Size of the gold nanorods used in this patterning experiment and the polarization dependent Rayleigh scattering images of O and X patterns. Orientations of the polarizer are represented by diagonal-arrows. Here, trapping and printing laser powers are 33 and 4.2 mW, respectively. Scale bar is 2 and 1 μm for a and b, respectively. (Adapted from [134])

Figure 4.9a shows a printed O and X pattern consisting of individually printed gold nanorods on the same substrate produced using the two-color laser printing method described above. Each gold nanorod is printed with a fixed perpendicular orientation of the polarization of the trapping and printing lasers. The pattern is created by moving the nano-stage after each single particle has been printed. After one of the letters has been printed, the laser polarizations are turned 90 degrees and the other letter is printed next to the first one. Therefore, the particles in each letter are oriented perpendicularly to each other as seen in the SEM image. The perpendicularly oriented O and X patterns can also be distinguished by using a linear polarizer in the detection path. Without a linear polarizer all printed particles should show a mixed scattering color from both transverse (520 nm) and longitudinal modes (724 nm). However,

since the intensity of the longitudinal mode is higher than that of the transverse mode, the overall color appears as red. With a linear polarizer, the two modes can be separated by aligning the polarizer with respect to the axes of the nanorods. When aligned along one of the main axes of the gold nanoparticle, the particles in one pattern show only scattering from the longitudinal mode while the particles in the other pattern show scattering from the transverse mode. It can be clearly seen in figure 4.9b that by turning the polarizer 90 degrees, green scattering from the transversal mode and red scattering from the longitudinal mode are interchanged.

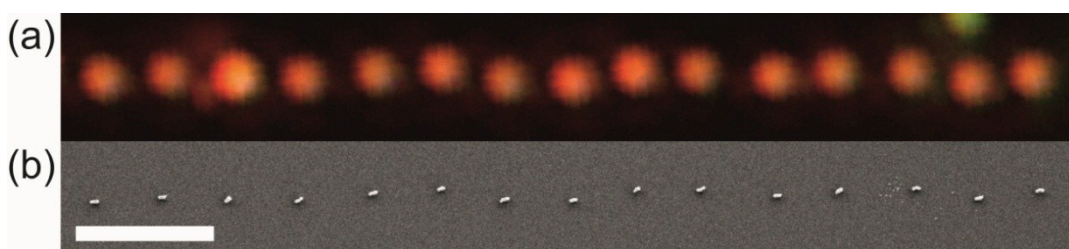


Figure 4.10 DFM and SEM image of a line of patterned 41×114nm gold nanorods used to determine the printing accuracy of two-color laser printing technique. Scale bar is 2 μm.

We also studied the printing accuracy of the two-color printing technique by printing a number of gold nanorods in a nominally straight line. Figure 4.10 shows a dark field microscope and SEM image of 15 gold nanorods printed in a line. From the SEM image the printing precision of our methods was calculated to be about 50 nm which is close to previous reports (~ 100 nm) of single nanoparticle printing with a resonant laser wavelength [35,140].

The control of the printing location and angular orientation was also possible with other gold nanorods with different sized. The applicable trapping laser power of the gold nanorods with higher aspect ratio was narrower than the one of smaller aspect ratio due to bigger absorption cross-section at 1064 nm. In following discussions, 41 × 114 nm gold nanorods are used to study the effect of the relative alignment and power of the two lasers on the angular printing precision.

4.1.5 Effect of relative orientation and laser power of two lasers on angular printing precision of gold nanorods

In the following discussions, the effects of relative alignments and laser powers of the two lasers on angular printing precision will be studied. These effects were determined by measuring the angular displacement of each printed gold nanoparticle with respect to trapping laser polarization axis in SEM images. To have statistically valid data, more than 100 gold nanorods were printed under the same conditions, where relative alignment and laser power of the two lasers are fixed. Also, one specific size of gold nanorods (41×114 nm) is chosen for quantitative comparison between sets of experiments.

Effect of relative orientation of two lasers on angular printing precision of gold nanorods

As we discussed above, perpendicular alignment of the two lasers provides the best angular printing precision in our two-color printing technique. To prove this experimentally, we chose two major relative polarization alignments of the two lasers; perpendicularly aligned and parallel alignment. For a qualitative comparison, the magnitude of the printing laser power is adjusted in each alignment in order to keep the total scattering force constant while the trapping laser power is kept constant. To adjust this value, it is necessary to take into account the magnitude of the scattering force which is governing by the imaginary part of the polarizability of gold nanorods as expressed in equation 2.25. From the calculation, the magnitude of the imaginary part of the polarizability of the short axis at 532 nm is bigger than that of the long axis by the factor of 1.35. Thus, with same printing laser, stronger scattering force will exerts on a gold nanorod if the relative polarization of lasers is perpendicularly aligned than when parallel aligned. To reflect this difference, an 11.2 mW printing laser power is used for parallel alignment, while 8.3 mW is used for perpendicular alignment.

In figure 4.11 the frequency distributions of angular deviation of the printed gold nanorods are shown for both perpendicular and parallel cases. It is clearly seen that perpendicular alignment of the two laser polarization directions gives a more than 2 times smaller standard deviation of the angular printing precision than for parallel alignment.

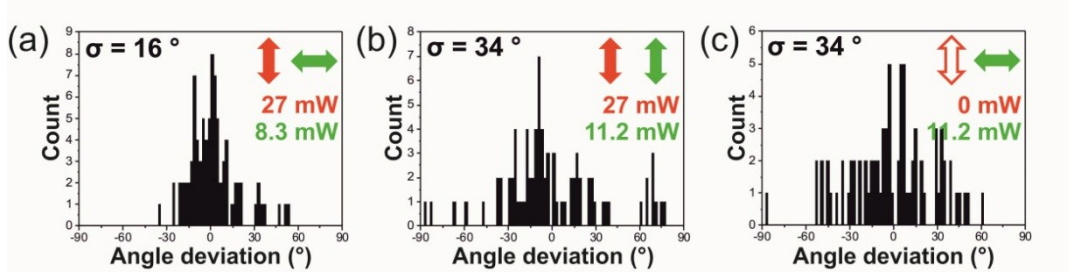


Figure 4.11 Frequency distributions of angular deviation of printed 41×114nm gold nanorods from their nominal orientation in different relative polarization alignments between the two lasers. (a) perpendicularly alignment (b) parallel alignment (c) printing laser only. The power used for each laser is colored with its polarization orientation accordingly. Standard deviations σ of each set of experiments are shown as insets. (Adapted from [134])

This difference can be explained by the angular torque induced by the external applied field. In both parallel and perpendicular alignments of two lasers, gold nanorods are aligned along the polarization of the trapping in the second step of two-color printing process which resulting in no angular torque on the gold nanorods. However, when the printing laser polarization is oriented with an angle θ ($0 \leq \theta \leq \pi/2$) with respect to the short axis of the gold nanorod in the optical trap, there will be an angular torque on this gold nanorod which can be expressed as $\tau = |\langle P \times E \rangle| = 1/4E_0^2(\alpha_{\text{paral}} - \alpha_{\text{perpend}}) \sin \theta$ [141], where α_{paral} and α_{perpend} are the polarizabilities of the short and long axes of the gold nanorod with respect to the printing laser polarization direction, respectively. Therefore, the angular torque on gold nanorods induced by the trapping laser is 0 when the two lasers are perpendicularly aligned ($\theta = 0$). However, when the two lasers are aligned in parallel ($\theta = \pi/2$), the torque induced by the printing laser will be maximized and its magnitude is given by $1/4E_0^2(\alpha_{\text{paral}} - \alpha_{\text{perpend}})$. Consequently, using parallel alignment of the printing laser significantly reduces the angular stiffness of the trapped gold nanorods and thus

results in decreased angular printing precision. On the other hand, a perpendicularly aligned printing laser provides additional angular stiffness to the pre-aligned trapped gold nanorods in the optical trap. This synergetic alignment effect becomes obvious by comparing two-laser printing with parallel alignment of the two lasers and single beam printing where no trapping laser is used. As shown in figure 4.11 the standard deviation (34 degrees) value of single color printing gives a similar value to the one from two-color printing with parallel alignment of the two lasers. This indicates that the torque induced by the printing laser can significantly affect the quality of the two-color laser printing depending on the polarization alignment of the two lasers. Since perpendicular alignment of the polarization directions of the two lasers brings synergetic effects for the printing accuracy, all following studies are conducted with this perpendicular alignment.

Effect of trapping laser power on angular printing precision of gold nanorods

The laser power dependence of the angular printing accuracy has also been studied. To this end, the intensity of one laser was varied while the other one was kept constant. To study the trapping power dependency of the angular printing precision, the printing laser power was fixed at 4.2 mW while the trapping laser power are set to 15, 33 and 52 mW. It is noteworthy that 4.2 mW is the minimum laser power required for two-color printing of gold nanorods trapped with a 52 mW trapping laser. Therefore, the 4.2 mW printing laser can be successfully used to print particles under lower trapping laser power conditions as well.

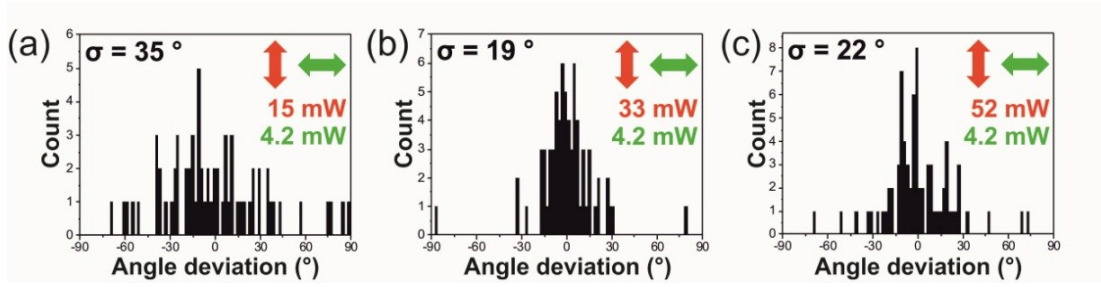


Figure 4.12 Frequency distribution of the angular deviation of the printed 41×114nm gold nanorods from their nominal orientation in different trapping laser power. The printing laser power is kept constant at 4.2 mW while trapping laser power is varied at (a) 15 mW (b) 33 mW and, (c) 52 mW, respectively Powers used for each laser are colored with their polarization orientation accordingly. Standard deviations σ of each set of experiments are shown as insets. (Adapted from [134])

In figure 4.12 the frequency of angular deviation of printed gold nanoparticles at different trapping laser power is shown. It can be clearly seen that an intermediate trapping laser power at 33 mW provides the best angular printing precision with a standard deviation of 19 degrees while lower (15 mW) and higher (52 mW) trapping laser powers result in standard deviations of 35 and 22 degrees, respectively. The most important factor which limits the angular printing precision is the rotational diffusion of gold nanorods in the optical trap due to their Brownian motion. With strong rotational diffusion the angular deviation of gold nanorods from the nominal orientation is larger, while more restricted rotational diffusion narrows the angular deviation distribution of the printed particles. As discussed early in this chapter, nanorods will align along the polarization direction of the trapping laser. The magnitude of the optical potential energy of the particle in the trap is proportional to the external electric field. Thus, with higher trapping laser the power optical potential energy will be steeper than with lower trapping laser power, resulting in better confinement of gold nanorod within the optical trap. With the minimum trapping laser power of 15 mW, the potential energy in the trap will not be enough to fix the gold nanorods along the orientation of the trapping laser polarization, thus the angular printing precision is low. Interestingly, with the highest trapping laser power of 52 mW, the standard deviation of the angular printing precision is worse as compared to

the intermediate laser trapping laser power. To interpret this observation, we need to look at the amplitude of the gradient force for different trapping laser powers.

Laser power (mW) (trapping laser / printing laser)	Force (pN)		Temperature increments (K)	
	Gradient	Scattering	Trapping laser	Printing laser
15 / 4.2	1.00	2.65	27	147
33 / 4.2	1.80	3.18	57	147
52 / 4.2	2.68	3.74	89	147
33 / 8.3	2.12	5.34	57	299
33 / 10.2	2.29	6.34	57	373

Table 4.2 Calculated gradient and scattering forces as well as temperature increases on the surface of 41×114nm gold nanorods at a given laser power.

In table 4.2 the amplitude of the gradient and scattering forces are shown for different trapping and printing laser powers. With fixed printing laser power at 4.2 mW, by increasing the trapping laser power from 15 to 52 mW the ratio between gradient and scattering forces comes closer to 1. This relative force intensity difference affects the time required for gold nanorods to escape from the laser focus and be printed to the substrate. With the highest trapping laser power at 52 mW, the gold nanorod will be strongly trapped by the gradient force and thus is propelled less rapidly when the printing laser is added. Therefore, the gold nanorod will have more time to change its orientation on the way from the laser focus to the substrate. As a consequence, the angular printing precision is slightly reduced when the scattering force from the printing laser becomes closer to the gradient force exerted by the trapping laser. Therefore, we conclude that there is an optimal intermediate trapping laser power which gives the best angular printing precision for this method via balancing between two competing effects of the angular trapping stiffness and the particle acceleration.

Effect of printing laser power on the angular printing precision

We now turn to the printing power dependency of the angular printing precision. In contrast to the above experiments, we now fix the trapping laser power at 33 mW, and vary the printing laser intensity to 4.2, 8.3 and 10.2 mW. The distribution of the angular deviations at different printing laser intensities are plotted in figure 4.13. The standard deviation value of the distribution is smallest (i.e. 19 degrees) at a printing laser power of 4.2 mW. Higher printing laser powers of 8.3 and 10.2 mW result in standard deviations of 27 and 25 degrees, respectively.

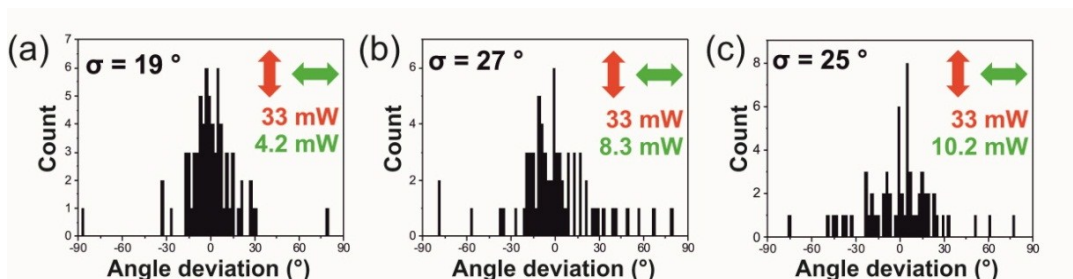


Figure 4.13 Frequency distribution of the angular deviation of the printed 41×114nm gold nanorods from their nominal orientation in different printing laser powers. The trapping laser power is kept constant at 33 mW while printing laser power is varied at (a) 4.2 mW (b) 8.3 mW and, (c) 10.2 mW, respectively. Powers used for each laser are colored with their polarization orientation accordingly. Standard deviations σ of each set of experiments are shown as insets. (Adapted from [134] ref)

That the best angular precision is achieved at the lowest printing power can be explained by the temperature increase of the nanorod upon irradiation with the printing laser. The temperature increase of the gold nanorod has two major impacts on the dynamics of the optical printing process, via rotational diffusion and printing time. The rotational diffusion of gold nanorods is increased in linear proportion to the temperature increase induced by plasmonic heating of the two lasers. In this study, the same trapping laser power is used throughout these experiments, thus the contribution of the trapping laser to the temperature increase of the nanorods is the same in all three cases. This increase is 57 K. Since the plasmonic heating linearly increases with laser power, with printing powers of 4.2, 8.3 and 10.2 mW the overall

temperature increases of the gold nanorods are 204, 356, and 430 K, respectively. Therefore, angular printing precision of gold nanorods is decreased with laser power by a factor of P . In contrast to rotational diffusion, the printing time is reduced with printing laser power by a factor of $P^{-1/2}$, which results in an increase in the angular printing precision of gold nanorods. Higher printing laser power leads to a stronger scattering force, resulting in greater acceleration of the gold nanorod toward the substrate. Consequently, the particle travels the same distance within a shorter time, resulting in an increase in angular printing precision. Assuming a constant printing laser power, among these two competing dynamics, the dominant one is rotational diffusion. Therefore, the best angular printing precision is achieved at the lowest printing laser power of 4.2 mW.

4.1.6 Summary

In this chapter, gold nanorods were printed onto non-functionalized substrates with control over their angular orientation and location by using two-color laser printing methods. In this method, gold nanorods were all-optically printed via three step process by employing two independent laser wavelengths. A 1064 nm laser whose wavelength is off-resonant with both the transverse and the longitudinal plasmon modes of the gold nanorods was used to trap and align the gold nanorods simultaneously. A 532 nm laser whose wavelength is resonant with the trasverse plasmon mode was then used to print pre-aligned gold nanorods onto a substrate. Gold nanorods were functionalized with PEG oligos and thus allows printing gold nanorods without using any further chemical substance in colloidal solution or on the surface. The effect of relative laser polarization alignment and laser powers of two lasers on the angular printing precision of the gold nanorods were experimentally studied. With optimized conditions, where the two lasers are perpendicularly aligned and with their powers of 27 and 8.3 mW for trapping and printing laser respectively, we achieved excellent control of angular orientation (± 16 degree) and spatial location ($\sigma = 50$ nm) of the gold nanorods printed on a flat surface.

4.2 Laser printing of spherical gold nanoparticles onto a silicon nitride photonic crystal nanocavity

4.2.1 Motivation for a top-down laser printing technique for creating a photonic crystal nanocavity containing a gold nanoparticle

In the growing field of photonic crystal nanocavities (PCNs), confining light in a physical defect is commonly realized by introducing periodic air holes (low refractive index) into a material with a high refractive index [142]. At this physical defect, light with a certain wavelength can be confined by the periodic modulation of refractive index and eventually directed to controlled emission from the structure. Since these materials provide a highly spatially confined electromagnetic field, they are useful to study light-matter interactions, especially the interaction between the optical field and sub-wavelength sized particles [143]. Quantum dots [144,145], nitrogen-vacancy diamonds [146,147] and recently plasmonic metal nanoparticles [148,149] are placed on the physical defect of the PCN and their effect on the nanocavity mode was investigated. To assemble such structures, two major nanofabrication methods are commonly used [150].

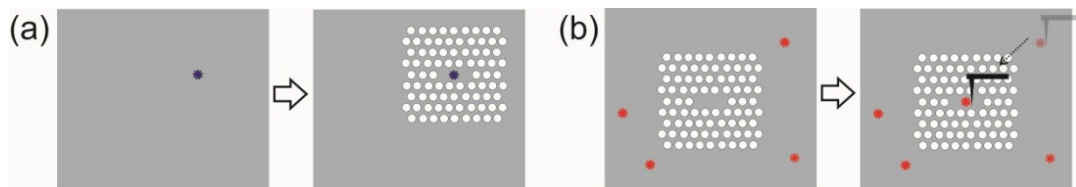


Figure 4.1 (a) Pre-positioning and (b) Post-positioning methods for nano-object arrangements on a two dimensional photonic crystal nanocavity.

In figure 4.1 pre- and post-nanofabrication methods are sketched. In the pre-nanofabrication method, the location of self-assembled nano-objects on a flat dielectric slab is firstly identified by microscopic techniques. Surrounding the pre-defined location of the nano-object, air holes are fabricated by a sequential process of electron beam lithography (EBL) and etching. In post-nanofabrication methods, in contrast to the pre-fabrication method, the air holes are firstly fabricated by EBL and an etching process. Thereafter, colloidal nano-objects are randomly deposited and further moved to the defect where the nanocavity mode is manifesting using an atomic force microscope (AFM) technique.

Both techniques yield precise positioning of a nano-object onto a PCN, however, they are rather limited in terms of production efficiency when routine fabrication is considered. To overcome this issue, a laser assisted all-optical laser printing method for single spherical nanoparticle deposition will be introduced in this chapter. This technique enables fast and convenient fabrication of a two dimensional Si_xN_y PCN containing a spherical gold nanoparticle.

4.2.2 Optical printing setup and silicon nitride photonic crystal nanocavity

In this work, L3 type two dimensional PCNs were prepared in free-standing silicon nitride (Si_xN_y) membranes with a thickness of $T = 200$ nm, lattice constant of $L = 260$ nm, and airy hole diameter of $D = 156$ nm. Although Si_xN_y has low refractive index ($n = 1.8 - 2.2$), the prepared PCN has a fairly high quality-factor ($Q = 210$) and it transmits light at a visible wavelength which is essential for dark field microscopy. Light confined at the PCN escapes from a linear three-hole defect (900×300 nm) located at the center of the air hole array. Detail of the design and an SEM image of the PCN, as well as its fundamental cavity mode, are shown in figure 4.2. In the photoluminescence spectrum of the Si_xN_y PCN, broad and narrow peaks can be observed. The broad peak which covers a wide wavelength range originates

from the intrinsic-fluorescence of Si_xN_y , while the narrow peak appearing at 687 nm is the fundamental cavity mode which is modulated by refractive periodicity in our specific PCN design [151,152].



Figure 4.2 (a) design, (b) SEM image and (c) photoluminescence spectrum of L3 type Si_xN_y photonic crystal nanocavity. Scale bar is 2 μm . (Adapted from [153])

To match the energy level between the fundamental cavity mode of the Si_xN_y PCN and the plasmon mode of a gold nanoparticle, 150 nm spherical gold nanoparticles were chosen. In figure 4.3 a TEM image and the calculated absorption, scattering and extinction spectra of 150 nm spherical gold nanoparticles are shown.

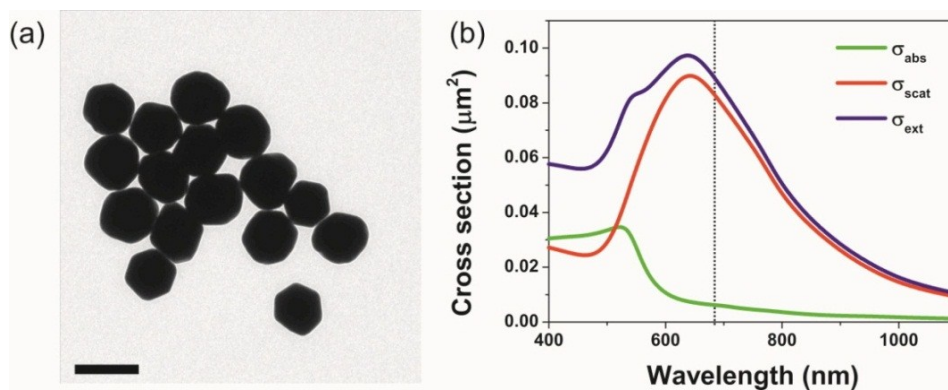


Figure 4.3 (a) TEM image and (b) calculated absorption, scattering, and extinction cross-sections of 150 nm spherical gold nanoparticles. The wavelength of the fundamental mode of the Si_xN_y nanocavity is marked with a dotted line. Scale bar is 200 nm. (Adapted from [153])

In contrast to smaller gold nanoparticles with diameters below 100 nm, 150 nm gold nanoparticles scatter efficiently while having a relatively small absorption cross

section. Moreover, due to the retardation effect [11], they possess a broad plasmon resonance peak over the VIS-NIR region (ca. 500–1100 nm) with a maxima at 642 nm. With this size of gold nanoparticles, the fundamental cavity mode of the PCNs at 687 nm overlaps adequately with the plasmon mode of 150 nm gold nanoparticles to provide energetic matching between two modes.

Gold nanoparticles are stabilized with negatively charged citrate and thus they are stable in water without forming aggregates during the experiments. To avoid non-specific binding between the Si_xN_y membrane and 150 nm gold nanoparticles, the Si_xN_y membrane is plasma cleaned to attain a negative charge on the surface prior to use.

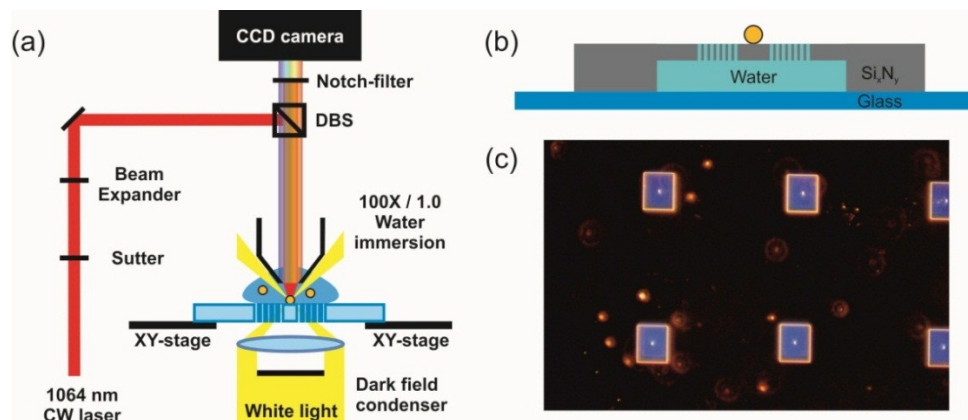


Figure 4.4 Schematic illustration of (a) laser printing setup and (b) detailed sample configuration. (c) Dark field microscope image of individual photonic nanocavities (blue scattering squares) and randomly diffusing 150 nm gold nanoparticles (red scattering dots) in water. (Adapted from [153])

To pattern a 150 nm gold nanoparticle onto a PCN, a single wavelength laser is used. Figure 4.4 shows the modified DFM setup equipped with a diode pumped solid-state cw laser used for printing gold nanoparticles. A 100 \times water dipping objective with a high numerical aperture ($\text{NA} = 1.0$) is used to focus the laser onto metal nanoparticles and to collect scattering light from the sample simultaneously. A mechanical shutter is placed in the beam path and controlled remotely by a control box during the printing process. A dark field condenser ($\text{NA} = 1.2\text{--}1.4$) focuses white light from the

bottom of the sample to illuminate it, and thus the behavior of the gold nanoparticles can be monitored. A thin glass coverslip (170 μm) is placed underneath the PCN membrane to avoid direct contamination from the microscope objective oil ($n = 1.518$). Water ($n = 1.33$) is filled into the empty layer in between the Si_xN_y membrane and the glass coverslip to correct for a refractive index mismatch as shown in figure 4.4b. With the above described configuration, individual PCNs and their corresponding defects can be distinguished as blue scattering squares and white scattering elongated dots, respectively. Also, colloidal gold nanoparticles on top of the Si_xN_y membrane can be seen as randomly diffusing bright orange spots as shown in figure 4.4c. To move the Si_xN_y membrane in the x - y plane precisely, it is fixed on a nano-precision stage and controlled by typing an arbitrary distance into the software.

4.2.3 Single gold nanoparticle printing onto a silicon nitride photonic crystal nanocavity

In figure 4.5 each step of the optical printing process is superimposed onto the calculated total force map. The magnitude and direction of forces exerted on a gold nanoparticle are calculated with a 1064 nm laser at 68 mW. In the laser printing process, the non-resonant 1064 nm laser is first focused slightly above the surface of the Si_xN_y membrane, and then a randomly diffusing gold nanoparticle (P1) near the laser is pulled into the laser beam (P2) by the gradient force exerted on the gold nanoparticle. When it is guided into an area where the laser intensity is higher, the scattering force exerting on the gold nanoparticle becomes larger resulting in propulsion along the laser propagation direction and then beyond the laser focus (P3). Consequently, when the accelerated gold nanoparticle arrives (P4) onto the surface of the Si_xN_y membrane, it is fixed onto the Si_xN_y membrane via strong van der Waals forces.

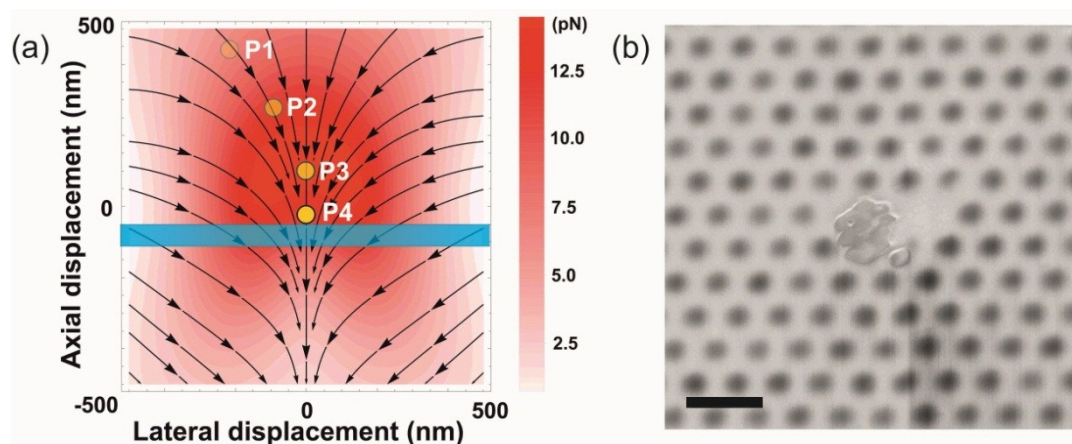


Figure 4.5 (a) The magnitude and direction of calculated total force exerting on a 150 nm gold nanoparticle (yellow dots) at different positions near the focused 1064 nm laser beam. The blue slab represents the Si_xN_y membrane. (b) SEM image of flattened 60 nm gold nanoparticles on a Si_xN_y nanocavity by 532 nm resonant wavelength laser. Scale bar is 400 nm.

Although the 1064 nm laser wavelength used in this study is off-resonant with the plasmon resonance of 150 nm gold nanoparticles, the direction of forces exhibits a typical feature of a force map where the scattering force is dominant. At a laser power of 68 mW, the calculated overall axial force exerted on a gold nanoparticle is 15 pN. No optical printing occurs below this laser power due to the small axial force. However, above this power, the probability of multiple particle printing increases with laser power. The magnitude of this force is comparable to the previous reports on optical printing of spherical gold nanoparticles with a resonant laser wavelength [35,140]. In theory, the axial force can be applied more effectively by using a laser wavelength resonant with the plasmon mode of the gold nanoparticles, since axial force increases proportionally with the extinction cross section. However, using a resonant wavelength laser for optical printing could cause optical heating of both gold nanoparticles and the Si_xN_y membrane. Gold nanoparticles absorb more light in the visible region than in the near infra-red region and thus would be heated much more efficiently by the resonant wavelength. The Si_xN_y membrane also absorbs visible light more efficiently than near infra-red light. As a consequence, heating of both the gold nanoparticle and Si_xN_y membrane makes printing onto the Si_xN_y membrane difficult due to the optically induced thermal energy which overwhelms the van der

Waals interaction, which is essential force for the binding. Using extreme laser power (532 nm, 100 mW) to push the 60 nm gold nanoparticles causes either deformation of the Si_xN_y membrane or melting of gold nanoparticles on the surface of the Si_xN_y membrane as shown in figure 4.5b.

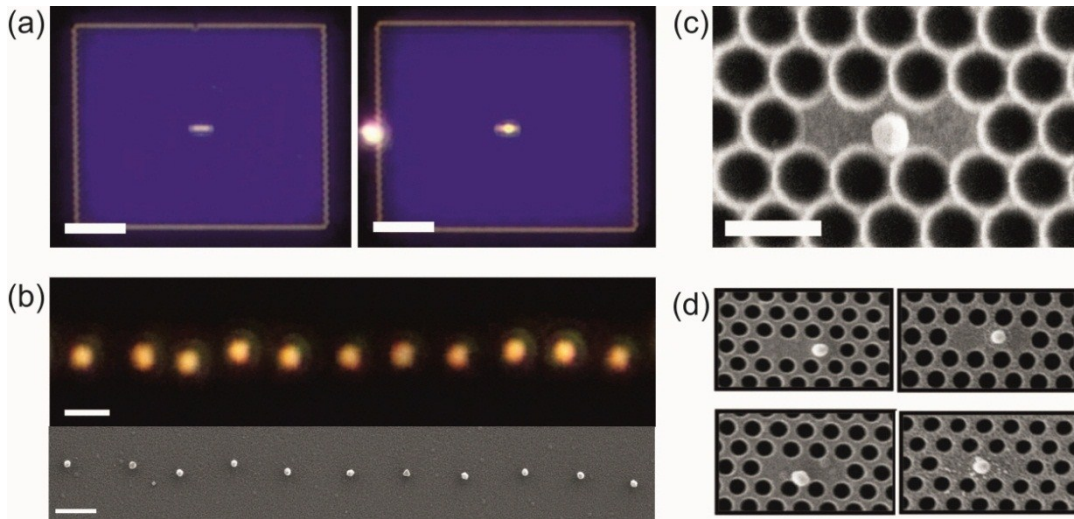


Figure 4.6 (a) Dark field microscope image of Si_xN_y PCN with and without a gold nanoparticle at its defect. Scale bar is 2 μm (b) Dark field microscope and SEM images of linearly printed gold nanoparticles for printing precision experiment. Scale bar is 1 μm . (c,d) SEM image of laser printed 150 nm gold nanoparticles on the defects of an L3 type Si_xN_y PCN. Scale bar is 0.5 μm . (Adapted from [153])

Figure 4.6a shows dark field microscope images of a Si_xN_y nanocavity with and without a gold nanoparticle on its defect. Bright orange scattering from a printed gold nanoparticle can be identified on the defect of the cavity located at the center of the PCN. A further SEM images (figure 4.6c,d) shows that the printed gold nanoparticle is firmly fixed on the Si_xN_y membrane and does not undergo any morphological changes during the laser printing process. However, among printed gold nanoparticles, only half of them are printed on the defect, whereas the others are printed slightly away from the defect. The 50 percent printing accuracy of this technique can be ascribed to two effects. First, the short axis of the defect (300 nm) is closed to the diffraction limit of the optics used in this study. Therefore, precise focusing the laser spot at the center of the short axis is virtually impossible. Second, the laser printing

technique has its own printing accuracy limit of ca. 50 nm due to the following reason [35,140]; When the gold nanoparticle is propelled from the laser focus along the laser propagation direction, the displacement of the gold nanoparticle from the laser axis fluctuates due to its entry angle and corresponding restoring optical force. Therefore, when a gold nanoparticle is printed on the substrate, its printed location and the laser axis are not necessarily coaxial. To determine the printing precision of our printing technique, 150 nm gold nanoparticles were printed in a line pattern on a Si_xN_y membrane and their displacements from a nominal line were measured. Figure 4.6b shows dark field microscope and SEM images of 11 printed gold nanoparticles on a Si_xN_y membrane. The standard deviation of printing precision was measured as 47 nm which is in good agreement with previously reported values [35,140].

4.2.4 Interaction between surface plasmons and fundamental nanocavity mode in hybrid nanocavity

Plasmons driven by fundamental cavity mode

To investigate the interaction between the plasmon mode of a gold nanoparticle and the fundamental cavity mode of a Si_xN_y PCN, we measured and compared photoluminescence spectra of Si_xN_y nanocavities with and without gold nanoparticles on their defects. In figure 4.7a the fundamental mode of the Si_xN_y PCN is plotted for both cases. In the absence of a gold nanoparticle, the line-width of the fundamental mode is 3.3 nm, whereas a line-width of 5.8 nm is found in the Si_xN_y PCN containing a gold nanoparticle. Moreover, the amplitude of the peak is also suppressed by factor of 3.6 when a gold nanoparticle is assembled with a Si_xN_y nanocavity. This peak broadening and damping is also found in other samples, regardless of small variation in the position of the gold nanoparticle on the defect. To understand this general tendency, our system is modeled and simulated by using the finite-difference time-domain method [154]. In figure 4.7b calculated fundamental modes of Si_xN_y

nanocavities in the presence and absence of a gold nanoparticle are overlaid. Calculations show that the line-width of the fundamental mode is broadened from 2.9 to 4.0 nm when the nanocavity contains a gold nanoparticle. Also, the amplitude of the peak reduced 0.7 times from the case of the nanocavity alone. In addition to the above qualitative agreement between experiments and simulation, a small red shift (~ 4 nm) of the fundamental mode from the experimental value can also be observed from simulation in the presence of a gold nanoparticle on a Si_xN_y nanocavity.

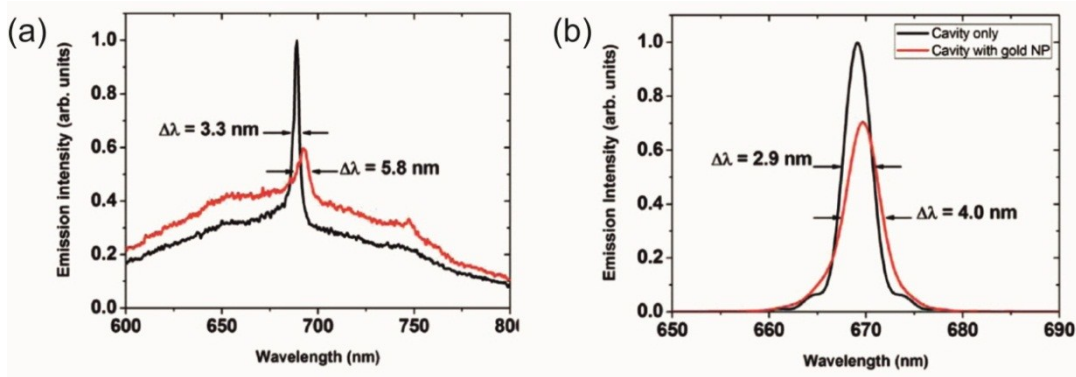


Figure 4.7 Plot of photoluminescence spectrum of a L3 Si_xN_y PCN before (black solid line) and after (red solid line) gold nanoparticle printing from (a) experiments and (b) simulation. (Adapted from [153])

To understand this broadening and damping of the fundamental mode, the evolution of the electromagnetic field was simulated by the finite differential time domain method. In figure 4.8a modeled decays of the electromagnetic field of the fundamental mode with and without a gold nanoparticle are plotted. By having gold nanoparticles on a Si_xN_y nanocavity, the lifetime of the electromagnetic field reduced from 204 fs to 112 fs. This, in turn, indicates that part of the energy which is initially stored in Si_xN_y is partially dissipated by the presence of the gold nanoparticle. To take a look into the details of this process, the electromagnetic field distribution of a gold nanoparticle conjugated to a Si_xN_y nanocavity are taken at different times, at 0, 100, 200, 300, 400, and 500 fs after the initial excitation as shown in figure 4.8b. It can be seen that at 150 fs after the initial excitation, build-up of the electromagnetic field propagates out of the Si_xN_y nanocavity slab. At 200 fs, the field becomes more

intense and is partially distributed over the surface of gold nanoparticles. Most of the field is diminished after 300 fs, however the energy dissipated from the PCN that drives the plasmon of a gold nanoparticle stays longer up to 500 fs. As a consequence of this partially dissipated energy which drives the plasmon of a gold nanoparticle, result in fast decays of the fundamental cavity.

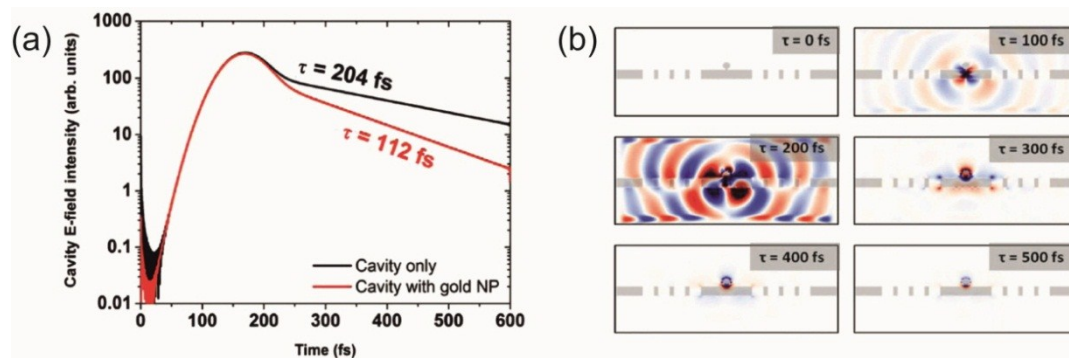


Figure 4.8 (a) FDTD modeled electromagnetic field ($|E_y|$) life time of the fundamental cavity mode of a L3 PCN with (red solid line) and without (black solid line) a gold nanoparticle on the nanocavity defect. (b) Distribution of $|E_z|$ component of electromagnetic field at various times after excitation. Cross-section of the nanocavity slab is colored grey. (Adapted from [153])

Effect of gold nanoparticle location in the cavity defect

As described earlier, due to the printing precision of our printing technique, the location of the printed gold nanoparticle on the defect can be slightly shifted from the center. Therefore it is necessary to investigate the effect of the gold nanoparticle location on the defect on the fundamental mode of the Si_xN_y PCN. We perform FDTD simulations of the fundamental cavity mode with respect to the different position of a gold nanoparticle along the x axis (long-axis of the defect) while the y position is fixed at 0. In figure 4.9a the $|E_y|$ field amplitude and percentage increase in cavity line-width are plotted as a function of the gold nanoparticle position along the x-axis. It is clearly shown that the electromagnetic field amplitude and the fundamental mode

bandwidth are closely correlated. This indicates that precise positioning on the gold particle in the defect allows tuning of the fundamental cavity mode in terms of the cavity quality factor.

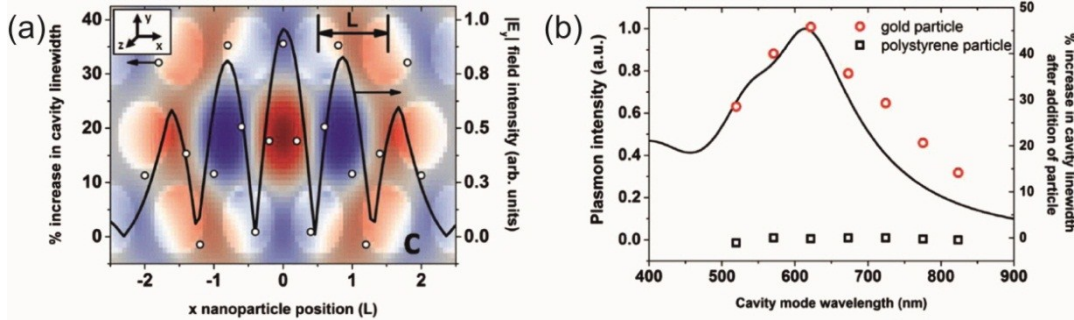


Figure 4.9 (a) Plot of FDTD modeled electromagnetic field ($|E_y|$, solid line), percentage increments of line-width (denoted as open dots) as function of gold nanoparticle position along x axis ($y = 0$). Background color denotes the amplitude of $|E_y|$ component in the electromagnetic field. (b) Plot of the calculated extinction spectrum of a 150 nm gold nanoparticle and percentage decrease of the fundamental cavity mode line width as a function of various cavity mode wavelengths in the presence of a 150 nm gold nanoparticle (red open circles) and a 150 nm polystyrene particle (black open square), respectively. (Adapted from [153])

We now turn to the discussion on energetic matching between the plasmon resonance mode of gold nanoparticles and the fundamental cavity mode. As mentioned earlier, the peak maximum of the plasmon resonance mode of a 150 nm gold particle is slightly blue shifted from the fundamental mode of Si_xN_y PCN, at 642 and 687 nm, respectively. To assess the effect of mode mismatch, we performed an FDTD simulation where the size and location of the gold nanoparticle was kept constant while the fundamental nanocavity mode was modulated by changing the lattice constant of the nanocavity. In figure 4.9b the percentage increase of the fundamental mode line width is plotted as a function of the cavity mode wavelength. The maximum increase in fundamental mode line-width is achieved when the fundamental cavity mode and the plasmon resonance mode of the nanoparticle are same wavelength. Consequently, the bigger the mismatch between the two modes, the smaller broadening of the fundamental mode line-width. An additional simulation was performed by replacing the gold nanoparticle with polystyrene beads of the same

size (150 nm) to assure that the line-width broadening occurred from mode mismatch. In contrast to gold nanoparticles, no line-width broadening is observed regardless of cavity mode wavelength shifts with the polystyrene beads.

4.2.5 Summary

Assembly of a plasmonic gold nanoparticle onto a L3 Si_xN_y photonic crystal nanocavity has been realized using single wavelength focused laser. A 1064 nm non-resonant laser was used to optically print individual 150 nm spherical gold nanoparticles onto the sub-micron defect of the nanocavity with a printing precision of ~ 50 nm. The Si_xN_y photonic crystal nanocavity showed broadening and damping of its fundamental nanocavity mode in the presence of a 150 nm gold nanoparticle. Time-resolved simulation revealed that the broadening and damping of the nanocavity fundamental mode arised from the use of partially dissipated electromagnetic energy to drive plasmon of the gold nanoparticle. Moreover, the effect of the gold nanoparticle location within the defect on the fundamental mode line-width was studied. The simulation shows that the line-width and electromagnetic field intensity are closely correlated. Also, the energetic matching between Si_xN_y nanocavity and plasmon modes was investigated. It was revealed that the change in line-width is maximized when the energy levels of the two modes are the same.

5. Hierarchical assembly of planet-satellite type nanostructures by using DNA origami technique

In this chapter, the assembly of hierarchical *planet-satellite type nanostructures* composed of metal nanoparticles, quantum dots, and organic dyes will be discussed. By using DNA origami technique, nanoscale elements are arranged into planet-satellite type structures with controllable composition, stoichiometry and defined inter-elemental distances. Furthermore, electroless metal overgrowth allows for the capability of tuning their morphology on a substrate as well as in solution. Prepared nanostructures allow us to quantitatively study the distance-dependent fluorescence quenching of dye molecules by gold nanoparticles. These structures show promise for harvesting light and amplifying circular dichroism signals.

5.1 DNA origami technique for spatial arrangement of gold nanoparticles

In the growing fields of nanophotonics, metamaterials, and biotechnology, it has become important to precisely arrange nanoscale elements [155,156]. *Top-down* techniques such as electron-beam lithography and photolithography have been utilized to create highly ordered nanostructures over wide areas. These techniques are limited, however, in their ability to create nanostructures with complex, three-dimensional morphologies. As an alternative approach, *bottom-up* methods allow for the creation of large numbers of highly homogeneous nanostructures with sophisticated morphologies. The recently developed DNA origami technique [37] is one of the state-of-the-art *bottom-up* methods to create precise and complex shaped nanostructures, which cannot be realized by conventional lithography methods.

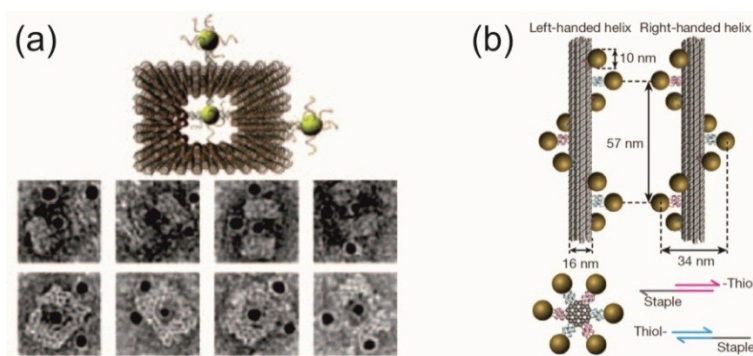


Figure 5.1 Spatially arranged gold nanoparticles created with (a) DNA nanocages and (b) chiral DNA helix bundles structures. (Adapted from [157,158])

Precise spatial arrangements of gold nanoparticles within a nanoscale object have been previously reported based on the DNA origami technique. In this approach, gold nanoparticles are attached on spatially addressable docking-sites in the DNA origami structure via Watson-clock base pairing. In one example, DNA-functionalized gold nanoparticles are encapsulated by DNA nanocages where several complementary DNA linkers are positioned on the walls of the hollow interior [157]. The DNA nanocage is further decorated with more gold nanoparticles on its outer walls,

resulting in an arrangement of gold nanoparticles with well-defined separation distances as shown in figure 5.1a. Gold nanoparticles can also be spatially arranged on radial spokes of DNA helix bundle structures for studying circular dichroism, as shown in figure 5.1a [158]. The chirality of the arranged gold nanoparticles in this structure gives rise to circularly polarized light in the same direction.

In this work, we use the DNA origami technique to arrange smaller satellite nano-elements in orbit around a larger planet nano-element. The overall size of assembled planet-satellite like nanostructures can be up to 500 nm in any one dimension – beyond the typical size regime of DNA-based nanostructures made of short molecular linkers [159]. The hierarchical assembly approach of this method allows creating planet-satellite type nanostructures (PSNs) with different elemental composition, stoichiometries, inter-elemental distances, and overall sizes. Moreover, these hetero-nanostructures provide various platforms to study distance-dependent fluorescence quenching, light-harvesting antenna, and signal enhancement of circular dichroism.

5.2 Design and preparation of planet-satellite type nanostructures

The structural composition of the planet-satellite type nanostructures can be categorized into two different building blocks: planet and satellite. As the name suggests, the planet is located at the center of the PSN and provides a solid base for the assembly of the satellites. To construct the PSN, the building blocks are prepared and assembled in sequential steps. In the first step of this hierarchical assembly, the surface of metal nanoparticles and quantum dots are functionalized with thiolated DNA oligos. Secondly, DNA origami structures of various size and shape are designed and prepared with the DNA origami technique. Third, DNA origami structures and their counter-parts elements (metal nanoparticles, quantum dots, and fluorescent dyes) are assembled to form satellites. In the last step, prepared satellites

adhere to the planet to create the PSN in its final form. In the following discussions, details of design and preparation of each step will be explained.

Step 1. Preparation of DNA-functionalized metal nanoparticles and quantum dots

Bare metal nanoparticles tend to aggregate in solution to minimize their surface area to volume ratio, which is energetically favorable. To have gold nanoparticles stable in solution without forming aggregates, various stabilizing chemicals can be introduced on their surface [160]. When their surface is covered with charged chemicals, the aggregation of the metal nanoparticles is effectively avoided due to electrostatic repulsion. Typically positively charged CTAB or negatively charged citrate is widely used as stabilizing chemicals. In the same sense, DNA oligos can also be used since they have highly a negatively charged phosphate group on their backbone. Thus DNA oligos functionalized metal nanoparticles can be stabilized in solution [161,162]. Furthermore, DNA oligos do not only work as stabilizers, but also as molecular linkers for the further assembly with their complementary DNA oligos [163].

In this work, metal nanoparticles and quantum dots are functionalized with DNA oligos to achieve high colloidal stability and grant DNA-binding specificity. DNA oligos on the surface allow them to be assembled with DNA origami structures which possess complementary DNA linkers in their docking-sites. To introduce DNA oligos on the surface of metal nanoparticles and quantum dots, we use thiol-modified DNA oligos which can be functionalized via covalent thiol bonding.

Preparation procedures of DNA-functionalized metal nanoparticles are described as follows. Differently sized citrate-stabilized metal nanoparticles are purchased from *BBI International*. Gold nanoparticles are concentrated by exchanging the initial stabilizer with BSPP (Bis(p-sulfonatophenyl)phenylphosphine dihydrate dipotassium salt) followed by the addition of highly concentrated sodium chloride solution (5 M).

The solution is centrifuged and redispersed in a 50% methanol solution and BSPP solution sequentially. In a separate batch, TCEP (Tris(carboxyethyl)phosphine hydrochloride) and HPLC grade thiol-modified single-stranded DNA (*biomers.net*) are mixed and kept for an hour to activate the thiol bonds. The prepared BSPP-functionalized metal nanoparticle solution and the excess thiol-modified single-stranded DNA solution are diluted in a $0.5\times$ TBE buffer solution. To achieve a fast reaction, the pH of the solution is adjusted as described in the work of Zhang et al [164], and results in a high-yield of DNA-functionalized metal nanoparticles within few minutes. The coverage of DNA on metal nanoparticles is further determined by the color change follows by addition of 100 mM magnesium chloride (MgCl_2) solution. In figure 5.2a normalized extinction spectrum of differently sized DNA-functionalized gold and silver nanoparticles are plotted. Gold nanoparticles show a clear plasmon resonance mode in visible wavelength, with the peak maxima shifted to longer wavelengths as they increase in size. The plasmonic resonance mode of silver nanoparticles appears at 400 nm, which is higher energy than that of the gold nanoparticles.

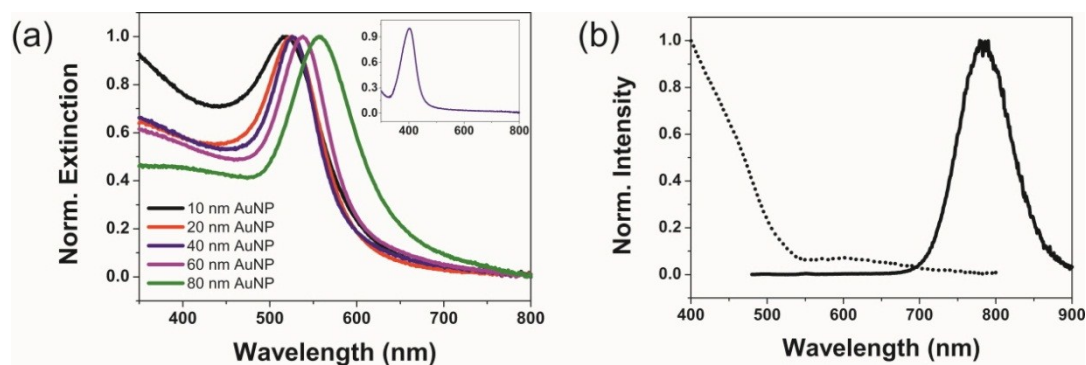


Figure 5.2 (a) Normalized extinction spectra of differently sized DNA-functionalized spherical gold nanoparticles in water. A 20 nm spherical silver nanoparticles is shown in the inset image for comparison. (b) Normalized absorption (dotted line) and fluorescence emission (solid line) spectra of DNA-functionalized CdSeTe quantum dots in water.

DNA-functionalized quantum dots are prepared with CdSeTe nanocrystals (*Invitrogen*) which have a fluorescence emission peak maximum at 800 nm. First, initial surface ligands are exchanged to 3-mercaptopropionic acid. Phosphorothioate modified DNA (PTO-DNA) is then mixed with quantum dots and incubated at 90 °C for 40 min. Excess PTO-DNA is removed by series of filtration steps (100 KDa MWCO centrifugal filters) and redispersed in water. In figure 5.2b normalized absorption and fluorescence emission spectrum of DNA functionalized CdSeTe quantum dots in water are shown.

Step 2. Design and preparation of DNA origami structures

To tune the morphology and functionality of PSN, various geometries of DNA origami structures are prepared. In this work, DNA origami structures with different size, shape, and lattice are prepared by folding a linear single-stranded *scaffold* DNA strand with help of different combinations of short DNA *staples*. Depending on the helices arrangements, this forms either honeycomb or square lattices as shown in figure 5.3 of cross-section view of two different DNA origami structures.

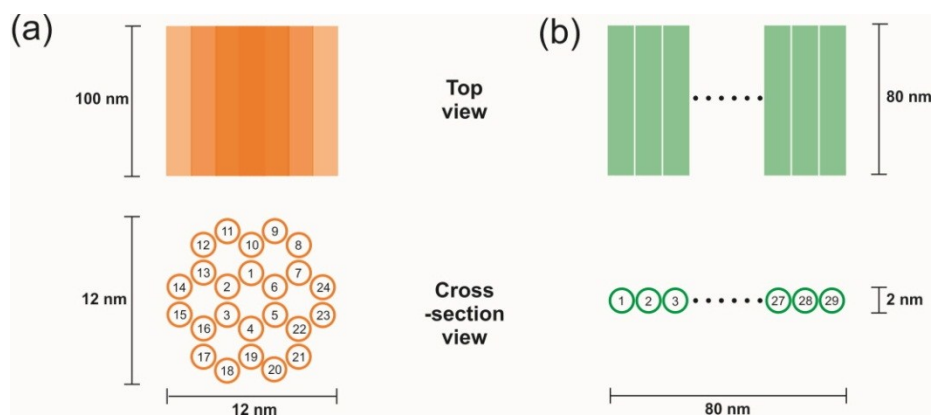


Figure 5.3 Top and cross-section view of designed (a) 24-helix-bundles and (b) DNA-sheets. Each circle and cylinder represents one DNA double helix.

The design and preparation of DNA origami structures will be explained using two examples: *24-helix-bundles* (24 HB) and *DNA-sheets*. The design of DNA origami structures is done using the open-source *caDNAno* program. As a scaffold of DNA origami structures, single stranded P7560 was used where sequences of 7560 bases are known. Individual DNA staples hybridize to a scaffold DNA to form a single segment of double helical DNA. Depending on the DNA design, the sequence of staple DNAs are customized by using scaffold DNA sequence as an input. The final DNA origami structures are constructed from the product of all segments. Neighboring segments are connected by interhelix connections (via non-migrating Holiday junction) either with scaffold DNA or DNA staples. In figure 5.3, 100 nm long 24× DNA helices arranged into honeycomb lattice and form 24-helix-bundles structure with overall size of 100 nm (L) × 12 nm (W) × 12 nm (H). DNA-sheets are created with 80 nm long 29× DNA helices by arranging them onto a two dimensional plane to form an approximately 80 nm (L) × 80 nm (W) × 2 nm (H) flat structure.

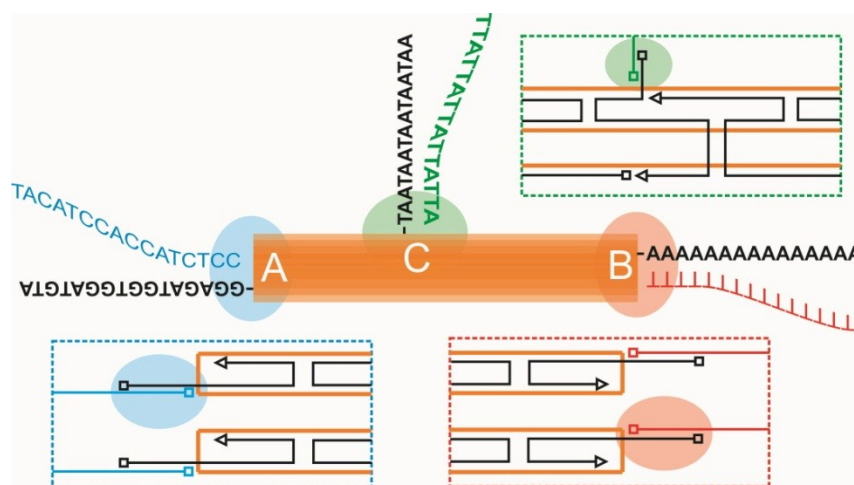


Figure 5.4 Illustration of DNA docking-sites of 24-helix-bundles structure. Orange colored cylinders represents DNA double helices. Blue, red, and green areas represent different docking-sites.

All designed DNA origami structures have at least one docking-site to connect them to other components: metal nanoparticles, quantum dots, and fluorescent dyes. Each docking-site contains DNA linkers with specific base sequences which are

complementary to the one of DNA oligos in counter-part component. In figure 5.4 three available docking-sites in 24-helix-bundle are shown in different colors, which are located at two ends (A and B) and side (C) of structure. In A and B, DNA linkers are overhang from the DNA origami structure along the helical axis of DNA helices and thus provide docking-site at each end of elongated DNA origami structure. In contrast to A and B, DNA linkers in C poke out of the DNA helix which are perpendicularly aligned to the helical axis. The exact location and amount of DNA linkers at each docking-sites can be customized. Typically, DNA linkers have DNA sequences where first half is complementary to the base sequence of specific part of scaffold DNA, which constitutes the helices in a DNA origami structure. The second half of the DNA linkers do not hybridized with scaffold DNA, and instead contribute to further assembly between the DNA origami structure and other coomponents. It is noteworthy that the role of DNA linkers is not limited to addressing docking sites for further assembly, but also for prohibiting un-desired multimerization among DNA origami structures. Multimerization of DNA origami structure will be thoroughly discussed in next section.

Folding DNA origami was done by mixing scaffold DNA (10 nM) and various DNA staples (each 100 nM) in 0.5×TE buffer containing divalent MgCl₂. Single-stranded P7560 extracted from *m13mp18* bacteria phage is used as scaffold DNA. To achieve high self-assembly yield while minimizing structure defects and aggregation, MgCl₂ concentration was varied from 1 mM to 200 mM to determine optimum MgCl₂ concentration. In the first step of assembly, 50 uL of mixture was heated to 80 °C for complete dehybridization of all double-stranded DNA with thermal cycler. Upon reaching 80 °C, the chemical mixture cooled down slowly to allow for self-assembly of the scaffold and DNA staples into the desired DNA origami structures. Two cooling steps with different cooling rates were conducted. Firstly, the mixture cooled from 80 °C to 60 °C with a cooling rate of 0.2 °C/min. In the second cooling step, the temperature dropped from 60 °C to 25 °C at a rate of 0.05 °C /min. Typically, 3D DNA origami structures required a slower cooling rate than simple 2D DNA origami structures due to their structural complexity [106].

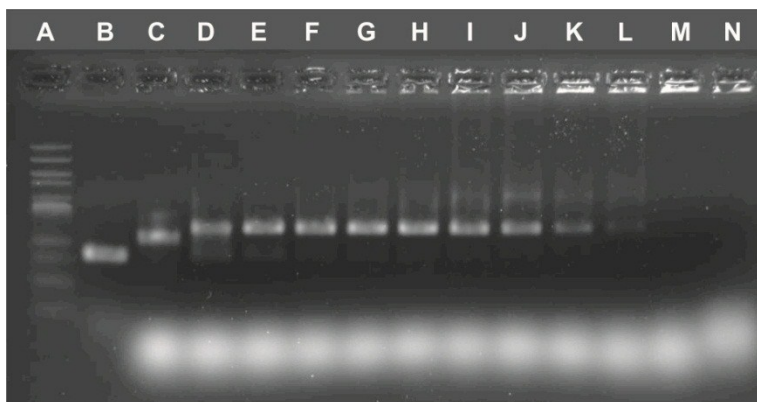


Figure 5.5 Fluorescence image of run gel of 2D DNA-sheets folding at different MgCl_2 concentration. From left to right, DNA ladders (A), P7560 (B), 1 (C), 4 (D), 10 (E), 12 (F), 14 (G), 16 (H), 18 (I), 20 (J), 24 (K), 28 (L), 50 (M), 200 (N) mM MgCl_2 .

Once self-assembly is terminated at room temperature, the resulting structures are separated by running the reaction mixture through an agarose gel matrix. In figure 5.5 fluorescence image of stained (ethidium bromide) gel for 2D DNA-sheets is shown. DNA Ladder (A) and scaffold DNA (B) were ran together with reaction mixtures in a separated slot to determine approximate molecular weight of folded DNA origami structures depending on MgCl_2 concentration.

In the assembly with 1 mM MgCl_2 (C), a clear band is observed, which ran slower than the scaffold DNA band. This indicates the formation of another structure with higher molecular weight than of the scaffold DNA. However, by increasing MgCl_2 concentration up to 4 mM (D), yet another new DNA structure is created with an even higher molecular weight. This new band kept its eluent position over the MgCl_2 concentration between 4 mM (D) to 28 mM (L) whereas distinct band at 1 mM sample is no longer present. Since each single stranded DNA is highly negatively charged, a sufficient amount of screening ions (magnesium or sodium) are required for the formation of these structures to overcome electrostatic repulsion between DNAs molecules. Therefore, increasing magnesium cation from 1 mM to 4 mM can successfully assemble DNA origami structures with high DNA density.

However, an upper-limit of screening ions concentration is also exist. If the concentration of screening ions is too high, it screens not only the charge within individual DNA origami structures but also the charge among DNA origami structures. This upper-limit is important to obtain not only high yield, but also adequate stability of DNA origami structure for long term storage. To determine the upper-limit of magnesium ion concentration, the sharpness of elution band has to be taking into account, which represents a mono-dispersity of DNA origami structure. By increasing ion concentration from 1 mM (C) to 12 mM (F), the distinct band became clearer, without blurring around it. However, further increasing magnesium ion concentration above 12 mM, a number of blurry bands re-appear in the larger molecular weigh region. Along with band clearness, the existence of DNA in the gel pocket has also to be considered. If DNA origami structures are aggregated and form a cluster of DNA origami structures, they will not migrate through the gel matrix due to their large size compared to gel matrix pore size. The clear tendency can be observed that amount of DNA inside the pocket increases with MgCl_2 concentration and became obvious when magnesium ion concentration is above 18 mM (I). In the extreme condition with 50 (M) and 200 (N) mM MgCl_2 in solution, all DNA are captured in the pocket and no other band can be observed. The excess of staples (10 times) are seen as the largest blurry band at the bottom of gel, owing to their small molecular weight.

Based on above discussion, 11 mM MgCl_2 has been chosen for optimum concentration of MgCl_2 for folding DNA-sheets. Same optimum magnesium concentration is found for 24-helix-bundles. This condition, however, is only valid for one specific design of DNA origami structures. Therefore this test has to be redone for differently shaped DNA origami structures.

The identified clear band is cut from the gel and mashed finely with knife to extract self-assembled DNA origami structures from the dense gel matrix. Mashed gel is centrifuged with Freeze' N Squeeze spin columns at 4 °C at 5000 rcf. Transparent purified DNA origami structure are collected and their structure is examined with electron microscope analysis. In figure 5.6 schematic illustration and TEM images of

DNA-sheet, DNA-block, 24-helix-bundles, and 14-helix-bundles structures are shown.

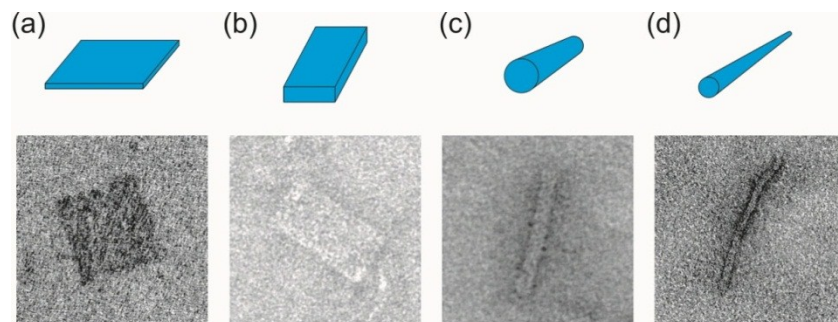


Figure 5.6 Illustration and TEM images of (a) DNA-sheet ($80 \times 80 \times 2$ nm), (b) DNA-block ($30 \times 60 \times 10$ nm), (c) 24-helix-bundles ($100 \times 16 \times 16$ nm), (d) 14-helix-bundles ($200 \times 12 \times 12$ nm).

Now we turn to discussion on potential multimerization of DNA origami structures during their self assembly process. As we discussed in Chapter 2, there are two forces which contribute on the stability of double-stranded DNA: base pairing and base stacking. Among them, base stacking can potentially cause dimerization of DNA origami structures. A nearly flat aromatic DNA bases in each helix bundles of DNA origami structure are oriented perpendicular to the helical axis. The first and last base pairs in each DNA helix are exposed to the solution and thus provides additional attractive sites owing to the presence of the partially delocalized π -electrons in aromatic bases. Therefore, each DNA origami structure could potentially attract other identical DNA origami structure via base stacking. However, this mulimerization can be avoided by leaving few bases on scaffold DNA unbound to any DNA staples, so called *blunt-end*.

To study this effect, two types of DNA-sheets with differently designed ends are compared. Both types of DNA-sheets have 30 linkers at one side of the structure where the helix bundles terminate. On the opposite side, one of the DNA-sheets is completely hybridized with staple DNAs, whereas the other is not. The detailed design of the helix end at each of DNA-sheets is shown in figure 5.7. If all sequences of scaffold DNA are paired with DNA staples in the *open-end* case (a), the exposed

aromatic base will face to the solution. Therefore, another *open-end* DNA-origami-sheet in solution can easily access and form dimer via base stacking interaction. However, in *blunt-end* case (b), some sequences of scaffold DNA at the structure ends are left unbound to any DNA staples. The orientation of remaining unbounded aromatic bases is no longer be orthogonal to the helical axis owing to the small persistence length of single-stranded DNA [165]. In figure 5.7 this effect is clearly shown in their TEM images, where DNA-sheets are found as either monomers or dimers, depending on the design of their end. Furthermore, the DNA linkers at the opposite ends also effectively prevent dimerization of DNA-sheets. Relatively long single stranded linkers (18A) stretched out from structure end, preventing base-stacking between two DNA-sheets. It is noteworthy that DNA linkers with specific base sequences such as multiple A or T can provide better blocking on base stacking than random sequence linkers.

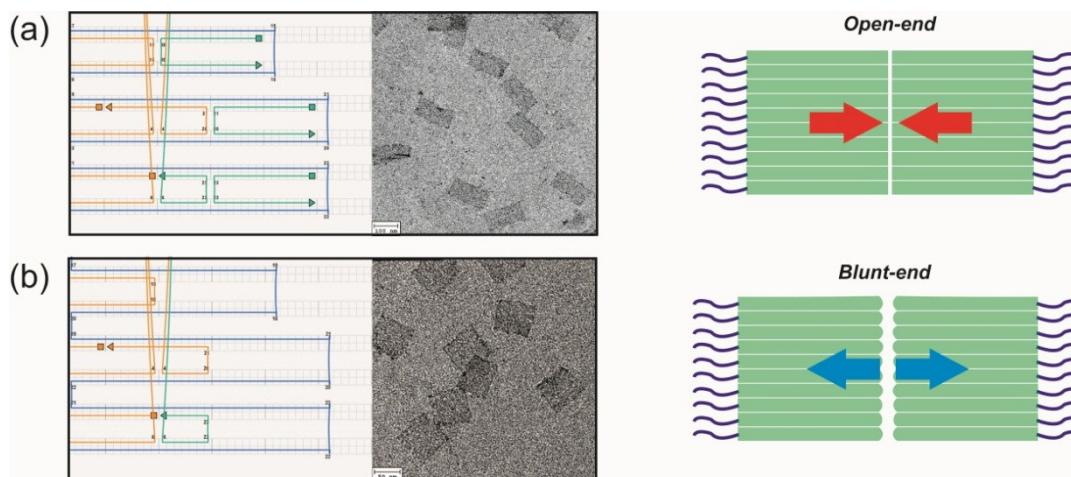


Figure 5.7 *caDNA* design and TEM image as well as schematic illustration of dimerization behavior of (a) open-end and (b) blunt-end DNA-sheets.

Step 3. Assembly of satellites

Depending on the final structure of PSN, the composition of satellites can be chosen either DNA origami structure alone or DNA origami structure containing different type of components (metal nanoparticles, quantum dots or organic dyes). The composition of satellites can be categorized into three different types, depending on number and location of docking-sites in the DNA origami structure. Possibilities include one docking-site at one end, one docking-site on each end, and one docking-site at one end and multiple sites on the side. One of the docking sites will be used in the final assembly step to assemble satellites and planet into final PSN. Therefore, remaining docking-sites can be used to assemble other components onto DNA origami structures.

The satellite assembly is done via base pairing between two complementary DNA linkers which are functionalized in the DNA origami structure and other counter-part components. Preparation of satellites is done by mixing excess amount of counter-part components into solution containing DNA origami structures to avoid formation of multimers. The excess of counter-part components are then removed with gel electrophoresis.



Figure 5.8 Schematic illustration of assembly of DNA functionalized 10 nm gold nanoparticles and 24-helix-bundle structure.

Figure 5.8 shows illustration of assembly between 10 nm gold nanoparticles and 24-helix-bundles via base pairing. To achieve high yield for hybridization, an excess of gold nanoparticles should be used for assembly. If the number of gold nanoparticles is equal or slightly bigger to the DNA origami structure, more than one DNA origami

structure will bind to single gold nanoparticle. Typically, a 1:10 ratio between DNA origami structures and gold nanoparticles provides stoichiometric binding between them. In table 5.1 the optimum mixing ratio between DNA origami structures and counter-part components are summarized.

To apply this optimum mixing ratio condition, it is important to know the concentration of each sample before conducting assembly. First, to know the concentration of DNA origami structure solution, the Beer-Lambert equation is used: $A = \epsilon lc$, where A is optical density, ϵ is molar absorption coefficient, l is path length, and c is sample concentration. UV-Vis spectrometer (*Nanodrop*) is used to measure optical density of the sample with small volume around a few microliters. DNA absorbs light in UV region with its absorption maximum at around 260 nm with the existence of an aromatic ring in each base. Paired bases in double stranded DNA absorb less than the one unpaired base in single stranded DNA with molar absorption coefficients (ϵ) of $\epsilon_{dsDNA} = 20 \text{ L}\cdot\text{g}^{-1}\text{cm}^{-1}$ and $\epsilon_{ssDNA} = 27 \text{ L}\cdot\text{g}^{-1}\text{cm}^{-1}$, respectively.

Satellites	DNA origami structures (A)	Metal nanoparticles, quantum dots, dyes (B)	Mixing ratio (A : B)
HB@MeNP, DNA-block@MeNP	Helix-bundles, DNA-block	Metal nanoparticles	1:10
9× AuNP helix	24-helix-bundles	Gold nanoparticles	1:90
4× AuNP row	24-helix-bundles	Gold nanoparticles	1:40
20× dye row	24-helix-bundles	Cy3 dyes	1:200

Table 5.1 Mixing ratio between DNA origami structures and metal nanoparticles, quantum dots, and fluorescence dyes.

To estimate the molar absorption coefficient of DNA origami structures, it is necessary to know the number of unpaired and paired bases in its structure. As an example of this calculation, single DNA-sheet contains 1,200 unpaired and 13,260 paired bases is considered. The overall molar extinction coefficient of DNA-sheet is then multiplication of number of bases by its corresponding molar absorption coefficient value: $\epsilon_{DNA\text{sheet}} = (\epsilon_{dsDNA} \times 13,260) + (\epsilon_{ssDNA} \times 1,200) = 29.76 \times 10^4 \text{ L}\cdot\text{g}^{-1}\text{cm}^{-1}$. From the calculated molar absorption coefficient and the measured values, the

mass concentration (g/L) of DNA-sheet can be derived via Beer-Lambert equation. The mass concentration is further converted to molar concentration (M) by adapting a molecular weight of DNA-sheet which is calculated by multiplying the average molecular weight of single bases (303.7 g/mol) and total number of bases (14,460).

Concentration of other components such as metal nanoparticles, quantum dots, and dyes are determined with same principle from their known molar extinction coefficients. Prior to assembly, all the samples are purified extensively with spin filters to ensure that there are no free DNA linkers, which can significantly affect the assembly yield. Assembled satellites are further purified with gel electrophoresis in order to remove the excess from the mixture. Figure 5.9 shows the illustration and TEM image of various satellites assembled in the optimized conditions described above.

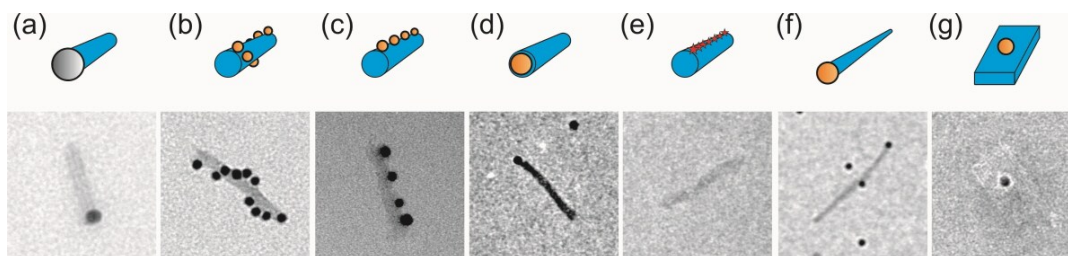


Figure 5.9 Illustration and TEM images of satellites. (a) 24 HB@20 nm AgNP, (b) 24 HB@9×10 nm AuNP, (c) 24HB@4×10 nm AuNP, (d) 24 HB@10 nm AuNP, (e) 24 HB@20×Cy3 dyes, (f) 14HB@10 nm AuNP and (g) DNA-block@10 nm AuNP.

Step 4. Assembly of planet-satellite type nanostructures

As a final step of hierarchical assembly, prepared satellites are further assembled with DNA functionalized planet to create PSNs. In this work, gold nanoparticles, quantum dots are used as planets. This assembly is based on base pairing between complementary DNA sequences of the planet and satellites. To achieve full coverage

of satellites onto the planet surface, an excess amount of satellites are added. Table 5.2 shows the optimized mixing ratio between planet and satellites depending on the size and type of planets. With bigger gold nanoparticles, the planet has a larger surface area, and more satellites need to be added.

Planet (nm)	Mixing ratio (planet:satellite)
10 nm AuNP	1:20
20 nm AuNP	1:200
40 nm AuNP	1:500
60 nm AuNP	1:700
80 nm AuNP	1:1,000
Quantum dots	1:20

Table 5.2 Mixing ratio between planet and satellite for assembly

Figure 5.10 shows the assembly of 60 nm gold nanoparticle (planet) and 24-helix-bundles containing 10 nm gold nanoparticle (satellites). 19× thymine (19T) linkers from the planet and multiple adenine (15A) linkers from 24-helix-bundles are hybridized to form PCNs. Due to the presence of excess amount of the satellites, the hybridization undergoes until the planet is fully covered with the satellites. The details of size, stoichiometry and inter-particle distance of assembled PSNs will be discussed in next sub-chapter thoroughly. In figure 5.11 the illustration of the planet with satellites and TEM images of resulting assembled PSNs are listed.

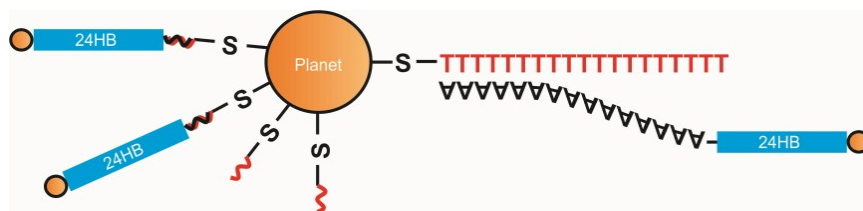
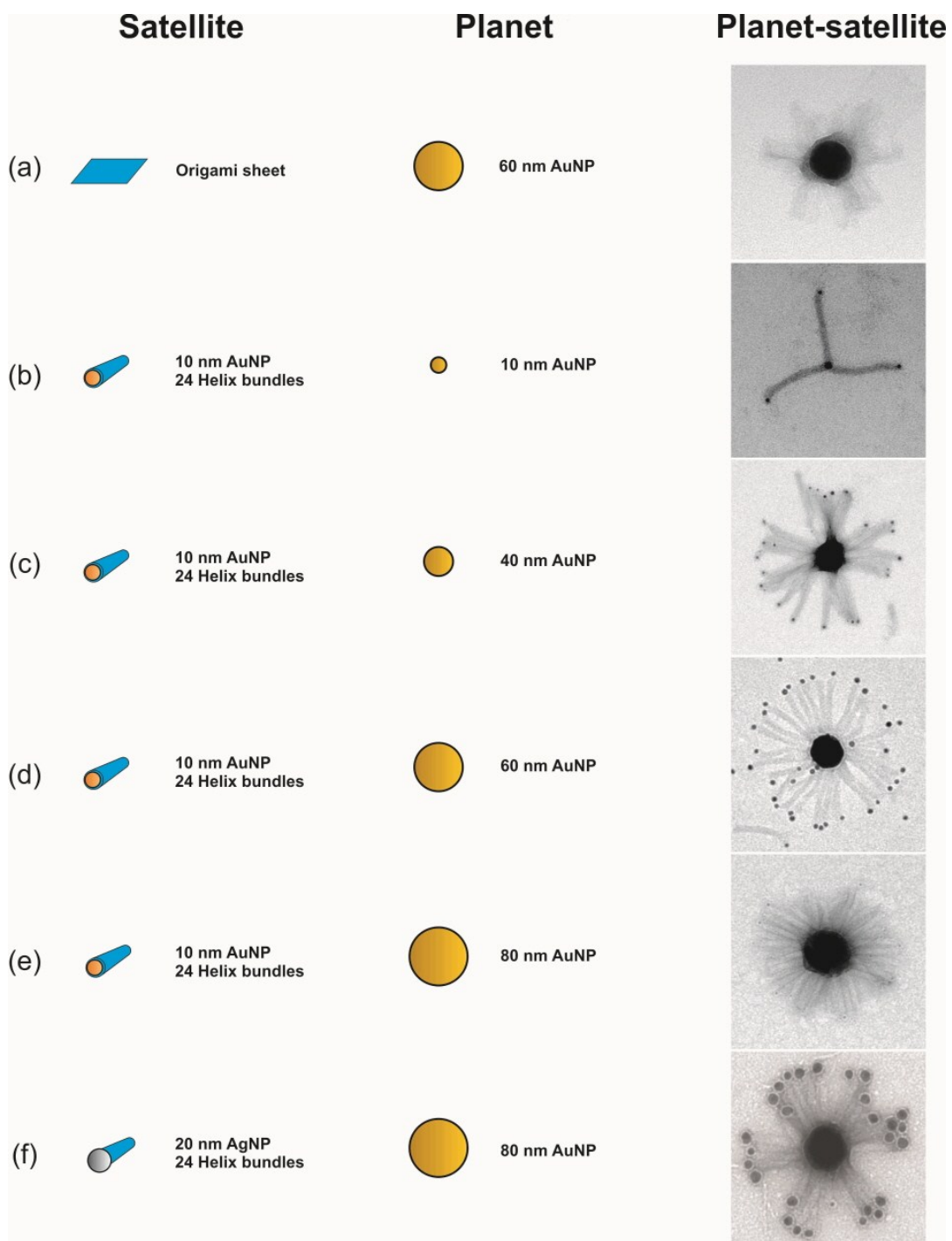


Figure 5.10 Schematic illustration of assembly between 24HB@10 nm AuNP satellites and a 60 nm AuNP planet.



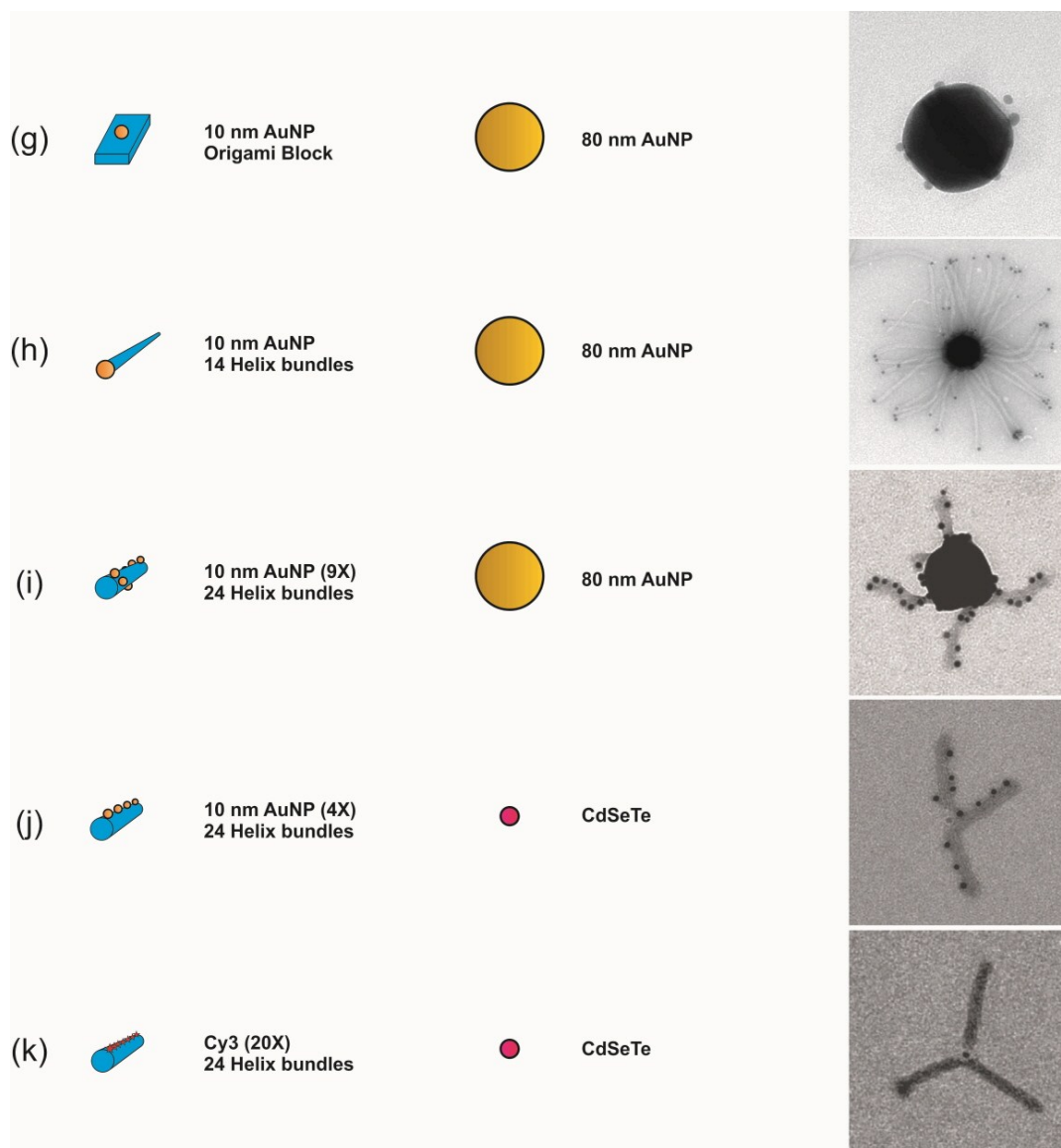


Table 5.11 Illustration of planet and satellites and their corresponding TEM images of planet-satellite type structures. The structures are summarized as *planet/satellite*. (a) 60nm AuNP/DNA-sheets, (b) 10nm AuNP/24HB@10nm AuNP, (c) 40 nm AuNP/24 HB@10 nm AuNP, (d) 60 nm AuNP/24 HB@10 nm AuNP, (e) 80 nm AuNP/24 HB@10 nm AuNP, (f) 80nm AuNP/24 HB@20nm AgNP, (g) 80 nm AuNP/DNA-block@10 nm AuNP, (h) 80 nm AuNP/14 HB@10 nm AuNP, (i) 80 nm AuNP/24 HB@9×10 nm AuNPs, (j) CdSeTe/24 HB@4×10 nm AuNPs and (k) CdSeTe/24 HB@20×Cy3 dyes.

Long-term stability of planet-satellite type nanostructures

The stability of assembled PSNs was also tested under different storage temperatures. Theoretically, PSNs are stable below the melting temperature of DNA origami structures, which is around 55 °C. However, degradation takes place over time when stored at room temperature. For long term storage, it is necessary to keep PSNs well below their melting temperature. At -18 °C, the morphology of PSNs are stable even for up to two years. PSNs can potentially become flocculated in long-term storage, however, a short sonication (< 10 s) process re-disperses them without damaging their structure.

5.3 Tuning the morphological properties of planet-satellite type nanostructures

Tuning the stoichiometry between planet and satellite

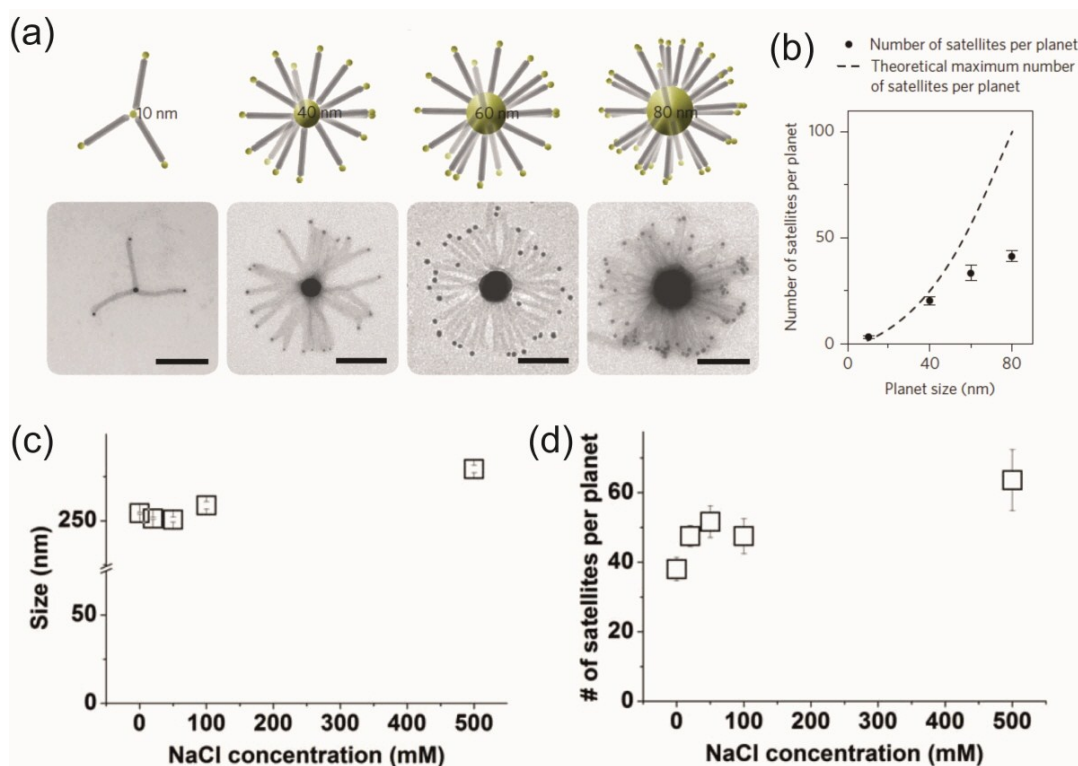


Figure 5.12 (a) Illustration and TEM images of PSNs with different planet diameters. (b) Measured and calculated plot of the number of satellites in single PSN as function of planet diameters. (c) Hydrodynamic size and (d) number of satellites in single PSNs consisting of 80 nm gold planet and 24 HB@10 nm AuNP satellites as function of NaCl concentrations (Adapted from [166])

The number of satellites on an individual PSN can be controlled by changing the size of the planets. As shown in figure 5.12a the number of satellites in a single PSN increases with diameter of planet. In theory, the surface area of the planet nanoparticle increases with a factor of r^2 , where r is radius of the particle. Therefore, the number of satellites bound to the planet should also increase with the same

dependency. However, experimental observation shows a linear dependence, as shown in figure 5.12b. This difference can be explained by the existing negative charges among the DNA origami structures. 11 mM MgCl_2 in the medium is sufficiently high to screen the negative charges of the DNA helices, but not so much as to induce aggregation among DNA origami structures. Therefore, the packing density of DNA origami on the gold surface is limited by repulsive forces among the other DNA origami structures. This effect becomes smaller with smaller planet size, where surface curvature is high. On a highly curved surface, neighboring DNA origami structures are separated enough to not affect each other. However, with a bigger planet, DNA origami structures are aligned almost parallel, so the repulsive force is significant. As a consequence, each DNA origami structure on a big planet takes up more space, which is enough to minimize repulsive forces from its neighbors. For experimental verification, we conducted DLS measurements and TEM image analysis to assess the effect of repulsive force on the hydrodynamic size and the packing density of satellites, respectively. The repulsive force among the DNA origami structures is modulated by adding different contents of sodium chloride into the PSNs solution. Results show that the effect of sodium chloride on the overall size of PSNs is small, only a 10% size change is observed. However, the number of satellites increases nearly 30%. This means that the density of satellites on the planet surface can be increased by screening the negative charges of the individual satellites on the planet surface without forming PSNs aggregates.

Tuning the inter-particle distance

It is shown in figure 5.13a that the inter-particle distance between the planet and satellites can also be controlled. By employing DNA origami structures with various length of 10, 100, and 200 nm as spacer, this distance can be precisely controlled. Figure 5.13b shows inter-particle distance distribution of measured distance from planet to small gold nanoparticles (surface to surface) based on TEM imaged of each samples. A clear tendency is observed that the longer the length of the DNA origami

structures, the farther the distance from planet gold nanoparticle to the small gold nanoparticles in the satellites. Moreover, from their distribution, two major observations can be made: First, the distribution becomes broader with the length of the DNA origami structures. Second, every case follows a cumulative shape distribution.

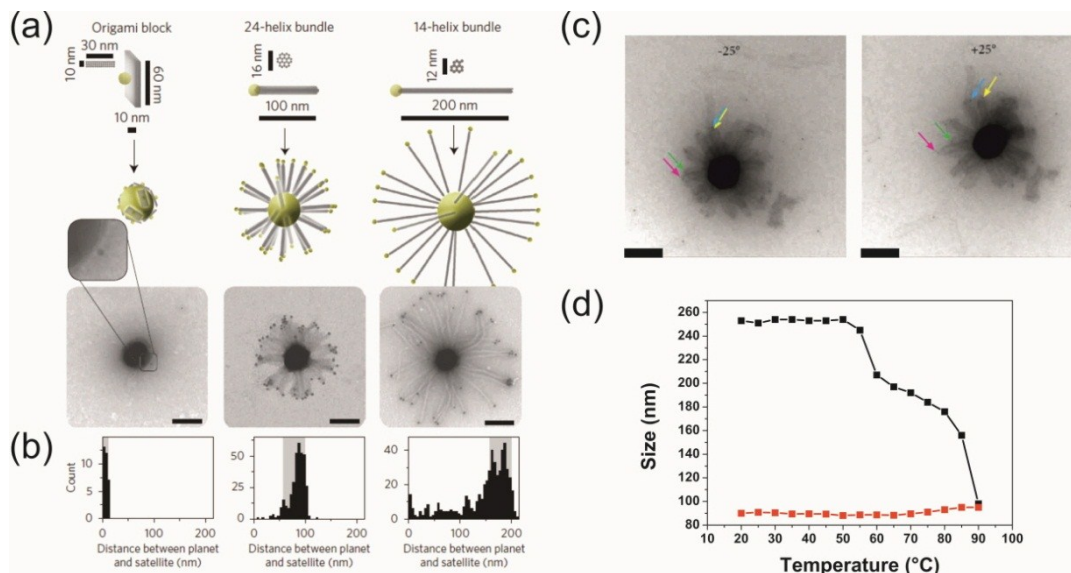


Figure 5.13 (a) Illustration and TEM images of PCNs with different DNA spacers; DNA-block, 24-helix-bundles and 14-helix-bundles. (b) Frequency distribution of distance (surface to surface) between 10 nm and 80 nm gold nanoparticles. (c) Distance between two neighboring 10 nm gold nanoparticles depending on observation angle in TEM image. Arrows point the position of 10 nm gold nanoparticles. Scale bar is 90 nm. (d) Hydrodynamic size of PCNs as function of temperature. Black and red squares represent PSNs and DNA-functionalized 80 nm gold nanoparticles, respectively. (Adapted from [166])

The broadening of inter-particle distance distribution is mainly due the rigidity of DNA origami structures. Since DNA origami structures are made only of soft polymer chains, they have relatively low structural stiffness compared to other rigid materials such as metals [167]. However, this stiffness can be improved by stacking numbers of DNA double helices into bundles, which are used in the our DNA origami structures. Therefore, structural stiffness of DNA origami structures is strongly governed by number of helices. As can be seen in figure 5.13a most 14-

helix-bundles structures in the TEM image are bent due to low structural rigidity, whereas 24-helix-bundles retain their straight morphology. For the same reason, DNA-blocks are more rigid than 24-helix-bundles. Therefore, when the structural stiffness of DNA origami is reduced with number of helices in DNA origami structure, the deviation of inter-particle distance increases.

The cumulative shape distribution can be explained by the collapsing of DNA origami structures onto surface. To determine the interparticle distance, we only rely on two-dimensional observation from TEM image of PSNs. However, in reality, some satellites are attached to the equator of the planet, while others are attached to other areas, including two poles. Here, two poles are positioned on the nominal axis which is perpendicular to the surface of the substrate. Therefore, one pole is positioned closest to the surface and the other is farthest. To gain insight on the three dimensional structure of PSNs, we performed TEM analysis of a sample encapsulated by a thick layer of dried buffer, as shown in figure 5.13c. Within this layer, PSNs are preserved their non-collapsed three-dimensional morphology. It can be seen that the distance between two neighboring nanoparticles are changed with respect to the observation angle. This in turn tells that the nanostructures kept their fully stretched geometry in all directions in solution. The fully stretched size of PSNs can also be determined by hydrodynamic size measurements. It shows that the size of a PSN, consisting of a 60 nm planet and 10 nm satellite gold nanoparticles, has a diameter of 255 nm, which is 25 nm smaller than the size measured by TEM. Taking into account the low density of DNA origami near the boundary of the PSN, a 25 nm smaller hydrodynamic size is a reasonable value. However, when nanostructures were dried on a two-dimensional surface, all satellites collapsed and attached parallel to the surface. Therefore, the satellites initially attached to the planet equator retain the inter-particle distance defined by physical length of the DNA origami structure, while satellites initially attached to the poles locate closer to the planet. Also, a greater number of satellites attached to the equator than to each pole due to the different loading surface area between them. Consequently, more satellites can be observed at the maximum inter-particle distance than are found at the shorter inter-particle distance, which results in cumulative shape distribution of the inter-particle distance.

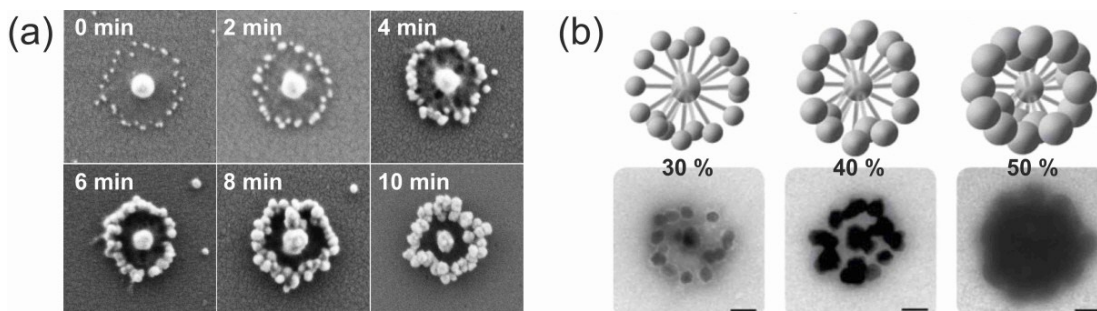
Post-morphological-tuning of PSNs

Figure 5.14 SEM images of gold overgrowth of planet-satellite type structures on a substrate at different deposition time, 0, 2, 4, 6, 8, 10 min. (b) TEM images of silver overgrowth nanostructures in solution at different silver salt concentration 30, 40, 50 %. (Adapted from [166])

The morphology of self-assembled nanostructures can also be tuned with post electroless deposition of metal ions. To perform overgrowth of gold on the gold nanoparticles, a commercially available gold enhancement kit was used. The kit contains gold (III) salt which are further reduced to gold (0) by addition of reducing agent. Figure 5.14a shows TEM images of PSNs with different electroless gold deposition times. The evolution of gold deposition on PSNs can be clearly seen from the size of each gold nanoparticle. After 4 min, most overgrown 10 nm gold nanoparticles are connected to their neighbors and start to form a closed gold ring structure around the planet. After 6 min of gold overgrowth, this gold nanoring is completely closed becomes thicker with further gold overgrowth. Continuous growing of the planet and the surrounding gold ring results in a smaller distance between the two, as can be seen in TEM image of the 10 min gold overgrowth PSN. The metal overgrowth can happen not only on the surface, but also in solution. The overgrowth in solution is performed by mixing a silver enhancement kit with the PSN solution. Depending on overgrowth time and silver salt contents in the solution, the magnitude of silver overgrowth on PSNs can be tuned as shown in figure 5.14b. It is noteworthy that this electroless metal overgrowth can be applied to any PSNs, thus

their optical properties can be easily tuned by choosing different chemical elements and overgrowth times.

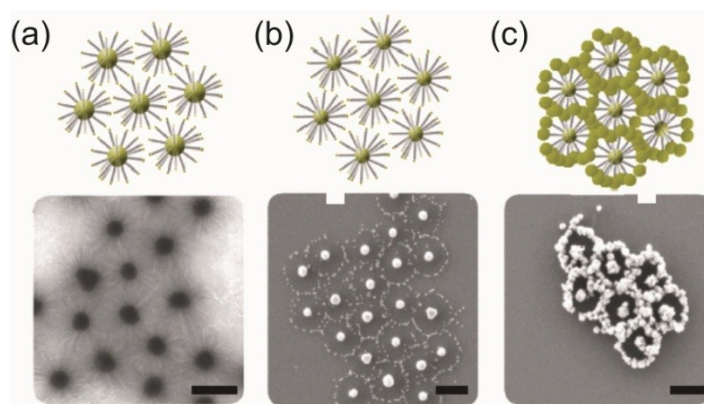


Figure 5.15 Close packed planet-satellite type nanostructures (60 nm AuNP/24 HB@10 nm AuNP) on (a) TEM grid (b) silicon oxide. (c) Gold overgrowth of close packed PSNs on substrate. Scale bars are 200 nm. (Adapted from [166])

PSNs can also self-assemble into highly ordered structures when dried on flat substrates. In figure 5.15, electron microscope images of close-packed lattices of PSNs are shown. Interestingly, nanostructures are in close proximity with small overlapping. A closer look at the high magnification SEM reveals that the measured planet-planet distance is slightly smaller than the expected value due to penetration into neighboring PSNs without sharing satellites. Post-electroless metal deposition was also possible without changing the lattices of the close-packing PSNs, as shown in figure 5.15c.

5.4 Planet-satellite type nanostructures for studying fluorescence quenching, light-harvesting antenna, and signal enhancement of circular dichroism

In following discussion, PSNs were used to study distance-dependent fluorescence quenching, the enhancement of circular dichroism signals and their functionality as light-harvesting antennas.

Distant-dependent fluorescence quenching of Cy5 dyes by gold nanoparticles

Nanostructures consist of 20 nm gold nanoparticles (planet) and 24-helix-bundles functionalized with fluorescent Cy5 dyes (satellites) were used to investigate distance-dependent fluorescence quenching of organic dyes by a gold surface. With the DNA origami technique, it is possible to place dyes at specific locations of the surface of the DNA origami structure via base pairing. 5 different locations were chosen along the direction for the helical axis of 24-helix-bundles at distances of 5, 9, 16, 22, and 58 nm from the gold nanoparticle surface to perform systematic study of distance-dependent quenching, as illustrated in figure 5.16a. Since DNA 24-helix-bundles are rigid enough to sustain their linear morphology, the distance from fluorescent dyes to the gold surface was kept constant. At each distance on a single 24-helix bundle, 4 fluorescence dyes are functionalized. Taking into account number of satellites (3 satellites) in PSNs, each structure contains 12 fluorescence dye molecules. To extract reasonably strong signal from sample, fluorescence spectroscopy was performed for a sample in bulk solution. In this study, metal nanoparticles were used as powerful fluorescence energy acceptor due to the fact that they have large absorption cross-section and omnidirectional quenching regardless of the dipole of donor molecules [168,169]. Although bigger gold nanoparticle planets could be loaded with more satellites, 20 nm gold nanoparticles were chosen to minimize electric field enhancements while fluorescence quenching is the dominant effect.

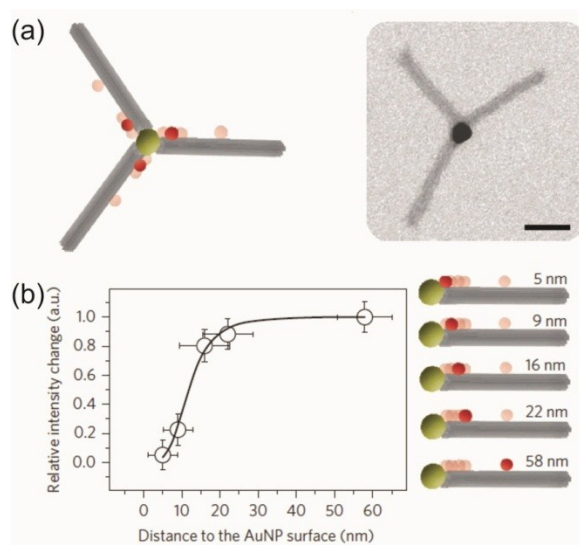


Figure 5.16 (a) Illustration and TEM image of fluorescence quenching ruler PSNs. (b) Plot of relative fluorescence intensity change as function of distance between 20 nm gold planet (colored yellow) and dyes (colored red). (Adapted from [166])

In figure 5.16b relative fluorescence intensities of nanostructures are plotted as function of distance. The relative fluorescence intensities were obtained with respect to a control sample where gold nanoparticle planets were absent. Quenching was observed with small distances between dyes and the gold nanoparticle surface. Fluorescence quenching happened when this distance is less than 22 nm, with no fluorescence quenching at a distance of 58 nm. Relative fluorescence data was fit to a simplified $1/d^4$ model and showed very good agreement with calculated values [170,171]. From this fitting, the averaged distance (d_0) where the energy transfer efficiency is 50% can be found at 12 ± 2 nm.

Light harvesting antenna system

Next the energy absorption of PSNs was studied. Some work has been done on employing spectral ladders of dye molecules on DNA origami structures, but to date, quantum dots have not been studied [172,173]. We prepared PSNs with a quantum

dot planet ($\lambda_{\text{emi}} = 800 \text{ nm}$) and fluorescent Cy3 dyes ($\lambda_{\text{exc}} = 554 \text{ nm}$, $\lambda_{\text{emi}} = 568 \text{ nm}$) as the satellites (functionalized onto the 24-helix-bundles). The details of PSN light-harvesting antenna structures are shown in figure 5.17a. For planet-satellite binding, quantum dots functionalized with both DNA oligos and streptavidin were used. In the case of streptavidin bound PSNs, the closest distance between the quantum dot and fluorescent dye molecules is 7 nm, due to physical size of streptavidin. The quantum dots absorb a wide range of energies in visible wavelength regime and emit at 800 nm. $20\times$ Cy3 dyes are functionalized on the long axis of 24-helix-bundle structures in a straight line to efficiently transfer absorbed energy to the central quantum dot. In these antenna structures, upon initial excitation, absorbed high-energy photons are guided along the dyes. When these photons eventually arrive at the central quantum dot, the energy is emitted as a lower energy photon. Therefore, in principle, the emission intensity of these antenna structures should be bigger than structures without donors. To verify, PSNs without Cy3 were prepared as a control and their fluorescence intensity was compared with the same excitation conditions.

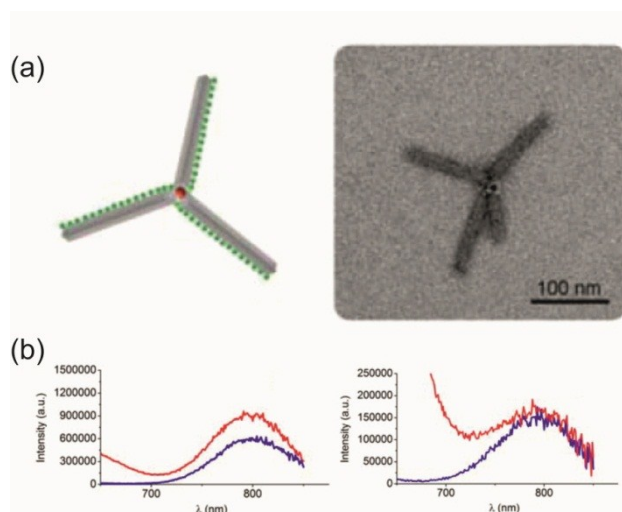


Figure 5.17 (a) Illustration and TEM image of a light-harvesting antenna structure (CdSeTe/24 HB@ $20\times$ Cy3 dyes). (b) Fluorescence intensity of nanostructures with (red solid line) and without (blue solid line) Cy3 dyes on the 24 helix bundles. (left : streptavidin-biotin conjugated, right : DNA oligos conjugated nanostructures) (Adapted from [166])

As shown in figure 5.17b, no notable difference was observed in the fluorescence of the control sample. This ambiguous result can be explained absorption character of quantum dots. Since the absorption spectrum of quantum dots covers almost all visible wavelengths, quantum dots are excited by virtually any visible wavelength. Therefore, the 554 nm excitation, which is used to excite Cy3 dyes in our system, also excites the quantum dots. Moreover, due to the relatively large absorption coefficient of quantum dots compared to Cy3 dyes, the emission of quantum dots makes a bigger contribution to the overall emission intensity. The influence of energy transfer from fluorescence dye to quantum dots is not significant to assure the effect, however, the small increment of fluorescence intensity was observed in most samples. This system can potentially be improved by replacing the fluorescent dye with quantum dots that emit at a shorter wavelength and have a comparable absorption coefficient to the central planet quantum dot.

Signal amplification of circular dichroism activity

Circular dichroism signals (longitudinal or transversal mode) from chiral gold nanohelix satellites can be amplified by adding a planet gold nanoparticle as a electric field enhancer. It has been reported that chiral arrangements of gold nanoparticles in 24-helix-bundles create chiral nanohelices, which actively respond to circularly polarized light [158]. To amplify this response, we introduced an 80 nm gold nanoparticle planet to enhance the electric around the chiral nanohelices. In addition to introducing gold nanoparticle planets, nanostructures bearing chiral nanohelices are overgrown with silver ions in solution to enhance the circular dichroism signal.

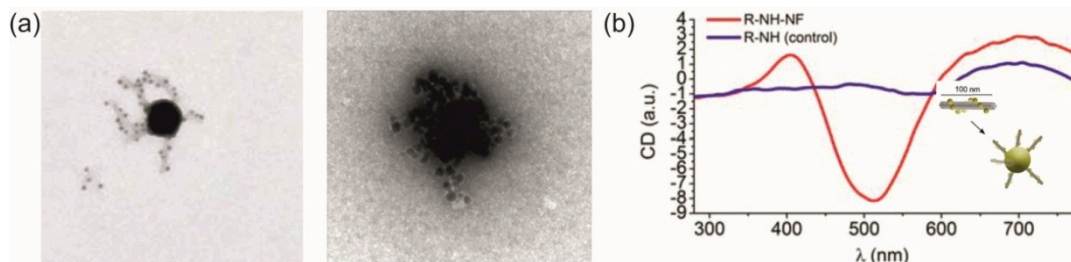


Figure 5.18 (a) TEM images of before and after silver overgrowth of chiral nanostructures (80 nm AuNP/24 HB@9×10 nm AuNPs). (b) Circular dichroism signal of silver overgrowth chiral nanostructures with and without 80 nm gold nanoparticle planet. (inset : illustration of chiral nanostructures) (Adapted from [166])

In figure 5.18 TEM image of a nanostructure before and after the silver overgrowth are shown. The size of individual gold nanoparticles increased, but their spherical morphology remained unchanged. To measure the effect of planet gold nanoparticles in enhancing the circular dichroism signal, a control sample was prepared. It is clearly seen in figure 5.18b that the circular dichroism signal of chiral nanostructures was significantly enhanced by the addition of the gold nanoparticle planet.

5.5 Summary

Planet-satellite type nanostructures are hierarchically assembled with metal nanoparticles, quantum dots, and fluorescent dyes based on the DNA origami technique. This *bottom-up* nanofabrication method enables creating a large number of nanostructures with controllable elemental composition, tunable stoichiometry and inter-elemental distance. First, inter-particle distances between gold nanoparticle planet and gold nanoparticles in satellites were controlled by using DNA origami structures as precise spacers. These DNA origami spacers allowed for the creation of structures up to 500 nm, which was not possible with shorter molecular linkers. Second, the number of satellites in single nanostructure was controlled by employing different sizes of gold nanoparticle planets. The bigger the diameter of the planet gold

nanoparticle, the more satellites were loaded on the planet. A linear dependence between the number of satellites and the diameter of the planet was observed and explained by electrostatic repulsion among the satellites on a planet with low surface curvature. Third, the electroless metal overgrowth was performed on individual PSNs and PSNs in close-packed lattices. This electroless metal overgrowth allowed for tunability in the morphology of PSNs not only on substrate, but also in solution.

The assembled nanostructures also allowed us to study light-matter interactions such as distance-dependent fluorescence quenching as well as PSNs as light-harvesting antenna system and circular dichroism signal enhancers. The modularity of the DNA origami design allowed us to place gold nanoparticles and fluorescent dyes at defined position on DNA origami structures. First, Cy5 dyes were placed on 24 helix bundles with distances of 5, 9, 16, 22, and 58 nm from surface of gold nanoparticle planet to investigate distance-dependent fluorescence quenching. A $1/d^4$ model gave good agreement with calculated values. Second, nanostructures were used as light-harvesting antenna structures by having fluorescent dyes and quantum dots as donors and acceptors, respectively. However, due to a large difference in the absorption coefficients of the donor and acceptor, the results were ambiguous. Employing quantum dots as donors instead of organic dyes can potentially improve this system by matching the absorption coefficients. Third, the intensity of circular dichroism signals from chiral nanohelices was amplified through a strong electric field from large gold nanoparticle planets.

6. Deposition of planet-satellite type nanostructures using focused laser beam

In this chapter a hybrid nanofabrication technique called *soft-optical deposition* will be discussed. This technique combines DNA origami with a tightly focused laser. Using the *bottom-up* DNA origami technique, planet-satellite type nanostructures (PSNs) with complex three-dimensional morphology are assembled. Prepared individual PSNs are optically trapped by a *top-down* optical tweezer technique and subsequently patterned at desired locations on a polymer functionalized substrate. PSN attain structural complexity from two distinct processes: the DNA origami technique (*bottom-up*) and the optical deposition technique (*top-down*). Incident laser powers ranging from 68 to 200 mW are experimentally determined to allow for manipulation of PSNs without deforming their morphology. The same principle was applied to different types of PSNs, confirming the versatility of *soft-optical deposition* technique.

6.1 Hybrid top-down/bottom-up nanofabrication approach: toward highly complex architecture

In the field of nanofabrication, *hybrid top-down/bottom-up* approaches have been used to achieve high structural complexity in nanoscale devices [174-176]. The combination of *top-down* and *bottom-up* approaches enables a precise arrangement of the building blocks into highly ordered architectures, which cannot be achieved with solely one approach.

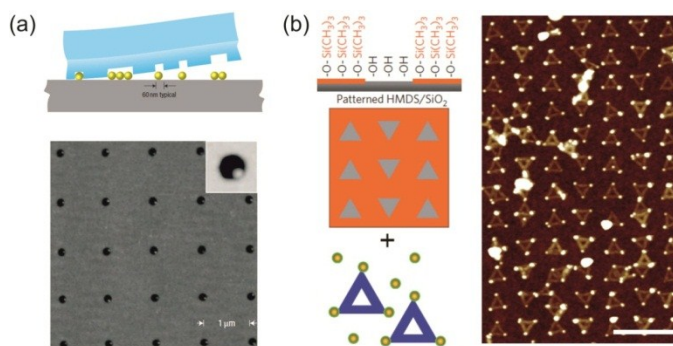


Figure 6.1 (a) PDMS stamp and (b) DNA origami structures assisted gold nanoparticle patterning methods. (Adapted from [177,178])

As an example, figure 6.1a shows spherical gold nanoparticles that were arranged on a flat surface by soft-lithography using a PDMS stamp, a process established by Kraus et al [177]. In their work, spherical gold nanoparticles and PDMS stamps were prepared by colloidal chemistry (*bottom-up*) and electron beam lithography (*top-down*), respectively. Uniformly sized gold nanoparticles assembled into the pre-defined holes on the PDMS stamp and then transferred onto the surface. The resulting patterned gold nanoparticles formed a highly ordered array over a large area. In the work of Hung et al [178], shown in figure 6.1b, gold nanoparticles were first assembled with triangle shaped DNA origami structures, and then integrated into lithographically defined patterns on a substrate. The DNA origami structures contain DNA linkers at each apex and thus DNA functionalized gold nanoparticles could bind with a fixed inter-particle distance. Prepared gold/DNA triangles were self-assembled

to form homogeneous triangular patterns on the substrate where a chemical contrast is given.

Although the above described *hybrid top-down/bottom-up* methods yield highly ordered arrays over a large area, the benefit is rather limited due to low-throughout, expense, and the harsh post chemical process (CHF_3 etching) involved with the electron beam lithography technique.

In this work, we have developed a novel nanofabrication technique called "*soft-optical deposition*", by combining focused laser beam (*top-down*) and DNA origami technique (*bottom-up*). In this hybrid nanofabrication method, complexly shaped planet-satellite type nanostructures (PSNs) were optically trapped and deposited at a desired location on a substrate. The DNA origami technique in this approach allows us to prepare PSNs with widely tunable morphology. Also, the fully solution-based focused laser beam technique enables the manipulation of a single nanoscale object using only a focused laser. With this combination, we have realized convenient manufacturing of highly complex nanostructures without expensive facilities or harsh chemical processes.

6.2 Plasmonic heating of planet-satellite type nanostructures and their thermal stability

Design and preparation of nanoflowers

To demonstrate the *soft-optical deposition* technique, PSNs consisting of a 60 nm spherical gold nanoparticle and multiple DNA-sheets were chosen as a simple model. In this structure, DNA-sheets are prepared by folding long single-stranded scaffold DNA into two-dimensional rectangular objects ($80 \times 80 \times 2$ nm) with help of single stranded DNA staples. Individual DNA-sheets have $15 \times$ DNA linkers (18A) at one

edge, which were used for further hybridization with 24T linkers on the surface of 60 nm gold nanoparticles. These PSNs will hereafter be called "nanoflowers".

Figure 6.2a shows simple schematic illustration of the preparation of nanoflowers. Also, the electron microscope images of each component and the resulting assembled nanoflowers are shown in figure 6.2b. A high magnification SEM image of nanoflowers clearly shows that the surface of individual gold nanoparticles were fully covered with numbers of DNA-sheets. The hydrodynamic size of the nanoflowers was measured as 215 nm with through dynamic light scattering. The distinct morphology of nanoflowers was defined by the sharp edges of DNA-sheets, which constituted a boundary of the structure. Detail design and preparation methods of both DNA functionalized gold nanoparticles and DNA-sheets can be found in Chapter 5.

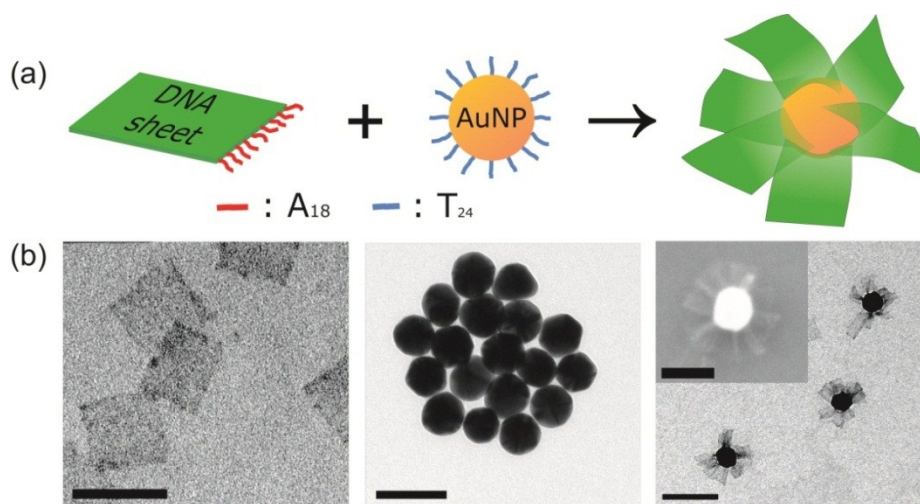


Figure 6.2 (a) Schematic illustration of assembly of nanoflowers. (b) SEM and TEM images of DNA-sheets (left, scale bar: 100 nm), 60 nm gold nanoparticles (middle, scale bar: 100 nm) and nanoflowers (right, scale bar: 200 and). Scale bar in inset image is 100 nm. (Adapted from [179])

Plasmonic heating of nanoflowers

A straightforward nanofabrication method for the deposition of individual nanoflowers is the laser printing method, which was introduced in Chapter 4. The presence of 60 nm plasmonic gold nanoparticles at the center of these structures makes it theoretically feasible that they could be optically printed on a substrate with tightly focused laser. To attain the maximum scattering force for the acceleration of nanoflowers toward a substrate, the complex polarizability of a 60 nm gold nanoparticle needs to be taken into account. In figure 6.3a the calculated real and imaginary part of the polarizability of a 60 nm gold nanoparticle are plotted as a function of wavelength. Since the magnitude of the scattering force increases linearly with the magnitude of the imaginary part of the polarizability, a laser wavelength near 530 nm could provide the strongest scattering force on the 60 nm gold nanoparticles. Moreover, the magnitude of the real part of the polarizability at 530 nm rapidly decreases as the laser wavelength decreases to 530 nm. This, in turn, results in a smaller gradient force, which counter-acts to the scattering force. Therefore, a laser wavelength near 530 nm is ideal for the optical printing of nanoflowers onto a substrate in terms of maximizing the scattering force. It is also possible to determine the optimal wavelength of the printing laser by looking at the extinction cross-section of a 60 nm gold nanoparticle. It can be clearly seen that the peak maximum is located at 530 nm.

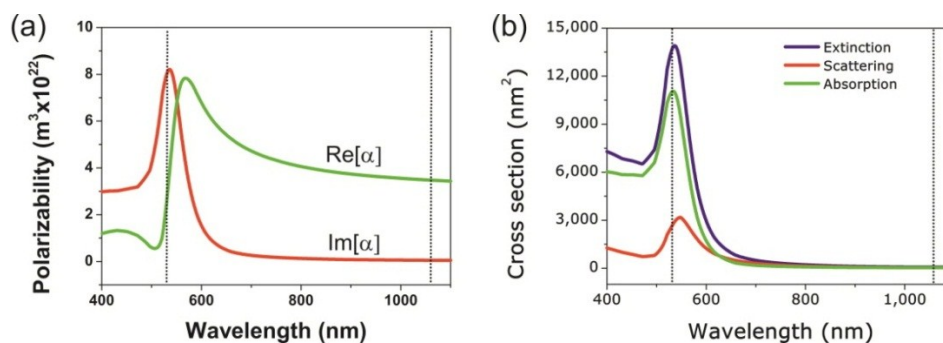


Figure 6.3 (a) Complex polarizability and (b) absorption, scattering, and extinction cross-section of a single 60 nm gold nanoparticle. 532 and 1064 nm laser wavelength is marked with dotted lines.

However, a consequence of using a resonant wavelength laser for optical printing is not only maximizing the printing force but also the increase in temperature of the gold nanoparticle. The large absorption cross-section of a 60 nm gold nanoparticle at 530 nm (figure 6.3b), results in a large amount of plasmonic heating. In the work of Spas et al [140], the authors found that a minimum laser power of 2.5 W was required to optically print an 82 nm gold nanoparticle ($\sigma_{\text{abs}@532\text{nm}} = 1.82 \times 10^{-2} \mu\text{m}^2$). With this power, the gold nanoparticle surface temperature increased to 240 °C. If same laser power and wavelength was applied to a 60 nm gold nanoparticle ($\sigma_{\text{abs}@532\text{nm}} = 1.09 \times 10^{-2} \mu\text{m}^2$), the surface temperature can reach up to 217 °C. At this temperature, spherical gold nanoparticles maintain their morphology since their initial shape is the most energetically stable form. In contrast to gold nanoparticles, however, the double-helical structure of DNA are highly fragile against to the surrounding temperature. The weak thermal tolerance of DNA is owing to the relatively weak hydrogen bonding and base stacking forces which are fundamental for DNA assembly [180,181]. Furthermore, it can be chemically decomposed when exposed to temperatures above 190 °C [182]. Thus it is necessary to investigate the thermal stability of nanoflowers in order to determine the applicability of the laser printing method on such structures containing DNA components.

Melting temperature of nanoflowers

The most widely used value to determine the thermal stability of nano-object containing DNA is the melting temperature. The melting temperatures of both DNA-sheets and nanoflowers are measured with thermal cycler equipped fluorescence spectrometer. In principle, the melting temperature of DNA origami structures can be measured with absorption spectroscopy by monitoring absorbance changes at 260 nm as discussed in Chapter 2. Alternatively, intercalating fluorescent SYBR green dyes can also be employed for this purpose [183]. In solutions containing double-stranded DNA, the SYBR green dyes can be intercalated between two neighboring base pairs. Once intercalated, the intra-molecular transformation of SYBR green dye is restricted

to a planar-form which has higher quantum efficiency (1000 fold) than its free-form. Therefore, denaturing events of the DNA origami structures can be monitored from the fluorescence intensity changes of the SYBR green dye in the sample solution.

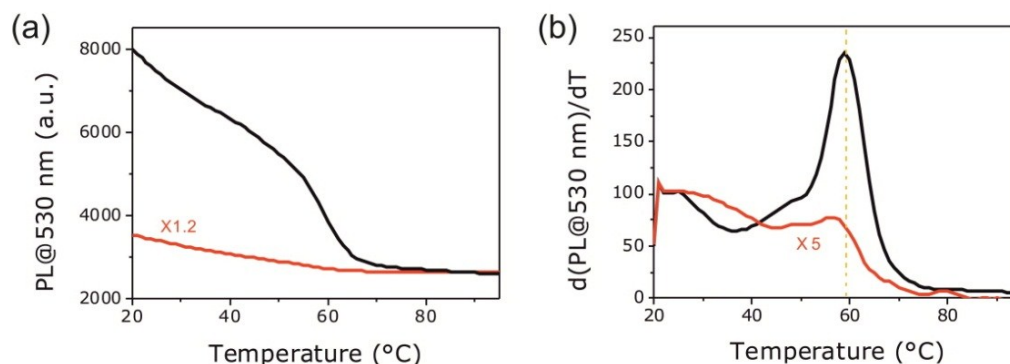


Figure 6.4 The evolution of (a) fluorescence intensity and (b) first derivatives of fluorescence intensity of SYBR green dye in DNA-sheets (black solid line) and nanoflower (red solid line) as a function of temperature. (Adapted from [179])

In figure 6.4a, fluorescence intensity changes of SYBR green dye in solutions of both DNA-sheets and nanoflowers are plotted as a function of temperature. In both samples, fluorescence intensity continuously decreases with increasing temperature from 20 °C to 95 °C. Three different rates of temperature decrease can be found in different temperature regimes: 20–50, 50–70, and 70–95 °C. In the lowest temperature regime, the fluorescence intensity of the sample with DNA-sheets decreases nearly uniformly over the region, which corresponds to the temperature dependent quantum efficiency of the SYBR green dyes (black line). This dependency can be commonly found in most of organic fluorescent dyes due to the promotion of non-radiative decay process at high temperatures [184]. In the mid-temperature regime, a more abrupt fluorescence intensity decrease is seen. This rapid fluorescence intensity change indicates the denaturing of large amount of double-stranded DNA into single-stranded form. Upon this denaturing, intercalated SYBR green dyes were freed and transform their conformation from a planar-form to non-emissive free-form, decreasing the fluorescence intensity. In the highest temperature region above 70 °C, the fluorescence intensity change is relatively small because of the small amount of

remaining restricted-form SYBR green dyes in sample solution. Thus, the temperature dependence of the overall fluorescence change is smallest in this region. Figure 6.4b shows the first derivatives of fluorescence intensity of SYBR green dyes and further illustrates the description above. Moreover, the melting temperature peak of DNA origami sheets can be clearly identified at around 60 °C, which agrees with the previously reported melting temperature of differently shaped DNA origami structures [120]. The melting temperature of nanoflowers was also measured with same principle (red line). Although it shows lower fluorescence intensity over the whole temperature region due to the fluorescence quenching by the gold nanoparticles [169], the obtained melting temperature is in a good agreement with DNA-sheets.

The determined melting temperature of DNA-sheets implies that there is laser power limit, above which optical printing of nanoflowers is not possible. Even with minimum printing laser (532 nm) power of 2.5 mW, the calculated surface temperature (217 °C) of gold nanoparticles exceeds the melting temperature of DNA origami sheets (60 °C). Therefore, it was necessary to consider an alternative wavelength that could minimize plasmonic heating.

Soft-optical deposition technique

In theory, the laser induced surface temperature of gold nanoparticles increases linearly with the applied laser power. This is proportional to the absorption cross-section of the nanoparticle at that wavelength. In near infrared (NIR) region, the absorption cross section of a spherical 60 nm gold nanoparticle is significantly smaller than at 532 nm as shown in 6.3b. For example, at 1064 nm, the absorption cross-section is $4.1 \times 10^{-5} \mu\text{m}^2$, which is 300 times smaller than at 532 nm. Therefore, by using non-resonant wavelength lasers, the surface temperature increase of gold nanoparticles upon absorption can be effectively suppressed below the melting temperature of DNA origami sheets.

However, with a NIR laser, there is also a smaller scattering cross-section, causing gold nanoparticles to be optically trapped rather than printed on surface [185]. Therefore it is necessary to develop new approach to deposit nanoflowers on surfaces in place of the direct optical printing technique. Figure 6.5 shows schematic illustration of three-step *soft-optical deposition* method, which involves a sequential process of trapping, translation and deposition.

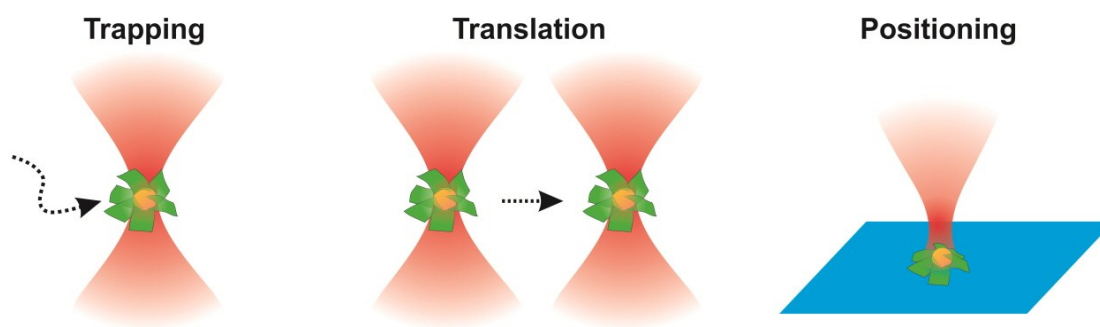


Figure 6.5 Schematic illustration of three step *soft-optical deposition*. (a) Optical trapping, (b) translation, and (c) deposition of nanoflowers. (Adapted from [179])

In the first step of *soft-optical deposition*, individual, randomly diffusing nanoflowers in solution were optically trapped by a non-resonant trapping laser. Once trapped, a nanoflower was translated within the solution and positioned above the desired deposition location. Finally, the nanoflower was lowered to the surface of the substrate and deposited via the electrostatic attraction between the oppositely charged surface and the nanoflower.

6.3 Soft-optical deposition of planet-satellite type nanostructures with focused laser beam

Soft-optical deposition setup

To demonstrate above *soft-optical deposition* technique, conventional DFM was modified by employing a non-resonant 1064 nm cw laser. In figure 6.6a, a schematic illustration of optical trapping DFM setup is shown. The laser was focused on the sample with a 100 \times water immersion objective of high numerical aperture (NA = 1.0). The microscope objective was used not only to tightly focus laser, but also to collect scattered light for imaging while experiments were performed. For precise control over the deposition locations of nanoflowers, a glass coverslip (0.17 mm) was fixed to nano-precision piezo stage. Figure 6.6b shows a dark field image of nanoflowers on the surface as green scattering spots. Red spots were the result of plasmonic coupling between particles, and were observed rarely due to the thick DNA-sheet shell around the gold nanoparticles.

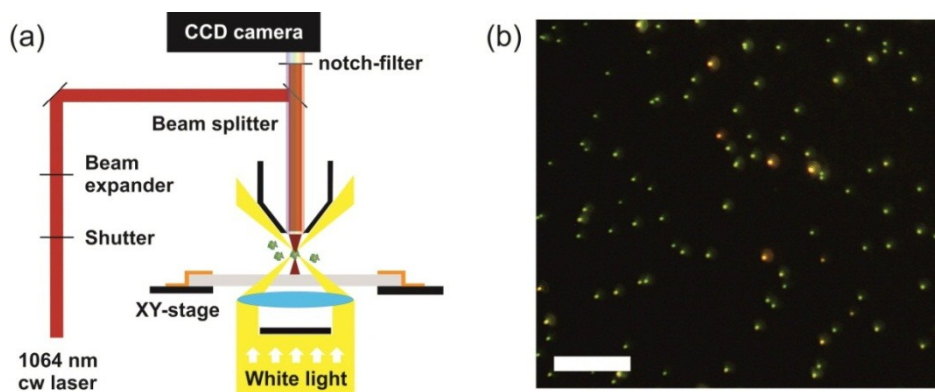


Figure 6.6 Schematic illustration of (a) *soft-optical deposition* setup and (b) dark field microscope image of 60 nm gold nanoparticles on glass substrate. Scale bar is 10 μm .

Optical properties of nanoflowers

The optical forces and plasmonic heating of a spherical gold nanoparticle are closely related to its plasmonic properties. These properties, especially effective cross-sections, can be conveniently calculated from Mie theory as discussed in Chapter 2. Moreover, the calculated properties are in good agreement with experimental results. However, this calculation does not take into account complicated surface conditions (e.g. type and density of surface molecules), which could affect to the plasmonic properties. Therefore, with nanoflowers, it was necessary to investigate the effect of the thick DNA-sheet shell on the plasmonic properties of the gold nanoparticles. To investigate this effect, an UV-Vis spectrometer was used to measure the extinction cross-sections of various types of gold nanoparticles colloids functionalized with different surface molecules. In figure 6.7b, the extinction spectrum of 60 nm gold nanoparticles functionalized with citrate, 24T DNA oligos, and DNA origami sheets in $0.5\times$ TBE buffer solution are plotted.

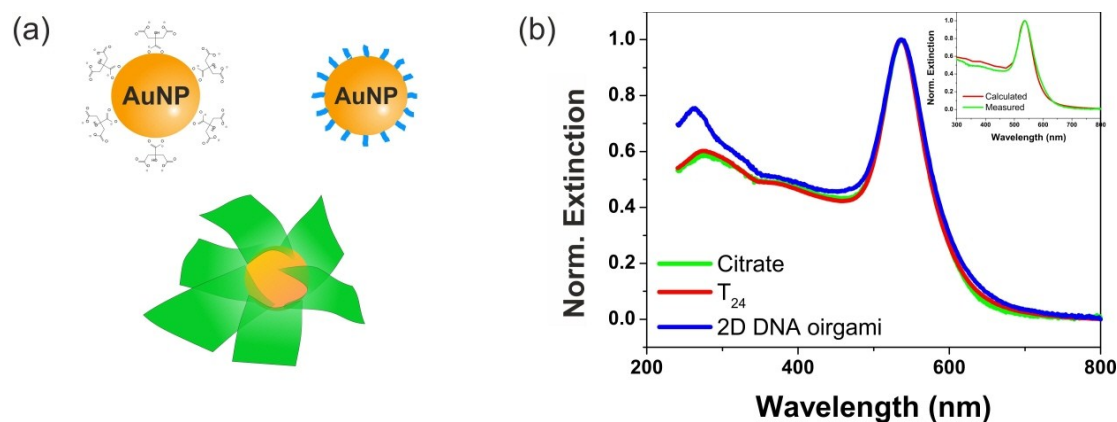


Figure 6.7 (a) Illustration of gold nanoparticles functionalized with citrate, 24T DNA oligos, and 2D DNA sheets on surface. (b) Normalized measured extinction spectra of 60 nm gold nanoparticles with different stabilizers on surface. A comparison of the calculated and measured extinction spectra of 60 nm gold nanoparticles are shown in inset.

In contrast to both citrate and 24T stabilized gold nanoparticles, the gold nanoparticles functionalized with DNA-sheets show a strong peak at 260 nm, in the

fingerprint region of DNA molecules. Due to different amounts of DNA loading on gold nanoparticles, this peak is pronounced with the nanoflowers, whereas the 24T and citrate functionalized gold nanoparticles have overlapping spectra. Regardless of type of surface molecules, a plasmon resonance peak of 60 nm gold nanoparticles appears at 540 nm. In general, the plasmonic peaks of gold nanoparticles are highly sensitive to the refractive index of the surrounding media. In nanoflowers, although DNA was highly packed onto the surface of the gold nanoparticles, water molecules dominantly make up the surrounding media. Due to negligible influence of DNA on plasmonic properties of gold nanoparticles, all the following calculations (optical force, plasmonic heating, etc) were done by considering nanoflowers as bare 60 nm gold nanoparticles. For completeness, the calculated and measured extinction spectra are superimposed in the inset image of figure 6.7b. It can be clearly seen that the experimental measurement agrees with the theoretically calculated spectrum. It is also noteworthy that there was no peak broadening observed between gold nanoparticles with different surface molecules, indicating the high colloidal stability of nanoflower structures in buffer solution. The stability of nanoflowers can be attributed to the thick negatively charged DNA-sheets ($\xi = -14$ mV) that surround the gold nanoparticles.

Soft-optical deposition of nanoflowers on a charged substrate

Nanoflower solutions were prepared with various concentrations from a few pM to tens of pM. Despite the extremely low concentration, the density of particles in solution was too high to achieve single particle trapping for the *soft-optical deposition* process. To avoid multiple nanoparticle trapping, stock solution was diluted to 0.45 pM by adding 0.5× TBE buffer containing 11 mM MgCl₂. To re-disperse nanoflowers after flocculation in long-term storage, diluted nanoflowers were sonicated for 10s and drop cast on an ultra-clean glass coverslip.

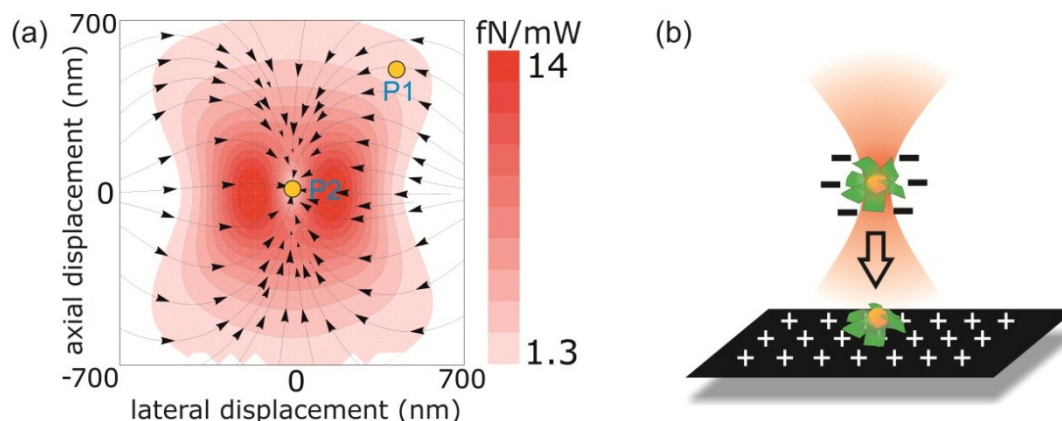


Figure 6.8 (a) Optical forces distribution near laser focus (b) schematic sketch of electrostatic attraction between nanoflowers and polymer layer.

Figure 6.8a shows the calculated magnitude and direction of total optical forces in a cross-section of the laser focus along the laser beam propagation direction. In the first step of *soft-optical deposition*, a randomly diffusing nanoflower (P1) near the laser focus is pulled by the gradient force to the region of highest intensity (P2). In this region, where all the forces balance, the nanoflower was optically trapped. In this work, nanoflowers were optically trapped with a tightly focused off-resonant 1064 nm laser. Trapped and non-trapped nanoflowers were clearly distinguished by their behavior which was monitored with dark field microscopy in real-time. Non-trapped nanoflowers exhibited randomly diffusing Brownian motion, while optically trapped nanoflowers were identified as a fixed green dot centered in the laser focus.

Optical trapping of nanoflowers was only possible with a trapping laser power larger than a minimum threshold power. Below this threshold, the trapping potential, which is proportional to the laser power, was too weak to overcome the Brownian motion of the nanoflowers, resulting in a highly unstable trap. At fixed temperature (20 °C) and viscosity (water), the threshold laser power was measured to be 68 mW. At this power, reasonably stable optical trapping of nanoflowers can be achieved. Laser powers above 68 mW provided highly stable trapping for several tens of minutes.

Once individual nanoflowers were optically trapped at the laser focus, the substrate was translated along x-y plane by moving a nano-precision stage. At the spot above the desired deposition location, the stage was lifted in the z-direction, bringing the trapped nanoflower towards the surface. Under the stable optical trapping condition, trapped nanoflowers stayed stable at the laser focus even with strong flows generated by rapid stage movement.

As a final step of *soft-optical deposition*, individual trapped nanoflowers were deposited onto the positively charged polymer layer on the glass surface. This layer was prepared by passivating a negatively charged ultra-clean substrate with a positively charged polymer. Optically trapped, negatively-charged nanoflowers were pulled towards the surface via electrostatic attraction to the positive polymer layer. This attraction only happened when a nanoflower was close enough to the surface, since the electrostatic force is inversely proportional to $1/r^2$, where r is distance between the nanoflower and the substrate. At a small separation distance, the electrostatic attraction force overcomes the optical trapping potential, and nanoflowers were deposited on the substrate. Since optical observation could only be made from the top, it was not possible to measure actual distance between the nanoflower and the substrate during deposition. However, the deposition could be monitored by observing shape changes of the particle spot before and after deposition. The shape of the diffraction-limited nanoflower scattering spot changed from a filled circle to an empty circle when the nanoflower moved out of focus and onto the substrate. Additionally, the observation of Brownian motion could also be used for the determination of deposition event. Optically trapped nanoflowers showed a small amount of Brownian motion in the laser focus, while deposited nanoflowers were completely fixed.

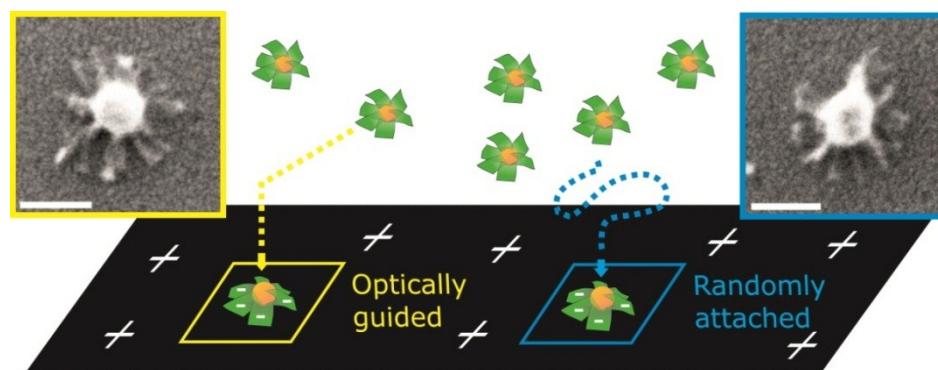


Figure 6.9 SEM images and schematic illustration of attached nanoflowers on surface by *soft-optical deposition* (inside yellow square) and non-specific binding (inside blue square). (Adapted from [179])

Due to the opposite charges of the nanoflowers and the substrate, non-specifically attached nanoflowers could also be found on the substrate. When randomly diffusing nanoflowers came close to surface, they were attracted and could be attached to the polymer layer without the help of the laser. Therefore, in principle, non-specifically attached nanoflowers would retain their morphology perfectly after attachment. Thus, these non-specifically bound nanoflowers could be used as a control for studying the validity of *soft-optical deposition* method. In figure 6.9 SEM images of two different nanoflowers are compared: one was deposited by *soft-optical deposition* and the other attached non-specifically. Here, a minimum trapping laser power of 68 mW was used for *soft-optical deposition*. From the SEM image, the morphology of the nanoflower is clearly identified as a spherical gold nanoparticle and surrounding rectangular DNA-origami-sheets. The sharp edges of the structure boundary were preserved, which is distinct morphology feature of DNA-sheets. This in turn indicates that there was no DNA denaturing occurring due to plasmonic heating during the *soft-optical deposition* process. Compared with the randomly deposited nanoflower, no noticeable morphological differences can be observed. This result shows the validity of this method for depositing nanoflowers with 1064 nm trapping laser at 68 mW. However, at this trapping laser power, trapped nanoflowers often escaped from the laser focus upon translation due to the relatively weak gradient force of 14 fN. Therefore, it was necessary to investigate applicability of this technique with larger trapping laser

powers that ultimately provide higher trapping stability during the *soft-optical deposition* process.

6.4 Effect of laser power on the morphology of planet-satellite type nanostructures

Determination of a non-destructive laser power range

For a systematic study, the surface temperature of a nanoflower was calculated first at laser powers varying from 68 mW to 493 mW. Finite element method software (COMSOL) was used to calculate the steady state heat distribution on a nanoflower surface. The volumetric heat generation Q (W/m^3) factor for the temperature calculation was obtained from the measured laser power and the absorption cross-section of a nanoflower as described in Chapter 2. Figure 6.10 shows a plot of the calculated surface temperature of a nanoflower as a function of the laser power.

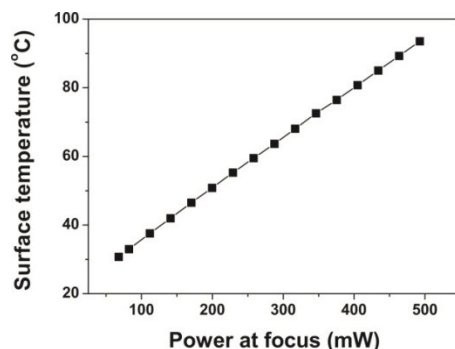


Figure 6.10 Calculated surface temperature of nanoflowers as a function of laser power (NA = 1.0) at focus. (Adapted from [179])

The calculated temperatures on the gold nanoparticle surface increases linearly with the laser power. At 68 mW, the calculated temperature was 31 °C, which is well below the melting temperature of DNA-sheets. Further increasing the laser power to

255 mW, resulted in a calculated surface temperature of 60 °C, which is near the melting temperature of DNA-sheets. At the maximum laser power of 493 mW, the calculated surface temperature exceeded the melting temperature of DNA-sheets at 95 °C. To prove the validity of above calculation, we performed *soft-optical deposition* technique experimentally with laser powers of 68, 112, 200, 229, 288, and 493 mW. For each laser power, the calculated surface temperature of a nanoflower was 31, 38, 51, 56, 65, and 95 °C, respectively. In order to keep all other conditions constant, goldwings were taken from same batch and were deposited on the substrate within a small region ($10\ \mu\text{m}\times 10\ \mu\text{m}$).

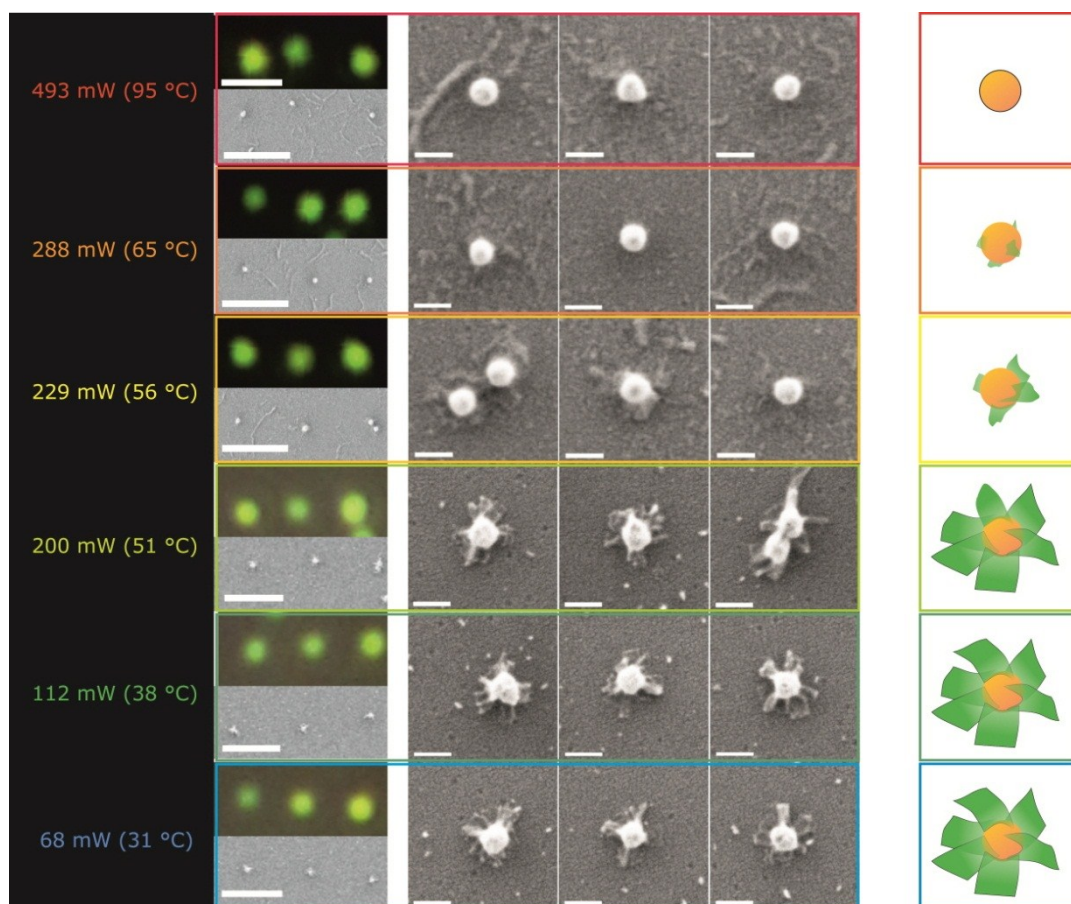


Figure 6.11 (a) Optical trapping laser power and corresponding calculated temperature at the surface of the 60 nm gold nanoparticle. (b) Dark field microscope and SEM image of surface attached nanoflowers at different laser power. (c) Illustrated morphology of nanoflowers upon plasmonic heating. Scale bar is 1 μm and 100 nm, respectively. (Adapted from [179])

In figure 6.11 shows dark field microscope images, SEM images and illustrations of nanoflower deposited with different laser powers (with calculated temperatures). In the low laser power regime, between 68 and 112 mW, no morphological changes were observed in the nanoflower structure. With increasing laser power, however, drastic morphological changes were observed. In each deposition, the average plasmonic heating time was 10 seconds. During this time, DNA-sheets were exposed to an elevated temperature induced by the optically heated gold nanoparticle. If this temperature was above the melting temperature of DNA-sheets, a morphological change must be observed due to DNA denaturing [180].

In the highest laser power regime, between 288 and 493 mW, an extremely small amount of DNA-sheets were found on the gold nanoparticle surface (or none at all). In this region, the surface temperature reached 65 to 95 °C and thermally induced dehybridization of the DNA-origami-sheets was taking place. Interestingly, in the intermediate laser power region, a rapid morphological transition can be observed. At a laser power of 200 mW, relatively well preserved DNA-origami-sheets were observed. However, increasing the laser power to 230 mW changed the morphology of nanoflowers drastically. Many DNA-sheets were completely detached, leaving behind a bare surface on the gold nanoparticle. Some remaining DNA-sheets were found, however, they were severely damaged and sharp edges could no longer be identified. The calculated surface temperature where this change took place was between 51 and 56 °C. The observed melting temperature was a few degrees lower than the measured melting temperature (60 °C) of DNA-sheets by using SYBR green dyes. This small difference can be explained by looking into the evolution of the first derivatives of fluorescence intensity as shown in figure 6.4b. It can be seen that the dehybridization of double-stranded DNA starts at 55 °C. At this temperature, shorter DNA staples were dehybridized from the scaffold DNA due to their relatively lower binding energy, while longer ones remain. The shortest DNA staples in DNA-sheets are DNA linkers (18T), which were located closest to gold nanoparticle surface, where the temperature was highest. Furthermore, unlike melting temperature experiments for bulk materials, optically heated nanoflowers generated a strong

temperature gradient around gold nanoparticle. Considering these facts, the small difference in the measured melting temperature is justified.

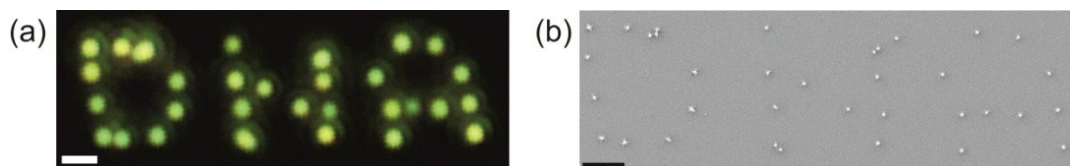


Figure 6.12 Dark field microscope and SEM image of DNA pattern consisting of individual nanoflowers. Pattern created by using 114 mW 1064 nm cw laser. Scale bars are 1 μm . (Adapted from [179])

The systematic study of how the morphology of nanoflowers was influenced by laser power allowed us to find a realistic trapping laser power range between 68 and 200 mW. With a fixed microscope objective and trapping laser wavelength, individual nanoflowers can be optically deposited at a desired location onto the substrate without deformation of their morphology. To demonstrate nanofabrication by using the *soft-optical deposition* technique, a series of nanoflower depositions was conducted to spell out “DNA”. Figure 6.12 shows dark field microscope and SEM images of the “DNA” pattern consisting of individual nanoflowers with an interparticle distance of 700 nm (using 114 mW trapping laser). Although small numbers of multimers were found, all the nanoflowers were deposited at the desired location and their distinct morphology was preserved during this process. The interparticle distance could potentially be reduced since this technique does not generate strong flows or thermal energy near the overheated gold nanoparticles, which was a major limiting factor in a previously reported laser printing technique [140].

Validity of soft-optical deposition technique to PSNs

To prove the versatility of the *soft-optical deposition* method, we performed temperature resistance experiments with another type of PSN. Here, the PSNs

consisted of 10 nm gold nanoparticle satellites and 60 nm gold nanoparticle planets with an inter-element distance of 100 nm, given by length of 24-helix-bundles.

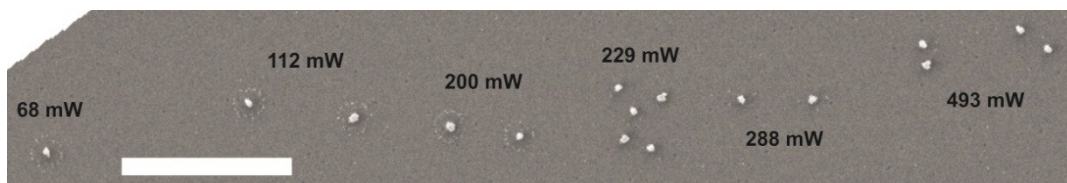


Figure 6.13 SEM image of planet-satellites structure deposited by *soft-optical deposition* methods at different laser powers. Scale bar is 1 μm .

In figure 6.13, SEM images of deposited PSNs with different trapping laser powers are shown. In contrast to nanoflowers, their morphology was defined by 10 nm gold nanoparticles, which constitute boundary of structure. Therefore, morphological changes from plasmonic heating can be determined simply by checking for existence of surrounding gold satellites after deposition. Here, we observed the same tendency as in the case of the nanoflowers. With tapping laser power below 200 mW, a beaded ring consisting of 10 nm gold nanoparticles could be clearly observed after *soft-optical deposition*, while higher laser powers (> 200 mW) resulted in dehybridization of satellites from the surface of planet gold nanoparticles.

6.5 Summary

The *Soft-optical deposition* technique and its validity in relation to trapping laser power on 60 nm gold bearing planet-satellite type nanostructure (PSNs) has been discussed. In this study, PSNs were prepared by self-assembly of 60 nm gold nanoparticles and two dimensional DNA origami sheets as planets and satellites, respectively. Prepared PSNs were optically trapped with a tightly focused, off-resonant NIR laser to minimize plasmonic heating effects. Stable trapping enabled manipulation of individual PSNs in solution and finally deposition on oppositely charged glass substrates without notable thermal damage on their morphology. We

have found a realistic trapping laser power range (68~200 mW, NA=1.0) that can be used for stable and non-destructive optical deposition of PSNs on a substrate. An array of PSNs were also patterned on a substrate with an inter-particle distance of 700 nm, granting dual structural complexity in the final structure.

7. Conclusion and outlook

In this thesis, I investigated various fabrication methods for the control of nanoscopic spatial arrangement of metal nanoparticles on a substrate. The methods were realized by utilizing two techniques: a *tightly focused laser* and the *DNA origami technique*. First, a *tightly focused laser* was used to hold or push individual colloidal metal nanoparticles and to ultimately print them at desired locations on substrates with a printing precision within a few tens of nanometers. By employing two independent laser wavelengths, this method allowed the all-optical control of angular orientation of printed gold nanorods. The method was also applied to a silicon nitride membrane to conveniently fabricate photonic crystal nanocavities containing plasmonic structures in their sub-micron physical defect. Precise spatial arrangement of metal nanoparticles into planet-satellite like nanostructure was possible by using the *DNA origami nanostructures* with well-defined size and shape. The hierarchical assembly approach of the method enabled controlling the composition, inter-particle distance, and stoichiometry between planets and satellites metal nanoparticles. Finally, the combination of tightly focused laser and DNA origami technique allowed the non-destructive deposition of thermally fragile planet-satellite type nanostructures on desired locations without morphological changes. The resulting patterned nanostructures had highly complex morphology which cannot be obtained by using individually one of the nanofabrication methods. The detailed findings and the outlook of this thesis are described below and categorized them into three different nanofabrication approaches: *top-down*, *bottom-up* and *hybrid top-down/bottom-up*.

In the first part of the *top-down* approach, I optically printed individual gold nanorods with control over their location and angular orientation on a substrate by using two independent laser wavelengths. Gold nanorods were functionalized with polyethylene glycol (PEG), thus non-specific binding between a bare glass substrate and the gold nanorods was effectively avoided. A trapping laser whose wavelength is off-resonant with both transverse and longitudinal plasmon modes of the gold nanorods was used to trap and simultaneously align individual gold nanorods at laser focus. By addition

of a resonant wavelength printing laser, pre-aligned gold nanorods were optically printed on a substrate while their angular orientation was maintained. The effect of relative alignments and laser powers of the two lasers on the angular printing precision were studied. The best controls of spatial location (ca. 50 nm) and angular printing precision (± 16 degrees) were achieved with perpendicularly aligned two lasers with laser powers of 27 and 8.3 mW for trapping and printing lasers, respectively. The two-color laser printing technique can be potentially useful for applications where controlling the orientation of gold nanorods is of interest. If two gold nanorods are printed in a tip-to-tip fashion in close proximity to each other, the resulting strong electric field enhancement could be used for the sensing small contents of molecules in surrounding environment. Furthermore, parallelization of this technique can be achieved by introducing a spatial light modulator which provides multiple identical beams with arbitrary arrangements.

In the second part of the *top-down* approach, I optically printed single gold nanoparticle onto a defect of a silicon nitride (Si_xN_y) photonic crystal nanocavity (PCN). By employing a focused near infrared wavelength laser, 150 nm spherical colloidal gold nanoparticles were deposited without destructing the morphology of both gold nanoparticles and silicon nitride PCNs. This method allowed fast and convenient printing of gold nanoparticles onto the PCNs with the precision of 50 nm. The gold nanoparticle containing Si_xN_y PCNs showed broadening and damping of their fundamental cavity mode regardless of the precise location of the gold nanoparticle within the defect-site. The finite-differential time-domain modeling of our system showed that there is qualitatively agreement between the experimental observation and the optical modeling. Further FDTD calculations revealed that the partially dissipated energy in fundamental cavity mode is used to excite plasmon mode of the gold nanoparticles. It was also predicted that this interaction can be maximized when the energy level of both plasmon and cavity mode are matched. This technique provides a novel all-optical based method for the routine fabrication of a photonic crystal nanocavity containing optically-printed nano-objects. It is foreseen that with this technique not only to gold nanoparticles but also quantum emitters, such as quantum dots or nitrogen-vacancy nanodiamonds can be potentially

used. Furthermore, a new type of low-threshold photonic crystal nanocavity laser may be possible by printing core-shell metal nanoparticle onto the cavity defect. In such hybrid laser, a strong electric field near metal nanoparticle could amplify the excitation rate of fluorescent dyes in the shell, thus lowering the threshold for the laser can be envisaged.

In the *bottom-up* approach, metal nanoparticles were spatially arranged into planet-satellite like nanostructures by using state-of-the-art DNA origami technique. By using DNA origami structures with well-defined size and shape as spacers, smaller metal nanoparticles were organized in orbit around larger metal nanoparticle which serves as a solid base. The hierarchical assembly approach of this technique allowed us to create such planet-satellite type nanostructures with tunable composition, inter-particle distance and stoichiometry between planet and satellites. Quantum dots and organic fluorescence dyes were also used instead of metal nanoparticles, thereby created hetero-nanostructures for fundamental studies, such as distance dependent quenching of fluorescence dye by gold nanoparticles, light harvesting antenna structure and amplification of circular dichroism response. The planet-satellite type nanostructure could potentially be used for building metamaterials by self-assembling them into highly ordered plasmonic arrays. Also, due to the structural symmetry of these nanostructures, they may be used as plasmon-based nanolenses or for surface plasmon amplification by stimulated emission of radiation (SPASERs) applications. The tunable inter-particle distance in planet-satellite type nanostructures may also allow the study of distance dependent electric field enhancement of plasmonically coupled nanoparticles.

In the *hybrid top-down/bottom-up* approach, I optically trapped and subsequently deposited planet-satellite type nanostructures at a desired location on a substrate without deforming their morphology. An off-resonance laser was not only used to optically manipulate individual PSNs but also to minimize thermal denaturing of DNAs induced by plasmonically heated metal nanoparticles. The PSNs consist of 60 nm gold nanoparticles (planet) and multiple two dimensional DNA origami sheets (satellites) were optically deposited in different trapping laser power in order to

determine an applicable trapping laser power range. With laser powers between 68 and 200 mW, non-destructive optical deposition of PSNs was possible while their morphology was kept unchanged even after deposition. This laser power range was applied to different type of PSNs and thereby verified the versatility of this technique for the optical deposition of such PSNs containing an optically trappable planet component. This hybrid nanofabrication technique can potentially be used where a higher degree of structural complexity is demanded. By utilizing both top-down and bottom-up nano-scale arrangement techniques, the dual structural complexity could be achieved, one given by self-assembly DNA origami technique and the other by optical deposition technique. It is also envisaged that the thermal tolerance of PSNs can be increased by using intercalating molecules as cross-linkers, such as 8-methoxypsoralen (MOP). MOP creates covalent bonds between complementary base pairs and thus increasing the thermal tolerance of DNA origami structure is envisioned.

References

- 1 Feynman, R. P. There's plenty of room at the bottom. *Engineering and Science* **23**, 22-36, (1960).
- 2 Sun, Y. G. & Xia, Y. N. Shape-controlled synthesis of gold and silver nanoparticles. *Science* **298**, 2176-2179, (2002).
- 3 Grzelczak, M., Perez-Juste, J., Mulvaney, P. & Liz-Marzan, L. M. Shape control in gold nanoparticle synthesis. *Chemical Society Reviews* **37**, 1783-1791, (2008).
- 4 Xia, Y. N., Yang, P. D., Sun, Y. G., Wu, Y. Y., Mayers, B., Gates, B., Yin, Y. D., Kim, F. & Yan, Y. Q. One-dimensional nanostructures: Synthesis, characterization, and applications. *Advanced Materials* **15**, 353-389, (2003).
- 5 Shao, Y., Jin, Y. D. & Dong, S. J. Synthesis of gold nanoplates by aspartate reduction of gold chloride. *Chemical Communications*, 1104-1105, (2004).
- 6 Sau, T. K. & Murphy, C. J. Room temperature, high-yield synthesis of multiple shapes of gold nanoparticles in aqueous solution. *Journal of the American Chemical Society* **126**, 8648-8649, (2004).
- 7 Jana, N. R., Gearheart, L. & Murphy, C. J. Wet chemical synthesis of high aspect ratio cylindrical gold nanorods. *Journal of Physical Chemistry B* **105**, 4065-4067, (2001).
- 8 Jana, N. R., Gearheart, L. & Murphy, C. J. Wet chemical synthesis of silver nanorods and nanowires of controllable aspect ratio. *Chemical Communications*, 617-618, (2001).
- 9 Jackson, J. B. & Halas, N. J. Silver nanoshells: Variations in morphologies and optical properties. *Journal of Physical Chemistry B* **105**, 2743-2746, (2001).
- 10 Chen, S. H., Wang, Z. L., Ballato, J., Foulger, S. H. & Carroll, D. L. Monopod, bipod, tripod, and tetrapod gold nanocrystals. *Journal of the American Chemical Society* **125**, 16186-16187, (2003).
- 11 Link, S. & El-Sayed, M. A. Spectral properties and relaxation dynamics of surface plasmon electronic oscillations in gold and silver nanodots and nanorods. *Journal of Physical Chemistry B* **103**, 8410-8426, (1999).

- 12 Yang, J., You, J. B., Chen, C. C., Hsu, W. C., Tan, H. R., Zhang, X. W., Hong, Z. R. & Yang, Y. Plasmonic Polymer Tandem Solar Cell. *Acs Nano* **5**, 6210-6217, (2011).
- 13 Kusumi, A., Nakada, C., Ritchie, K., Murase, K., Suzuki, K., Murakoshi, H., Kasai, R. S., Kondo, J. & Fujiwara, T. Paradigm shift of the plasma membrane concept from the two-dimensional continuum fluid to the partitioned fluid: High-speed single-molecule tracking of membrane molecules. *Annual Review of Biophysics and Biomolecular Structure* **34**, 351-354, (2005).
- 14 Raschke, G., Kowarik, S., Franzl, T., Sonnichsen, C., Klar, T. A., Feldmann, J., Nichtl, A. & Kurzinger, K. Biomolecular recognition based on single gold nanoparticle light scattering. *Nano Letters* **3**, 935-938, (2003).
- 15 El-Sayed, I. H., Huang, X. H. & El-Sayed, M. A. Surface plasmon resonance scattering and absorption of anti-EGFR antibody conjugated gold nanoparticles in cancer diagnostics: Applications in oral cancer. *Nano Letters* **5**, 829-834, (2005).
- 16 Sonnichsen, C., Reinhard, B. M., Liphardt, J. & Alivisatos, A. P. A molecular ruler based on plasmon coupling of single gold and silver nanoparticles. *Nature Biotechnology* **23**, 741-745, (2005).
- 17 Lim, D. K., Jeon, K. S., Kim, H. M., Nam, J. M. & Suh, Y. D. Nanogap-engineerable Raman-active nanodumbbells for single-molecule detection. *Nature Materials* **9**, 60-67, (2010).
- 18 Li, Z. Y. & Xia, Y. N. Metal Nanoparticles with Gain toward Single-Molecule Detection by Surface-Enhanced Raman Scattering. *Nano Letters* **10**, 243-249, (2010).
- 19 Dahlin, A., Zach, M., Rindzevicius, T., Kall, M., Sutherland, D. S. & Hook, F. Localized surface plasmon resonance sensing of lipid-membrane-mediated biorecognition events. *Journal of the American Chemical Society* **127**, 5043-5048, (2005).
- 20 Kim, D., Jeong, Y. Y. & Jon, S. A Drug-Loaded Aptamer-Gold Nanoparticle Bioconjugate for Combined CT Imaging and Therapy of Prostate Cancer. *Acs Nano* **4**, 3689-3696, (2010).
- 21 Kennedy, L. C., Bickford, L. R., Lewinski, N. A., Coughlin, A. J., Hu, Y., Day, E. S., West, J. L. & Drezek, R. A. A New Era for Cancer Treatment: Gold-Nanoparticle-Mediated Thermal Therapies. *Small* **7**, 169-183, (2011).

-
- 22 Huang, X. H., El-Sayed, I. H., Qian, W. & El-Sayed, M. A. Cancer cell imaging and photothermal therapy in the near-infrared region by using gold nanorods. *Journal of the American Chemical Society* **128**, 2115-2120, (2006).
- 23 Tseng, A. A. *Nanofabrication: fundamentals and applications*. (World Scientific, 2008).
- 24 Majumder, D. D., Banerjee, R., Ulrichs, C., Mewis, I. & Goswami, A. Nanomaterials: Science of bottom-up and top-down. *Iete Technical Review* **24**, 9-25, (2007).
- 25 Biswas, A., Bayer, I. S., Biris, A. S., Wang, T., Dervishi, E. & Faupel, F. Advances in top-down and bottom-up surface nanofabrication: Techniques, applications & future prospects. *Advances in Colloid and Interface Science* **170**, 2-27, (2012).
- 26 Vieu, C., Carcenac, F., Pepin, A., Chen, Y., Mejias, M., Lebib, A., Manin-Ferlazzo, L., Couraud, L. & Launois, H. Electron beam lithography: resolution limits and applications. *Applied Surface Science* **164**, 111-117, (2000).
- 27 Sundaramurthy, A., Schuck, P. J., Conley, N. R., Fromm, D. P., Kino, G. S. & Moerner, W. E. Toward nanometer-scale optical photolithography: Utilizing the near-field of bowtie optical nanoantennas. *Nano Letters* **6**, 355-360, (2006).
- 28 Mendes, P. M., Jacke, S., Critchley, K., Plaza, J., Chen, Y., Nikitin, K., Palmer, R. E., Preece, J. A., Evans, S. D. & Fitzmaurice, D. Gold nanoparticle patterning of silicon wafers using chemical e-beam lithography. *Langmuir* **20**, 3766-3768, (2004).
- 29 Liu, G. Y., Xu, S. & Qian, Y. L. Nanofabrication of self-assembled monolayers using scanning probe lithography. *Accounts of Chemical Research* **33**, 457-466, (2000).
- 30 Yan, H., Park, S. H., Finkelstein, G., Reif, J. H. & LaBean, T. H. DNA-templated self-assembly of protein arrays and highly conductive nanowires. *Science* **301**, 1882-1884, (2003).
- 31 Wang, Y., Chen, G., Yang, M. X., Silber, G., Xing, S. X., Tan, L. H., Wang, F., Feng, Y. H., Liu, X. G., Li, S. Z. & Chen, H. Y. A systems approach towards the stoichiometry-controlled hetero-assembly of nanoparticles. *Nature Communications* **1**, (2010).
- 32 Lu, W. & Lieber, C. M. Nanoelectronics from the bottom up. *Nature Materials* **6**, 841-850, (2007).

- 33 Li, F., Josephson, D. P. & Stein, A. Colloidal Assembly: The Road from Particles to Colloidal Molecules and Crystals. *Angewandte Chemie-International Edition* **50**, 360-388, (2011).
- 34 Hoepfner, S., Maoz, R., Cohen, S. R., Chi, L. F., Fuchs, H. & Sagiv, J. Metal nanoparticles, nanowires, and contact electrodes self-assembled on patterned monolayer templates - A bottom-up chemical approach. *Advanced Materials* **14**, 1036, (2002).
- 35 Urban, A. S., Lutich, A. A., Stefani, F. D. & Feldmann, J. Laser Printing Single Gold Nanoparticles. *Nano Letters* **10**, 4794-4798, (2010).
- 36 Guffey, M. J. & Scherer, N. F. All-Optical Patterning of Au Nanoparticles on Surfaces Using Optical Traps. *Nano Letters* **10**, 4302-4308, (2010).
- 37 Rothemund, P. W. K. Folding DNA to create nanoscale shapes and patterns. *Nature* **440**, 297-302, (2006).
- 38 Wagner, F. E., Haslbeck, S., Stievano, L., Calogero, S., Pankhurst, Q. A. & Martinek, P. Before striking gold in gold-ruby glass. *Nature* **407**, 691-692, (2000).
- 39 Leonhardt, U. Optical metamaterials - Invisibility cup. *Nature Photonics* **1**, 207-208, (2007).
- 40 Weyl, W. A. *Coloured Glasses*. 380-400 (Society of Glass Technology, 1951).
- 41 Dykman, L. A. & Khlebtsov, N. G. Gold Nanoparticles in Biology and Medicine: Recent Advances and Prospects. *Acta Naturae* **3**, 34-55, (2011).
- 42 Faraday, M. Experimental Relations of Gold (and Other Metals) to Light. *Philosophical Transactions of the Royal Society of London* **147**, (1857).
- 43 Turkevich, J., Stevenson, P. C. & Hillier, J. A Study of the Nucleation and Growth Processes in the Synthesis of Colloidal Gold. *Discussions of the Faraday Society*, 55, (1951).
- 44 Zsigmondy, R. (Nobel Foundation, 1926).
- 45 Mie, G. Beiträge zur Optik trüber Medien, speziell kolloidaler Metallösungen. *Annalen der Physik* **330**, 337-445, (1908).
- 46 Tylecote, R. F. *A history of metallurgy*. (The Metals Society, 1976).
- 47 Ashcroft, N. W. & Mermin, N. D. *Solid state physics*. (Harcourt, 1976).
- 48 Maxwell, J. C. A dynamical theory of the electromagnetic field. *Philosophical Transactions of the Royal Society of London* **155**, 459-512, (1865).
- 49 Drude, P. Zur Elektronentheorie der metalle. *Annalen der Physik* **306**, 566-613, (1900).

- 50 Drude, P. Zur Elektronentheorie der Metalle; II. Teil. Galvanomagnetische und thermomagnetische Effecte. *Annalen der Physik* **308**, 369-402, (1900).
- 51 Sommerfeld, A. & Bethe, H. *Elektronentheorie der Metalle*. (Springer Verlag, 1933).
- 52 Zeman, E. J. & Schatz, G. C. An Accurate Electromagnetic Theory Study of Surface Enhancement Factors for Ag, Au, Cu, Li, Na, Al, Ga, in, Zn, and Cd. *Journal of Physical Chemistry* **91**, 634-643, (1987).
- 53 Ordal, M. A., Bell, R. J., Alexander, J., R. W., Long, L. L. & Querry, M. R. Optical properties of fourteen metals in the infrared and far infrared: Al, Co, Cu, Au, Fe, Pb, Mo, Ni, Pd, Pt, Ag, Ti, V, and W. *Applied Optics* **24**, 4493-4499, (1985).
- 54 Maier, S. A. *Plasmonics: Fundamentals and Applications*. (Springer, 2007).
- 55 Johnson, P. B. & Christy, R. W. Optical constants of noble metals. *Physical Review B* **6**, 4370-4379, (1972).
- 56 Kopitzki, K. & Herzog, P. *Einführung in die Festkörperphysik*. (Springer DE, 2007).
- 57 Kreibig, U. & Vollmer, M. *Optical properties of metal clusters*. (Springer, 1995).
- 58 Griffiths, D. J. *Introduction to Electrodynamics*. (Addison Wesley, 2012).
- 59 Sonnichsen, C., Franzl, T., Wilk, T., von Plessen, G., Feldmann, J., Wilson, O. & Mulvaney, P. Drastic reduction of plasmon damping in gold nanorods. *Physical Review Letters* **88**, (2002).
- 60 Myroshnychenko, V., Rodriguez-Fernandez, J., Pastoriza-Santos, I., Funston, A. M., Novo, C., Mulvaney, P., Liz-Marzan, L. M. & de Abajo, F. J. G. Modelling the optical response of gold nanoparticles. *Chemical Society Reviews* **37**, 1792-1805, (2008).
- 61 Kuwata, H., Tamaru, H., Esumi, K. & Miyano, K. Resonant light scattering from metal nanoparticles: Practical analysis beyond Rayleigh approximation. *Applied Physics Letters* **83**, 4625-4627, (2003).
- 62 Molloy, J. E. & Padgett, M. J. Lights, action: optical tweezers. *Contemporary Physics* **43**, 241-258, (2002).
- 63 Ashkin, A. & Dziedzic, J. M. Optical Trapping and Manipulation of Viruses and Bacteria. *Science* **235**, 1517-1520, (1987).
- 64 Ashkin, A., Dziedzic, J. M., Bjorkholm, J. E. & Chu, S. Observation of a Single-Beam Gradient Force Optical Trap for Dielectric Particles. *Optics Letters* **11**, 288-290, (1986).

- 65 Ashkin, A. Acceleration and Trapping of Particles by Radiation Pressure. *Physical Review Letters* **24**, 156, (1970).
- 66 Darrigol, O. *Electrodynamics from Ampère to Einstein*. (Oxford University Press, 2000).
- 67 Agayan, R. R., Gittes, F., Kopelman, R. & Schmidt, C. F. Optical trapping near resonance absorption. *Applied Optics* **41**, 2318-2327, (2002).
- 68 Jin, R. C. Quantum sized, thiolate-protected gold nanoclusters. *Nanoscale* **2**, 343-362, (2010).
- 69 Puech, K., Henari, F. Z., Blau, W. J., Duff, D. & Schmid, G. Investigation of the Ultrafast Dephasing Time of Gold Nanoparticles Using Incoherent-Light. *Chemical Physics Letters* **247**, 13-17, (1995).
- 70 Govorov, A. O. & Richardson, H. H. Generating heat with metal nanoparticles. *Nano Today* **2**, 30-38, (2007).
- 71 Sun, C. K., Vallee, F., Acioli, L. H., Ippen, E. P. & Fujimoto, J. G. Femtosecond-Tunable Measurement of Electron Thermalization in Gold. *Physical Review B* **50**, 15337-15348, (1994).
- 72 Fann, W. S., Storz, R., Tom, H. W. K. & Bokor, J. Electron Thermalization in Gold. *Physical Review B* **46**, 13592-13595, (1992).
- 73 Govorov, A. O., Zhang, W., Skeini, T., Richardson, H., Lee, J. & Kotov, N. A. Gold nanoparticle ensembles as heaters and actuators: melting and collective plasmon resonances. *Nanoscale Research Letters* **1**, 84-90, (2006).
- 74 MQMIE version v. 3.2a (2012).
- 75 Miescher, F. Ueber die chemische Zusammensetzung der Eiterzellen. *Medicinisch-chemische Untersuchungen* **4**, 441-460, (1871).
- 76 Levene, P. The structure of yeast nucleic acid. *The Journal of Biological Chemistry* **40**, 415-424, (1919).
- 77 Hershey, A. D. & Chase, M. Independent Functions of Viral Protein and Nucleic Acid in Growth of Bacteriophage. *Journal of General Physiology* **36**, 39-56, (1952).
- 78 Watson, J. D. & Crick, F. H. C. Molecular Structure of Nucleic Acids - a Structure for Deoxyribose Nucleic Acid. *Nature* **171**, 737-738, (1953).
- 79 Chen, J. H. & Seeman, N. C. Synthesis from DNA of a Molecule with the Connectivity of a Cube. *Nature* **350**, 631-633, (1991).
- 80 Alberts, B., Johnson, A., Lewis, J., Raff, K., Roberts, K. & Walters, P. *Molecular Biology of the Cell*. (Garland Science, 2002).
- 81 Butler, J. M. *Forensic DNA Typing*. (Elsevier, 2001).
- 82 Saenger, W. *Principles of Nucleic Acid Structure*. (Springer-Verlag, 1984).

- 83 Ghosh, A. & Bansal, M. A glossary of DNA structures from A to Z. *Acta Crystallographica Section D-Biological Crystallography* **59**, 620-626, (2003).
- 84 Berg, J., Tymoczko, J. & Stryer, L. *Biochemistry*. (W. H. Freeman and Company, 2002).
- 85 Bloomfield, V. A., Crothers, D. M. & Tinoco, I. *Nucleic Acids: Structure, Function and Properties.*, (University Science Books Sausalitos, 2000).
- 86 Chalikian, T. V., Volker, J., Plum, G. E. & Breslauer, K. J. A more unified picture for the thermodynamics of nucleic acid duplex melting: A characterization by calorimetric and volumetric techniques. *Proceedings of the National Academy of Sciences of the United States of America* **96**, 7853-7858, (1999).
- 87 Wing, R., Drew, H., Takano, T., Broka, C., Tanaka, S., Itakura, K. & Dickerson, R. E. Crystal-Structure Analysis of a Complete Turn of B-DNA. *Nature* **287**, 755-758, (1980).
- 88 Basu, H. S., Feuerstein, B. G., Zarling, D. A., Shafer, R. H. & Marton, L. J. Recognition of Z-Rna and Z-DNA Determinants by Polyamines in Solution - Experimental and Theoretical-Studies. *Journal of Biomolecular Structure & Dynamics* **6**, 299-309, (1988).
- 89 Yakovchuk, P., Protozanova, E. & Frank-Kamenetskii, M. D. Base-stacking and base-pairing contributions into thermal stability of the DNA double helix (vol 34, pg 564, 2006). *Nucleic Acids Research* **34**, 1082, (2006).
- 90 SantaLucia, J. A unified view of polymer, dumbbell, and oligonucleotide DNA nearest-neighbor thermodynamics. *Proceedings of the National Academy of Sciences of the United States of America* **95**, 1460-1465, (1998).
- 91 Merrifield, R. B. Solid Phase Peptide Synthesis .1. Synthesis of a Tetrapeptide. *Journal of the American Chemical Society* **85**, 2149, (1963).
- 92 Zadegan, R. M. & Norton, M. L. Structural DNA Nanotechnology: From Design to Applications. *International Journal of Molecular Sciences* **13**, 7149-7162, (2012).
- 93 Sarikaya, M., Tamerler, C., Jen, A. K. Y., Schulten, K. & Baneyx, F. Molecular biomimetics: nanotechnology through biology. *Nature Materials* **2**, 577-585, (2003).
- 94 Eichman, B. F., Vargason, J. M., Mooers, B. H. M. & Ho, P. S. The Holliday junction in an inverted repeat DNA sequence: Sequence effects on the structure of four-way junctions. *Proceedings of the National Academy of Sciences of the United States of America* **97**, 3971-3976, (2000).

References

- 95 Ban, E. & Picu, C. R. Strength of DNA Sticky End Links. *Biomacromolecules* **15**, 143-149, (2014).
- 96 Hays, F. A., Watson, J. & Ho, P. S. Caution! DNA crossing: crystal structures of Holliday junctions. *Journal of Biological Chemistry* **278**, 49663-49666, (2003).
- 97 Liberi, G. & Foiani, M. The double life of Holliday junctions. *Cell Research* **20**, 611-613, (2010).
- 98 LaBean, T. H., Yan, H., Kopatsch, J., Liu, F. R., Winfree, E., Reif, J. H. & Seeman, N. C. Construction, analysis, ligation, and self-assembly of DNA triple crossover complexes. *Journal of the American Chemical Society* **122**, 1848-1860, (2000).
- 99 Liu, D., Wang, M. S., Deng, Z. X., Walulu, R. & Mao, C. D. Tensegrity: Construction of rigid DNA triangles with flexible four-arm DNA junctions. *Journal of the American Chemical Society* **126**, 2324-2325, (2004).
- 100 Aldaye, F. A., Lo, P. K., Karam, P., McLaughlin, C. K., Cosa, G. & Sleiman, H. F. Modular construction of DNA nanotubes of tunable geometry and single- or double-stranded character. *Nature Nanotechnology* **4**, 349-352, (2009).
- 101 Mao, C. D., Sun, W. Q. & Seeman, N. C. Assembly of Borromean rings from DNA. *Nature* **386**, 137-138, (1997).
- 102 Shih, W. M., Quispe, J. D. & Joyce, G. F. A 1.7-kilobase single-stranded DNA that folds into a nanoscale octahedron. *Nature* **427**, 618-621, (2004).
- 103 Zhang, Y. W. & Seeman, N. C. Construction of a DNA-Truncated Octahedron. *Journal of the American Chemical Society* **116**, 1661-1669, (1994).
- 104 Seeman, N. C. DNA in a material world. *Nature* **421**, 427-431, (2003).
- 105 Andersen, E. S. *et al.* Self-assembly of a nanoscale DNA box with a controllable lid. *Nature* **459**, 73-75, (2009).
- 106 Douglas, S. M., Dietz, H., Liedl, T., Hogberg, B., Graf, F. & Shih, W. M. Self-assembly of DNA into nanoscale three-dimensional shapes. *Nature* **459**, 414-418, (2009).
- 107 Liedl, T., Hogberg, B., Tytell, J., Ingber, D. E. & Shih, W. M. Self-assembly of three-dimensional prestressed tensegrity structures from DNA. *Nature Nanotechnology* **5**, 520-524, (2010).
- 108 Sanderson, K. Bioengineering: What to make with DNA origami. *Nature* **464**, 158-159, (2010).

- 109 Han, D. R., Pal, S., Nangreave, J., Deng, Z. T., Liu, Y. & Yan, H. DNA Origami with Complex Curvatures in Three-Dimensional Space. *Science* **332**, 342-346, (2011).
- 110 Dietz, H., Douglas, S. M. & Shih, W. M. Folding DNA into Twisted and Curved Nanoscale Shapes. *Science* **325**, 725-730, (2009).
- 111 Liu, W. Y., Zhong, H., Wang, R. S. & Seeman, N. C. Crystalline Two-Dimensional DNA-Origami Arrays. *Angewandte Chemie-International Edition* **50**, 264-267, (2011).
- 112 Ohtsuki, M., Isaacson, M. S. & Crewe, A. V. Dark Field Imaging of Biological Macromolecules with the Scanning-Transmission Electron-Microscope. *Proceedings of the National Academy of Sciences of the United States of America* **76**, 1228-1232, (1979).
- 113 Beer, A. Determination of the absorption of red light in colored liquids. *Annalen der Physik und Chemie* **86**, 78-88, (1852).
- 114 Bendersky, L. A. & Gayle, F. W. Electron diffraction using transmission electron microscopy. *Journal of Research of the National Institute of Standards and Technology* **106**, 997-1012, (2001).
- 115 Smoluchowsky, M. Zur kinetischen Theorie der Brownschen Molekularbewegung und der Suspensionen. *Annalen der Physik* **326**, 756-780, (1906).
- 116 Einstein, A. Über die von der molekularkinetischen Theorie der Wärme geforderte Bewegung von in ruhenden Flüssigkeiten suspendierten Teilchen. *Annalen der Physik* **322**, 549-560, (1905).
- 117 Reddy, J. N. & Gartling, D. K. *The finite element method in heat transfer and fluid dynamics*. (CRC Press, 2010).
- 118 Yee, K. S. Numerical Solution of Initial Boundary Value Problems Involving Maxwells Equations in Isotropic Media. *Ieee Transactions on Antennas and Propagation* **14**, 302, (1966).
- 119 Douglas, S. M., Marblestone, A. H., Teerapittayanon, S., Vazquez, A., Church, G. M. & Shih, W. M. Rapid prototyping of 3D DNA-origami shapes with caDNAno. *Nucleic Acids Research* **37**, 5001-5006, (2009).
- 120 Castro, C. E., Kilchherr, F., Kim, D. N., Shiao, E. L., Wauer, T., Wortmann, P., Bathe, M. & Dietz, H. A primer to scaffolded DNA origami. *Nature Methods* **8**, 221-229, (2011).
- 121 Hughes, B. K., Luther, J. M. & Beard, M. C. The Subtle Chemistry of Colloidal, Quantum-Confined Semiconductor Nanostructures. *Acs Nano* **6**, 4573-4579, (2012).

- 122 Sau, T. K. & Rogach, A. L. Nonspherical Noble Metal Nanoparticles: Colloid-Chemical Synthesis and Morphology Control. *Advanced Materials* **22**, 1781-1804, (2010).
- 123 Choi, C. L. & Alivisatos, A. P. From Artificial Atoms to Nanocrystal Molecules: Preparation and Properties of More Complex Nanostructures. *Annual Review of Physical Chemistry, Vol 61* **61**, 369-389, (2010).
- 124 Sau, T. K., Rogach, A. L., Jackel, F., Klar, T. A. & Feldmann, J. Properties and Applications of Colloidal Nonspherical Noble Metal Nanoparticles. *Advanced Materials* **22**, 1805-1825, (2010).
- 125 Yu, Y. Y., Chang, S. S., Lee, C. L. & Wang, C. R. C. Gold nanorods: Electrochemical synthesis and optical properties. *Journal of Physical Chemistry B* **101**, 6661-6664, (1997).
- 126 Bakr, O. M., Wunsch, B. H. & Stellacci, F. High-yield synthesis of multi-branched urchin-like gold nanoparticles. *Chemistry of Materials* **18**, 3297-3301, (2006).
- 127 Hrelescu, C., Sau, T. K., Rogach, A. L., Jackel, F. & Feldmann, J. Single gold nanostars enhance Raman scattering. *Applied Physics Letters* **94**, (2009).
- 128 Eustis, S. & El-Sayed, M. A. Why gold nanoparticles are more precious than pretty gold: Noble metal surface plasmon resonance and its enhancement of the radiative and nonradiative properties of nanocrystals of different shapes. *Chemical Society Reviews* **35**, 209-217, (2006).
- 129 Mivelle, M., van Zanten, T. S., Neumann, L., van Hulst, N. F. & Garcia-Parajo, M. F. Ultrabright Bowtie Nanoaperture Antenna Probes Studied by Single Molecule Fluorescence. *Nano Letters* **12**, 5972-5978, (2012).
- 130 Landis, S., Constancias, C., Lnadis, S., Manakli, S., Martin, L., Pain, L. & Rio, D. *Electron beam lithography*. (John Wiley & Sons, Inc., 2013).
- 131 Gans, R. Über die form ultramikroskopischer goldteilchen. *Annalen der Physik* **342**, 881-900, (1912).
- 132 Tong, L. M., Miljkovic, V. D. & Kall, M. Alignment, Rotation, and Spinning of Single Plasmonic Nanoparticles and Nanowires Using Polarization Dependent Optical Forces. *Nano Letters* **10**, 268-273, (2010).
- 133 Urban, A. S. *Optothermal manipulation of phospholipid membranes with gold nanoparticles*, LMU München, (2010).
- 134 Do, J., Fedoruk, M., Jackel, F. & Feldmann, J. Two-Color Laser Printing of Individual Gold Nanorods. *Nano Letters* **13**, 4164-4168, (2013).

- 135 Ni, W. H., Ba, H. J., Lutich, A. A., Jackel, F. & Feldmann, J. Enhancing Single-Nanoparticle Surface-Chemistry by Plasmonic Overheating in an Optical Trap. *Nano Letters* **12**, 4647-4650, (2012).
- 136 Bastus, N. G., Comenge, J. & Puntès, V. Kinetically Controlled Seeded Growth Synthesis of Citrate-Stabilized Gold Nanoparticles of up to 200 nm: Size Focusing versus Ostwald Ripening. *Langmuir* **27**, 11098-11105, (2011).
- 137 Chen, H. J., Shao, L., Li, Q. & Wang, J. F. Gold nanorods and their plasmonic properties. *Chemical Society Reviews* **42**, 2679-2724, (2013).
- 138 Selhuber-Unkel, C., Zins, I., Schubert, O., Sonnichsen, C. & Oddershede, L. B. Quantitative optical trapping of single gold nanorods. *Nano Letters* **8**, 2998-3003, (2008).
- 139 Singer, W., Nieminen, T. A., Gibson, U. J., Heckenberg, N. R. & Rubinsztein-Dunlop, H. Orientation of optically trapped nonspherical birefringent particles. *Physical Review E* **73**, (2006).
- 140 Nedev, S., Urban, A. S., Lutich, A. A. & Feldmann, J. Optical Force Stamping Lithography. *Nano Letters* **11**, 5066-5070, (2011).
- 141 Shelton, W. A., Bonin, K. D. & Walker, T. G. Nonlinear motion of optically torqued nanorods. *Physical Review E* **71**, (2005).
- 142 Akahane, Y., Asano, T., Song, B. S. & Noda, S. High-Q photonic nanocavity in a two-dimensional photonic crystal. *Nature* **425**, 944-947, (2003).
- 143 Yoshie, T., Scherer, A., Hendrickson, J., Khitrova, G., Gibbs, H. M., Rupper, G., Ell, C., Shchekin, O. B. & Deppe, D. G. Vacuum Rabi splitting with a single quantum dot in a photonic crystal nanocavity. *Nature* **432**, 200-203, (2004).
- 144 Badolato, A., Hennessy, K., Atature, M., Dreiser, J., Hu, E., Petroff, P. M. & Imamoglu, A. Deterministic coupling of single quantum dots to single nanocavity modes. *Science* **308**, 1158-1161, (2005).
- 145 Hennessy, K., Badolato, A., Winger, M., Gerace, D., Atature, M., Gulde, S., Falt, S., Hu, E. L. & Imamoglu, A. Quantum nature of a strongly coupled single quantum dot-cavity system. *Nature* **445**, 896-899, (2007).
- 146 van der Sar, T., Hagemeyer, J., Pfaff, W., Heeres, E. C., Thon, S. M., Kim, H., Petroff, P. M., Oosterkamp, T. H., Bouwmeester, D. & Hanson, R. Deterministic nanoassembly of a coupled quantum emitter-photonic crystal cavity system. *Applied Physics Letters* **98**, (2011).
- 147 Wolters, J., Schell, A. W., Kewes, G., Nüsse, N., Schoengen, M., Doscher, H., Hannappel, T., Lochel, B., Barth, M. & Benson, O. Enhancement of the zero

- phonon line emission from a single nitrogen vacancy center in a nanodiamond via coupling to a photonic crystal cavity. *Applied Physics Letters* **97**, (2010).
- 148 Barth, M., Schietinger, S., Fischer, S., Becker, J., Nusse, N., Aichele, T., Lochel, B., Sonnichsen, C. & Benson, O. Nanoassembled Plasmonic-Photonic Hybrid Cavity for Tailored Light-Matter Coupling. *Nano Letters* **10**, 891-895, (2010).
- 149 De Angelis, F., Patrini, M., Das, G., Maksymov, I., Galli, M., Businaro, L., Andreani, L. C. & Di Fabrizio, E. A hybrid plasmonic-photonic nanodevice for label-free detection of a few molecules. *Nano Letters* **8**, 2321-2327, (2008).
- 150 Benson, O. Assembly of hybrid photonic architectures from nanophotonic constituents. *Nature* **480**, 193-199, (2011).
- 151 Adawi, A. M., Murshidy, M. M., Fry, P. W. & Lidzey, D. G. An Optical Nanocavity Incorporating a Fluorescent Organic Dye Having a High Quality Factor. *Acs Nano* **4**, 3039-3044, (2010).
- 152 Murshidy, M. M., Adawi, A. M., Fry, P. W., Whittaker, D. M. & Lidzey, D. G. The optical properties of hybrid organic-inorganic L3 nanocavities. *Journal of the Optical Society of America B-Optical Physics* **27**, 215-221, (2010).
- 153 Do, J., Sediq, K. N., Deasy, K., Coles, D. M., Rodriguez-Fernandez, J., Feldmann, J. & Lidzey, D. G. Photonic Crystal Nanocavities Containing Plasmonic Nanoparticles Assembled Using a Laser-Printing Technique. *Advanced Optical Materials* **1**, 946-951, (2013).
- 154 Oskooi, A. F., Roundy, D., Ibanescu, M., Bermel, P., Joannopoulos, J. D. & Johnson, S. G. MEEP: A flexible free-software package for electromagnetic simulations by the FDTD method. *Computer Physics Communications* **181**, 687-702, (2010).
- 155 Soukoulis, C. M. & Wegener, M. Past achievements and future challenges in the development of three-dimensional photonic metamaterials. *Nature Photonics* **5**, 523-530, (2011).
- 156 Liu, N., Hentschel, M., Weiss, T., Alivisatos, A. P. & Giessen, H. Three-Dimensional Plasmon Rulers. *Science* **332**, 1407-1410, (2011).
- 157 Zhao, Z., Jacovetty, E. L., Liu, Y. & Yan, H. Encapsulation of Gold Nanoparticles in a DNA Origami Cage. *Angewandte Chemie-International Edition* **50**, 2041-2044, (2011).
- 158 Kuzyk, A., Schreiber, R., Fan, Z. Y., Pardatscher, G., Roller, E. M., Hogele, A., Simmel, F. C., Govorov, A. O. & Liedl, T. DNA-based self-assembly of chiral plasmonic nanostructures with tailored optical response. *Nature* **483**, 311-314, (2012).

-
- 159 Jones, M. R., Macfarlane, R. J., Lee, B., Zhang, J. A., Young, K. L., Senesi, A. J. & Mirkin, C. A. DNA-nanoparticle superlattices formed from anisotropic building blocks. *Nature Materials* **9**, 913-917, (2010).
- 160 Zhou, J. F., Ralston, J., Sedev, R. & Beattie, D. A. Functionalized gold nanoparticles: Synthesis, structure and colloid stability. *Journal of Colloid and Interface Science* **331**, 251-262, (2009).
- 161 Mirkin, C. A., Letsinger, R. L., Mucic, R. C. & Storhoff, J. J. A DNA-based method for rationally assembling nanoparticles into macroscopic materials. *Nature* **382**, 607-609, (1996).
- 162 Alivisatos, A. P., Johnsson, K. P., Peng, X. G., Wilson, T. E., Loweth, C. J., Bruchez, M. P. & Schultz, P. G. Organization of 'nanocrystal molecules' using DNA. *Nature* **382**, 609-611, (1996).
- 163 Li, Z., Jin, R. C., Mirkin, C. A. & Letsinger, R. L. Multiple thiol-anchor capped DNA-gold nanoparticle conjugates. *Nucleic Acids Research* **30**, 1558-1562, (2002).
- 164 Zhang, X., Servos, M. R. & Liu, J. W. Fast pH-assisted functionalization of silver nanoparticles with monothiolated DNA. *Chemical Communications* **48**, 10114-10116, (2012).
- 165 Chi, Q. J., Wang, G. X. & Jiang, J. H. The persistence length and length per base of single-stranded DNA obtained from fluorescence correlation spectroscopy measurements using mean field theory. *Physica a-Statistical Mechanics and Its Applications* **392**, 1072-1079, (2013).
- 166 Schreiber, R., Do, J., Roller, E. M., Zhang, T., Schuller, V. J., Nickels, P. C., Feldmann, J. & Liedl, T. Hierarchical assembly of metal nanoparticles, quantum dots and organic dyes using DNA origami scaffolds. *Nature Nanotechnology* **9**, 74-78, (2014).
- 167 Vologodskii, A. & Frank-Kamenetskii, M. D. Strong bending of the DNA double helix. *Nucleic Acids Research* **41**, 6785-6792, (2013).
- 168 Mayilo, S., Kloster, M. A., Wunderlich, M., Lutich, A., Klar, T. A., Nichtl, A., Kurzinger, K., Stefani, F. D. & Feldmann, J. Long-Range Fluorescence Quenching by Gold Nanoparticles in a Sandwich Immunoassay for Cardiac Troponin T. *Nano Letters* **9**, 4558-4563, (2009).
- 169 Dulkeith, E., Morteani, A. C., Niedereichholz, T., Klar, T. A., Feldmann, J., Levi, S. A., van Veggel, F. C. J. M., Reinhoudt, D. N., Moller, M. & Gittins, D. I. Fluorescence quenching of dye molecules near gold nanoparticles: Radiative and nonradiative effects. *Physical Review Letters* **89**, (2002).

- 170 Persson, B. N. J. & Lang, N. D. Electron-Hole-Pair Quenching of Excited-States near a Metal. *Physical Review B* **26**, 5409-5415, (1982).
- 171 Anger, P., Bharadwaj, P. & Novotny, L. Enhancement and quenching of single-molecule fluorescence. *Physical Review Letters* **96**, (2006).
- 172 Stein, I. H., Steinhauer, C. & Tinnefeld, P. Single-Molecule Four-Color FRET Visualizes Energy-Transfer Paths on DNA Origami. *Journal of the American Chemical Society* **133**, 4193-4195, (2011).
- 173 Dutta, P. K., Varghese, R., Nangreave, J., Lin, S., Yan, H. & Liu, Y. DNA-Directed Artificial Light-Harvesting Antenna. *Journal of the American Chemical Society* **133**, 11985-11993, (2011).
- 174 Zheng, J. W., Chen, Z. C. & Liu, Z. F. Atomic force microscopy-based nanolithography on silicon using colloidal Au nanoparticles as a nanooxidation mask. *Langmuir* **16**, 9673-9676, (2000).
- 175 Moon, J. H., Jang, S. G., Lim, J. M. & Yang, S. M. Multiscale nanopatterns templated from two-dimensional assemblies of photoresist particles. *Advanced Materials* **17**, 2559, (2005).
- 176 Dhawan, A., Du, Y., Batchelor, D., Wang, H. N., Leonard, D., Misra, V., Ozturk, M., Gerhold, M. D. & Vo-Dinh, T. Hybrid Top-Down and Bottom-Up Fabrication Approach for Wafer-Scale Plasmonic Nanoplatfoms. *Small* **7**, 727-731, (2011).
- 177 Kraus, T., Malaquin, L., Schmid, H., Riess, W., Spencer, N. D. & Wolf, H. Nanoparticle printing with single-particle resolution. *Nature Nanotechnology* **2**, 570-576, (2007).
- 178 Hung, A. M., Micheel, C. M., Bozano, L. D., Osterbur, L. W., Wallraff, G. M. & Cha, J. N. Large-area spatially ordered arrays of gold nanoparticles directed by lithographically confined DNA origami. *Nature Nanotechnology* **5**, 121-126, (2010).
- 179 Do, J., Schreiber, R., Lutich, A. A., Liedl, T., Rodriguez-Fernandez, J. & Feldmann, J. Design and Optical Trapping of a Biocompatible Propeller-like Nanoscale Hybrid. *Nano Letters* **12**, 5008-5013, (2012).
- 180 Stehr, J., Hrelescu, C., Sperling, R. A., Raschke, G., Wunderlich, M., Nichtl, A., Heindl, D., Kurzinger, K., Parak, W. J., Klar, T. A. & Feldmann, J. Gold NanoStoves for microsecond DNA melting analysis. *Nano Letters* **8**, 619-623, (2008).
- 181 Huschka, R., Zuloaga, J., Knight, M. W., Brown, L. V., Nordlander, P. & Halas, N. J. Light-Induced Release of DNA from Gold Nanoparticles:

-
- Nanoshells and Nanorods. *Journal of the American Chemical Society* **133**, 12247-12255, (2011).
- 182 Karni, M., Zidon, D., Polak, P., Zalevsky, Z. & Shefi, O. Thermal Degradation of DNA. *DNA and Cell Biology* **32**, 298-301, (2013).
- 183 Dragan, A. I., Pavlovic, R., McGivney, J. B., Casas-Finet, J. R., Bishop, E. S., Strouse, R. J., Schenerman, M. A. & Geddes, C. D. SYBR Green I: Fluorescence Properties and Interaction with DNA. *Journal of Fluorescence* **22**, 1189-1199, (2012).
- 184 Helenius, V., Monshouwer, R. & vonGrondelle, R. Temperature-dependent lifetimes and quantum yield of the singlet and triplet states of the B820 subunit of LHI antenna complex of purple bacterium *Rhodospirillum rubrum*. *Journal of Physical Chemistry B* **101**, 10554-10559, (1997).
- 185 Ohlinger, A., Nedev, S., Lutich, A. A. & Feldmann, J. Optothermal Escape of Plasmonically Coupled Silver Nanoparticles from a Three-Dimensional Optical Trap. *Nano Letters* **11**, 1770-1774, (2011).

Acknowledgements

This work was carried out at Photonics and Optoelectronics group (PhOG) of Ludwig-Maximilian-Universität München for the last 3 years under the supervision of **Prof. Dr. Jochen Feldmann**. I would like to specially thank Prof. Dr. Jochen Feldmann for allowing me to be part of the PhOG members. High research standard and fantastic experimental equipment in the group helped me to concentrate on my study. Also, it was not possible to finish all projects successfully without his scientific guidance.

I thank **Prof. Dr. Tim Liedl** and **Prof. David G. Lidzey** for giving me a wonderful opportunity to have collaboration work with you.

I also want to thank:

Dr. Jessica Rodríguez Fernández, Dr. Frank Jäckel and **Dr. Andrey Lutich**, for their great scientific guidance and proof reading of this thesis.

Dr. Michael Fedoruk, Robert Schreiber and **Dr. Kieran Deasy**, who are involved in the projects, for wonderful teamwork and proof reading of this thesis.

Gerlinder Adam, Stefan Niedermaier, Christian Holopirek and **Katja Lyons**, for their bureaucratic and technical supports during my study.

Dr. Lindsey Anderson, Dr. Adam Blanch, Dr. Michael Carlson, for their hard work on decoding (Konglish → English) this thesis to make it readable.

Dr. Theobald Lohmüller, Dr. Jacek Stolarczyk, Dr. Habeeb Muhammed Madathumpady Abubaker, Dr. Carlos Cárdenas-Daw, Dr. Nicolas Bouchonville, Dr. Sol Carretero Palacios, Dr. Ming Fu, Dr. Karolina Milowska, Silke Kirchner, Spas Nedev, Paul Kühler, Miao Li, Verena Baumann, Anastasia Babynina, Verena Hintermayr, Thomas Simon, Florian Ehrat, Patrick Urban, and Carla Zensen, who are my former and current colleagues. All you guys are the best !!!

Last but not least, I thank **my family** in Korea. You made, you believed, and supported me. This thesis is my small present for you.

아버지, 어머니, 형님내외, 그리고 내 조카 윤이, 사랑합니다. 그리고 감사합니다.
이 논문은 당신들을 위한 조그만 선물입니다.